THESIS

RETRIEVAL OF AEROSOL SINGLE SCATTERING ALBEDO AT UV WAVELENGTHS FOR TWO URBAN FIELD CAMPAIGNS

Submitted by

Chelsea A. Corr

Department of Atmospheric Science

In partial fulfillment of the requirements

For the Degree of Master of Science

Colorado State University

Fort Collins, Colorado

Summer 2008

ABSTRACT OF THESIS

RETRIEVAL OF AEROSOL SINGLE SCATTERING ALBEDO AT UV WAVELENGTHS FOR TWO URBAN FIELD CAMPAIGNS

Aerosols significantly affect the intensity of surface ultraviolet (UV) irradiance with subsequent effects on the photolysis rates of tropospheric pollutants, however, aerosol optical properties (e.g., single scattering albedo) in the UV range remain largely unknown. The absence of appropriate instrumentation requires that aerosol UV optical properties be retrieved from the mathematical inversion of measured parameters, or, more specifically, UV surface irradiance. Such retrieval methods have been developed and used successfully in several studies.

Three commonly used retrieval methods were used in this work: the partial single-wavelength method, the full single-wavelength method, and the optimal estimation method. A single-wavelength method similar in design to those developed in previous studies was developed here for the retrieval of ranges of SSA values at two UV wavelengths (368nm and 332nm) for days during two field campaigns in Houston, TX in the Fall 2006 and Mexico City, Mexico in March 2006. Ranges of SSA values were retrieved by comparing modeled to measured direct-to-diffuse ratios (DDR). Several sensitivity studies were performed to examine the response of the DDR and the radiative transfer model (the Tropospheric Ultraviolet model 4.4) to ranges of input values.

Average SSA_{368} and SSA_{332} ranged from approximately 0.60 to 1.00 for both campaigns and were consistent with UV SSA values reported in other studies. Statistically lower range-averaged SSA_{332} with respect to range-averaged SSA_{368} occurred for a substantial fraction of all retrieval days for both field campaigns. Such a trend was attributed to the presence of larger particles and/or aerosol species with spectral absorption characteristics based on aerosol chemistry and meteorological data. Partial single-wavelength derived and full single-wavelength derived SSA compared favorably but both were higher than SSA values obtained using the optimal estimation method.

Chelsea A. Corr
Department of Atmospheric Science
Colorado State University
Fort Collins, CO 80523
Summer 2008

ACKNOWLEDGEMENTS

First and foremost, I would like to thank my advisor, Dr. Sonia Kreidenweis for her wise guidance, patience, and endless encouragement throughout this process. I also extend my utmost thanks to my co-advisor, Dr. James Slusser, for his though-provoking questions and enthusiastic support. A special thanks to my committee members, Dr. Jeffrey Collett, Jr. and Dr. Wei Gao, for solidifying this work through their input and suggestions.

I would also like to thank members of the Atmospheric Chemistry Research group at Colorado State University, in particular, those students and staff of the Kreidenweis group. Without their sense of humor and willingness to help, this work would not have been possible. Special thanks to Becky Olson, Dr. John Davis, George Jansen at the UV-B Monitoring and Research Program and Thomas Taylor at Colorado State University for their assistance with data collection and analysis. Finally, I'd like to recognize of my friends and family whose continued encouragement and praise has been greatly appreciated.

This work is supported by United States Department of Agriculture UV-B Monitoring and Research Program, under the Subaward number R-07-0173.

TABLE OF CONTENTS

LIST OF TABLES

LIST OF FIGURES

LIST OF NOTATIONS

$\{b_{ext}\}$	Volumetric extinction coefficient
$\{g\}$	Volumetric asymmetry parameter
$\{\omega\}$	Volumetric single scattering albedo
A	Surface albedo
AERONET	Aerosol Robotic Network
AOD	Aerosol optical depth
α	Angstrom exponent
β	Fixed model inputs
$b_{abs, p}$	Aerosol absorption coefficient
$b_{ext, p}$	Aerosol extinction coefficient
$b_{scat, p}$	Aerosol scattering coefficient
BC	Black carbon
χ^2	Chi-squared statistic
$Cl^{\cdot}$	Chlorine radical
C_{abs}	Absorption cross-section
C_{ext}	Extinction cross-section
C_{scat}	Scattering cross-section
CNRS	Centre National de la Recherche Scientifique

CST	Central Standard Time
δ	Relative error
D_p	Particle diameter
D_T	Diffuse fraction
ds	Path length
DDR	Direct-to-diffuse Ratio
DH	Diffuse horizontal irradiance
DN	Direct normal irradiance
DISORT	Discrete Ordinate Method
DOY	Day of year
ε	Error in optimal estimation
EC	Elemental Carbon
ϕ	Azimuth angle
Φ	Scalar cost function
F	Forward model
FWHM	Full Width at Half Maximum
g	Asymmetry parameter
GSFC	Goddard Space Flight Center
$HO_2^{\cdot}$, $RO_2^{\cdot}$	Peroxy radicals
H_2O_2	Hydrogen peroxide
HCHO	Formaldehyde
HONO	Nitrous acid

HYSPLIT	Hybrid Single-Particle Lagrangian Integrated Trajectory
I	Irradiance
I_o	Extraterrestrial irradiance
j	Photolysis rate coefficient
J	Emission due to multiple scattering
κ	Sample size
κ_{eff}	Effective sample size
K	Jacobian weighting matrix
k	Imaginary part of the refractive index
λ	Wavelength
μ	Complex refractive index
m	Air mass factor
MILAGRO	Megacity Initiative: Local and Global Research Objectives
ν	Degrees of freedom
n	Real part of the refractive index
N	Particle number concentration
$n(D_p)$	Number size distribution
NASA	National Aeronautics and Space Administration
NO_2	Nitrogen dioxide
NO_x	Oxides of nitrogen
NOAA	National Oceanic and Atmospheric Administration

NMT	North Moody Tower
NUV	Near ultraviolet range
O_2	Oxygen
O_3	Ozone
$OH^{\cdot}$	Hydroxyl radical
OC	Organic Carbon
OE	Optimal Estimation
P	Particle phase function
PM_{10}	Coarse mode particles
PDF	Probability Distribution Function
θ	Solar zenith angle
Θ	Scattering angle
Q_{180}	180^{o} backscattering efficiency
Q_{abs}	Absorption efficiency
Q_{back}	Backscattering efficiency
Q_{ext}	Extinction efficiency
Q_{neph}	Nephelometer scattering efficiency
$Q_{nephback}$	Nephelometer backscattering efficiency
Q_{scat}	Scattering efficiency
ρ	Particle radius
R	Earth-Sun distance
r	Correlation coefficient
r_1	Lag-1 autocorrelation

s	Standard deviation
S_a	Covariance of *a priori* values
S_y	Covariance of measurements
SSA	Single scattering albedo
SMPS	Scanning Mobility Particle Sizer
SZA	Solar zenith angle
t	Student's t-test t score
t_{crit}	Critical t-value
T	Transmission
T1	MILAGRO measurement site
τ_T	Total optical depth
τ_r	Rayleigh optical depth
τ_g	Trace gas optical depth
TexAQS II/GoMACCS	Texas Air Quality Study II/Gulf of Mexico Atmospheric Composition and Climate Study
TOC	Total Ozone Column
TUV	Tropospheric Ultraviolet Model
USDA	United States Department of Agriculture
UV	Ultraviolet
UV-A	Ultraviolet radiation with 315nm<wavelength<400nm
UV-B	Ultraviolet radiation with 280nm<wavelength<315nm
UV-C	Ultraviolet radiation with 200nm<wavelength<280nm
UV-MFRSR	Ultraviolet Multi-filter Shadowband Radiometer

UVMRP	UV-B Monitoring and Research Program
V	Measured voltage
V_o	Extraterrestrial voltage
V_T	Measured transmission
Vis-MFRSR	Visible Multi-filter Shadowband Radiometer
VOC	Volatile Organic Carbon
$\hat{x}$	State vector
$\bar{x}$	Sample mean
x_a	*A priori* vector
x_n	Aerosol size distribution of moment *n*
Ψ	Intensity of scattered radiation
y	Set of measured parameters
YES	Yankee Environmental Systems
z	Height

1 Introduction

Because of their significant effects on health, cloud formation and precipitation, air quality, and climate, many modeling, laboratory and field studies have focused on characterizing the chemical and physical properties of atmospheric aerosols. Additionally, many studies have examined aerosol interactions with atmospheric gases and radiation on the local, regional, and global scales. Most relevant to the recently widely debated topic of climate change is the effect of aerosols on Earth's energy budget. It has been projected that aerosols have a direct effect on the energy budget comparable to that of greenhouse gases but opposite in sign [*Forster et al.*, 2007] through their interactions with solar radiation. Aerosols are observed to both scatter and absorb atmospheric radiation, with the chemical and physical properties of the aerosol governing whether the aerosol preferentially absorbs or scatters. These absorption and scattering properties of aerosols at visible wavelengths (λ, 400nm to 700nm) are responsible for visibility degradation and regional haze [*Haywood et al.*, 2003; *Kerr et al.*, 2004; *McMeeking et al.*, 2006]. Aerosols also interact with solar radiation through their role in cloud formation. Known as the aerosol indirect effect, the chemical and physical properties (e.g., particle size) of aerosols affect their ability to act as cloud condensation nuclei,

resulting in changes to cloud reflectivity and lifetime [*Rosenfeld*, 2000; *Twomey*, 1977].

Aerosol interactions with radiation in the visible and infrared (λ>700nm) wavelength ranges have been the focus of most aerosol radiative effects studies as these wavelengths are most relevant to climate change. Less understood, but potentially equally important, are aerosol interactions with ultraviolet radiation (λ<400nm). The perturbation of UV energy flux to Earth's surface by aerosols may result in important changes to photochemistry and biologically-active UV radiation, with consequential impacts on the biosphere. Appropriately characterizing the absorption and scattering properties of aerosols in the ultraviolet range allows for a more precise quantification of the amount of ultraviolet radiation reaching the surface, a value necessary for accurately forecasting air quality (i.e., the strength and frequency of photochemical smog episodes) and daily UV exposure risks.

1.1 Ultraviolet Radiation and Photochemistry in the Atmosphere

The sun behaves as a nearly perfect blackbody, with an emission spectrum outside of Earth's atmosphere approximating blackbody emission at 5770 K [*Finlayson-Pitts and Pitts*, 2000]. However, as solar radiation travels through the atmosphere, the spectral distribution is modified due to the preferential absorption and scattering over certain wavelength ranges by atmospheric gases and aerosols. This attenuation yields a radiation spectrum ranging from approximately 290nm to 2400nm at Earth's surface, a range optimized to drive Earth's biological and physical processes [*Finlayson-Pitts and Pitts*, 2000].

The shortest wavelengths that penetrate the mesosphere are in the near ultraviolet (NUV) region and range from 200nm to 400nm [*Finlayson-Pitts and Pitts*, 2000]. The NUV region is further broken down into the UV-A (315nm to 400nm), UV-B (280nm to 315nm), and UV-C (200nm to 280nm) regions. UV-C radiation is effectively removed in the stratosphere by the photodissociation of molecular oxygen (O_2) (optimized at $\lambda<242$nm) and stratospheric ozone (O_3) (optimized at $245\text{nm}<\lambda<310\text{nm}$) in the ozone layer [*Finlayson-Pitts and Pitts*, 2000]. Absorption by stratospheric O_3 extends into the short-wavelength UV-B ($\lambda<336$nm), however absorption at these wavelengths is weaker than absorption in the UV-C thereby allowing some transmission of radiation at these wavelengths [*Finlayson-Pitts and Pitts*, 2000].

The UV-A and UV-B radiation not absorbed in the stratosphere reaches Earth's surface and has been measured in several studies [e.g., *Herman et al.*, 1999; *Wetzel et al.*, 2003]. Though UV radiation only comprises a small fraction of the total radiation reaching Earth's surface, the impact this UV radiation has on tropospheric chemistry as well as human and ecosystem health is tremendous. Prolonged exposure to UV-A and UV-B radiation has been shown to result in negative health effects such as skin cancer, DNA damage, cataracts, and suppression of the immune systems in humans [*Diffey*, 1991; *Longstreth et al.*, 1998]. Similarly, DNA damage in terrestrial plants has been found with exposure to UV-B and UV-A radiation, ultimately resulting in changes in plant growth and cell function [*Bornman and Teramura*, 1993].

In the troposphere, UV-A and UV-B radiation drives much of the photochemistry and oxidation thus playing a major role in the overall chemistry of the troposphere. For instance, the formation of the most prevalent oxidant in the atmosphere, the hydroxyl radical ($OH^{\cdot}$), mostly occurs via three photolysis reactions: the photolysis of O_3, the photolysis of nitrous acid (HONO), and the photolysis of hydrogen peroxide (H_2O_2), all of which are most effective in the wavelength range of 300nm to 400nm [*Finlayson-Pitts and Pitts*, 2000]. Additionally, species such as aldehydes and chloride-containing compounds are readily photolyzed over this wavelength range to form highly reactive peroxy radicals ($HO_2^{\cdot}$, $RO_2^{\cdot}$) and chlorine radicals ($Cl^{\cdot}$) that also participate in tropospheric oxidation processes.

UV-A and UV-B radiation in the troposphere is also responsible for the formation of ground-level O_3 through reaction mechanisms involving volatile organic carbon species (VOCs) and oxides of nitrogen (NO_x). Under stagnant air conditions, VOCs build up in the atmosphere and photolyze to create $HO_2^{\cdot}$ and $RO_2^{\cdot}$, the radical species primarily responsible for the oxidation of nitric oxide (NO) (emitted from anthropogenic sources) to nitrogen dioxide (NO_2). NO_2 is efficiently photolyzed by UV-A radiation to form ground-state oxygen ($O(^3P)$) which, after reaction with O_2, forms ground-level O_3. Because of the lung tissue damage encountered with the inhalation of O_3 [*Zwick et al.*, 1991], controls on the formation of ground-level O_3 have been the subject of numerous studies, including ones focused on the effects of the changes in the amount of available UV energy on photolysis rates [*Dickerson et al.*, 1997; *Liao et al.*, 1999].

1.2 Aerosol Interactions with Ultraviolet Radiation

A general scheme for atmospheric attenuation pathways for broadband incoming solar radiation is described in Figure 1.1. These pathways are applicable to UV radiation and explain the loss of UV radiation as it travels through the atmosphere. UV absorption by gases (indicated by pathway 1) primarily occurs in the stratosphere with some gas-phase photochemistry in the troposphere, as discussed in the previous section. Pathway 2, or the absorption or reflection of radiation by the surface (characterized as the surface albedo), has been examined by several studies for the UV range, with estimates ranging from 0.01 to 1.0 depending on surface type [*Castro et al.*, 2001; *Madronich*, 1993; *McKenzie et al.*, 1996; *Scourfield and Bodeker*, 2000; *Webb et al.*, 2000]. The scattering by clouds and the scattering and absorption by aerosols have also been the subject of many studies, with a number of those studies reporting significant effects on the UV radiation budget [e.g., *Diaz et al.*, 2000; *Junkermann*, 2005; e.g., *Reuder and Schwander*, 1999].

1.2.1 Aerosol Effects on Ultraviolet Irradiance

The scattering and absorption properties of aerosols have been extensively studied in the visible range to estimate the contributions of aerosols to Earth's energy budget [e.g., *Ghan et al.*, 2001]. Motivated by recent concerns of increases in surface UV radiation with a thinning stratospheric ozone layer [*Blumthaler and Ambach*, 1990; *McKenzie et al.*, 1999], attention has been given to extending these aerosol optical properties to shorter wavelengths and to estimating the effects of aerosols on UV radiation. Recent studies show aerosols can cause changes to the surface UV

radiation field on the order of those caused by the thinning ozone layer but opposite in sign [*Elminir*, 2007; *Reuder and Schwander*, 1999].

Generally speaking, it has been determined using modeling techniques that those aerosols that primarily scatter visible light also scatter UV radiation and those aerosols that absorb visible light also absorb UV radiation [*Dickerson et al.*, 1997; *He and Carmichael*, 1999; *Liao et al.*, 1999; *Reuder and Schwander*, 1999]. Aerosol scattering is responsible for the conversion of direct radiation to diffuse radiation, resulting in either increases or decreases to the photon path length, depending on the solar zenith angle (SZA). Aerosol absorption removes UV radiation from the system resulting in a significant decrease in surface UV amounts [*He and Carmichael*, 1999; *Liao et al.*, 1999]. Typically, as SZA increases, the attenuation by both absorbing and scattering aerosols is enhanced, with greatest effects at shorter UV-B wavelengths [*Reuder and Schwander*, 1999]. This is especially true for aerosol scattering properties; at small SZAs (mid-afternoon hours) scattering aerosols increase photon path length resulting in a slight increase in surface UV radiation, while at high SZAs (i.e., morning or late afternoon/evening hours), the path length of incoming radiation is much longer relative to the diffuse radiation (i.e., scattered radiation) and thus the addition of scattering aerosol yields a reduction in surface UV radiation [*Dickerson et al.*, 1997; *Liao et al.*, 1999; *Reuder and Schwander*, 1999]. There is also a noted effect of aerosol column load on these aerosol optical properties, with a general increase in the aerosol effect on UV radiation with increase in column load [*He and Carmichael*, 1999].

The combined effects of aerosol UV scattering and absorption have been shown to cause a local reduction in UV radiation on the order of 15-25% at small SZAs and as much as 30-45% at larger SZAs, with some spectral dependence of attenuation at each SZA (i.e., aerosols attenuate more short-wavelength UV than long-wavelength UV) [*Reuder and Schwander*, 1999]. Papayannis et al. [1998] reported similar observations of a reduction in surface UV radiation by 30-40% that they attributed to the presence of urban aerosols. Urban aerosols are also suggested to be responsible for 40% less UV-B radiation measured at a metropolitan site in Mexico City compared to UV-B radiation measured in a suburban area of Mexico City during pollution events [*Acosta and Evans*, 2000]. High concentrations of coarse mode particles (PM_{10}) are shown to be well-correlated with a decrease in UV-B radiation of nearly 40% [*Elminir*, 2007]. These larger particles include mineral dust, a strong UV absorber that alone has been estimated to reduce global UV irradiance by 2-4% [*Diaz et al.*, 2000].

Indirect radiative effects of aerosols via cloud-radiation interactions have also been observed in the UV [*Junkermann et al.*, 2002; *Junkermann*, 2005; *Lefer et al.*, 2003]. Flight experimental data reveal an enhancement of UV-A flux in between cumulus clouds, with a slight decrease in UV-B flux near cloud edge, as well as reductions in UV-A and UV-B actinic flux by 45% and 25% below cloud, respectively [*Junkermann*, 2005]. Ground-based irradiance measurements have indicated that low-level clouds (e.g., stratus) can cause a reduction in surface UV-B radiation between 30-55% while high-level clouds (e.g., cirrus) attenuate 20-83% of

the UV-B radiation reaching the troposphere depending on the percentage of cloud cover [*Adam and El Shazly*, 2007].

1.2.2 Aerosol Effects on Photochemistry

Changes in the intensity of UV radiation reaching the surface due to interactions with aerosols have been show to significantly affect tropospheric photochemistry, with studies indicating both increases and decreases in photolysis rates, depending on the type and amount of aerosol present as well as SZA [*Castro et al.*, 2001; *He and Carmichael*, 1999; *Lefer et al.*, 2003; *Liao et al.*, 1999; *Reuder and Schwander*, 1999]. Regardless of their specific optical properties, aerosols are estimated to causes changes in photolysis rates on the order of 20% [*Lefer et al.*, 2003]. These changes result in increases or decreases in tropospheric ozone, with increased photolysis rates increasing ozone concentrations and vice versa [*Castro et al.*, 2001; *Dickerson et al.*, 1997; *He and Carmichael*, 1999].

The effects of a well-mixed layer of pure sulfate ($(NH_4)_2SO_4$) aerosol (a nearly perfect scatterer) extending from the surface to 5km on photolysis rate coefficients for ozone (j_{O3}), nitrogen oxide (j_{NO2}), and formaldehyde (j_{HCHO}) were examined in a modeling study conducted by Liao et al. [1999]. The study determined that, under cloud-free skies and an SZA of 0^o, photolysis rate coefficients in presence of aerosol for all three species were larger than reference photolysis rates calculated for cloud and aerosol free conditions throughout the atmosphere, with more pronounced increases above 1km (Figure 1.2). At a larger SZA, the effects of $(NH_4)_2SO_4$ show a similar trend above 1km, however a noted decrease in photolysis

rates with decrease in height occurs below 1km [*Liao et al.*, 1999]. Overall values of j_{O3}, j_{NO2}, and j_{HCHO} are also smaller at larger SZAs [*Liao et al.*, 1999]. Similar findings were posted by He and Carmichael [1999] indicated a moderate loading of scattering maritime and rural (remote) aerosol results in increases of surface j_{NO2} by 3.44% and 1.38%, respectively. Above the boundary layer, increases in photolysis rates as a result of aerosol scattering can be more substantial with j-values increasing by as much as 32% [*He and Carmichael*, 1999].

Strongly absorbing aerosols, such as soot, have been shown to decrease tropospheric averaged photolysis rates by as much as 10-18%, in concentrations representative of an urban plume [*Liao et al.*, 1999]. A decrease in j-values from reference photolysis rates is seen at all altitudes with most pronounced decreases occurring at the surface and under higher aerosol concentrations (Figure 1.3) [*Liao et al.*, 1999]. At the surface, the decrease in photolysis rates is estimated to be 20%, resulting in a large decrease in tropospheric ozone concentrations (~70%) [*He and Carmichael*, 1999]. Dickerson et al [1997] and later Liao et al [1999] found j-values decrease at all SZAs and j-values were smaller overall at higher SZAs when absorbing aerosols are present. External and internal mixtures of absorbing and scattering aerosols result in decreases of photolysis rates comparable to those seen for pure soot aerosol under cloud-free conditions [*Liao et al.*, 1999].

Clouds also affect photolysis rates, as suggested by the previously discussed effects of clouds on UV radiation. In Junkermann et al. [2002], model simulations were run with a mean cloud cover of 20% to examine the effects of a broken cloud field on photolysis frequencies. While it was shown that some enhancement of j_{NO2}

and j_{O3} occurred at cloud edges, there was an overall decrease in photolysis frequency in the presence of clouds. Using data obtained during aircraft measurements, Lefer et al [2003] suggested j_{NO2} values could be increased by 200% above a solid sheet of cloud cover while below the cloud deck NO_2 photolysis rates could decrease by up to 90%. Clouds may also affect aerosol effects on UV radiation. In the presence of stratus clouds (approximately 100% cloud cover) aerosol effects are less pronounced and even negligible compared to cloud radiative properties below cloud level [*Liao et al.*, 1999].

1.2.3 Determination and Estimates of UV Aerosol Optical Properties

Aerosol interactions with solar radiation are defined by several optical properties. Such properties are used to describe particles' ability to remove energy from the atmospheric system and the preferred mechanism (i.e., scattering or absorption) and are needed to accurately model the effects of aerosols on surface UV intensity.

Aerosol Optical Depth and the Angstrom Exponent

Optical depth is the attenuation of radiation integrated through a layer of atmosphere due to the presence of aerosols and gases and is the sum of attenuation due to both scattering and absorption by these atmospheric constituents. Aerosol optical depth, or AOD, is determined by the subtraction from the total optical depth (τ_T) of the optical depth due to background gases, (termed Rayleigh optical depth, τ_r) as well as the optical depth of relevant trace gases (e.g., water vapor, O_3) (τ_g) that may absorb at the wavelength of interest,

$$AOD = \tau_T - \tau_r - \tau_g \quad (1.1)$$

It is may also be expressed as the integration of the aerosol extinction coefficient ($b_{ext,p}$) over a layer height

$$AOD = \int_{z_1}^{z_2} b_{ext,p}\, dz \quad (1.2)$$

where $b_{ext,p}$ is the aerosol extinction coefficient (specific to the aerosol size distribution, number concentration, and refractive index), and z_1 and z_2 are the lower and upper bounds of the heights of the atmospheric layer of interest. Monochromatic total optical depth is related to solar irradiance by the Beer-Lambert law

$$\frac{I_\lambda}{I_{\lambda,o}} = R^2 \exp\left(-m\,\tau_{T,\lambda}\right) \quad (1.3)$$

where I is the observed irradiance at a single wavelength , I_o is the extraterrestrial irradiance at that same wavelength, $\tau_{T,\lambda}$ is total optical depth at the wavelength of interest, m is the air mass factor, and R is the Earth-Sun distance. Many ground-based instruments measuring irradiance employ this concept in what is termed the Langley method [*Slusser et al.*, 2000] using a synonymous equation,

$$\frac{V_\lambda}{V_{\lambda,o}} = R^2 \exp\left(-m\,\tau_\lambda\right) \quad (1.4)$$

where V is the instrument measured voltage (the raw measurement of irradiance outputted by many instruments) at a single wavelength and V_o is the extraterrestrial voltage at that wavelength, thus producing values for total optical depth at a given wavelength and m.

Values of AOD typically are between 0 and 1, with larger values generally indicating the presence of more aerosol. Several studies focusing on the retrieval of

aerosol UV optical properties have determined AOD using the aforementioned Langley method (Table 1.1). For example, Wetzel et al [2003] determined AOD at 368nm for three air mass types characteristic of the remote Alaskan atmosphere. For arctic haze air masses (dominated by sulfates and trace metal species) AOD was less than 0.1, while Asian dust and marine aerosol dominated air masses had AODs of 0.12-0.25 [*Wetzel et al.*, 2003]. AOD generally increases with a decrease in wavelength, thus, at a given time, UV AOD will be larger than AOD at visible wavelengths. Jacovides et al [2005] found during a study in Athens, Greece that AODs in the UV-A (350nm) were as much as a factor of two higher than AOD at 500nm for many of the study days. Similar findings were also reported for urban aerosols measured near the Goddard Space Flight Center (AODs of 1.48 and 1.02 for 340nm and 500nm, respectively) [*Eck et al.*, 1998; *Krotkov et al.*, 2005a]. Additionally, Eck et al [1998] determined this relationship to exist for biomass burning aerosols (e.g., during a Bolivian burning event, AOD at 340nm was measured as 3.02 while AOD at 500nm was 2.09) as well as desert dust aerosols (AOD at 340nm of 0.62 versus AOD at 500nm of 0.41).

The relationship between wavelength and optical depth is described by the Angstrom exponent, α, such that

$$\frac{AOD}{AOD_o} = \left(\frac{\lambda}{\lambda_0}\right)^{-\alpha} \qquad 1.5$$

where λ, is wavelength and λ_o is a reference wavelength. The Angstrom exponent is calculated as the slope of a simple linear fit through a plot of natural log of

wavelength (lnλ) versus natural log of AOD as is described by the rearrangement of the Angstrom equation

$$\alpha = -\frac{\ln \frac{AOD_2}{AOD_1}}{\ln \frac{\lambda_2}{\lambda_1}} \qquad 1.6$$

where 1 and 2 denote the use of two different wavelengths and their corresponding optical depths. However it should be noted that the lnλ-ln(AOD) relationship is not necessarily linear. King and Byrne [1976] and later Kaufman [1993] determined that the modal nature of aerosol size distributions causes a curvature in the Angstrom exponent relationship between the natural log of AOD and the natural log of wavelength. Furthermore, Eck et al [1998] suggests that the degree of curvature of this relationship is controlled by the concentration of particles in the accumulation mode (D_p<1.0μm). This curvature is lost when the Angstrom exponent is calculated for wavelength pairs, however the dependence of the Angstrom exponent on aerosol size distribution is not. Studies have indicated that values for the Angstrom exponent calculated for short wavelength pairs (e.g., 340-440nm) are different from those calculated for longer wavelength pairs (e.g., 500-670nm) due to sensitivities of the Angstrom exponent to the concentration and mean diameter of the accumulation mode aerosol [*Eck et al.*, 1998; *Jacovides et al.*, 2005; *Reid et al.*, 1999; *Schuster et al.*, 2006].

For aerosols, the Angstrom exponent typically ranges between 0 and 4, with a dependence on particle size. The Angstrom exponent increases and approaches 4 (the

Rayleigh limit) with decrease in mean particle diameter while values near zero are obtained for size distributions with a mean diameter larger than 0.2 μm.

Single Scattering Albedo

The single scattering albedo (SSA) is a measure of particle scattering relative to total extinction by particles (absorption plus scattering). Mathematically, SSA is described by the expression

$$SSA = \frac{b_{sca,p}}{b_{ext,p}} \tag{1.7}$$

where $b_{sca,p}$ is the aerosol scattering coefficient and $b_{ext,p}$ is expressed by the sum of the aerosol scattering and absorption ($b_{abs,p}$) coefficients

$$b_{ext,p} = b_{sca,p} + b_{abs,p} \tag{1.8}$$

Atmospherically-relevant SSA values fall between 0.5 and 1, with SSA values of 1 indicating a particle is purely scattering and values less than one indicating some particle absorption [*Seinfeld and Pandis*, 2006]. Madronich [1993] reports SSA values in the UV-range typically range from 0.80 to 0.99. Results from several recent studies have calculated SSA values consistent with this range for a variety of aerosol loadings and air mass types (Table 1.1) [*Krotkov et al.*, 2005b; *Petters et al.*, 2003; *Wenny et al.*, 1998; *Wetzel et al.*, 2003].

A SSA wavelength dependence has been suggested as a function of particle composition and size. Bergstrom et al. [2002] suggested SSA follows a power-law relationship with wavelength such that particle size governs whether the SSA increases, decreases, or remains the same over a wavelength range. Assuming extinction follows a power law, SSA can be written as a function of wavelength

$$SSA = 1 - \left(\frac{b_{abs,0}}{b_{ext,0}} \right) \left(\frac{\lambda}{\lambda_o} \right)^{-1+\alpha} \quad 1.9$$

where α is the angstrom exponent [*Bergstrom et al.*, 2002]. If the aerosol is dominated by smaller particles (i.e., freshly emitted aerosol), such as EC, α would be greater than 1 and thus, SSA should decrease with an increase in wavelength. Oppositely, in the presence of larger particles ($\alpha < 1$), SSA would increase with increase in wavelength.

This behavior is largely related to the relationships between the absorption and the scattering Angstrom exponents with particle diameter. The absorption and scattering Angstrom exponents describes the relationship between the particle absorption and wavelength and particle scattering with wavelength, respectively. Generally speaking, the absorption by particles increase with decrease in wavelength by a power-law relationship, regardless of particle size as particle absorption is largely driven by particle composition and not diameter, thus yielding absorption Angstrom values of 1 or greater. Particle scattering, on the other hand, is strongly related to particle size, such that the scattering Angstrom is small (and thus scattering is strong at all wavelengths) for large particles while the scattering Angstrom is large for smaller particles. Thus for larger particles (e.g., seasalt, mineral dust), where change in scattering with wavelength is negligible, SSA decreases with a decrease in wavelength as the absorption increases with wavelength [*Bergstrom et al.*, 2007]. For smaller particles, such as those associated with fresh urban emissions, scattering and absorption have competing effects. However, the scattering Angstrom is generally

larger than the absorption Angstrom thus yielding an apparent increase in SSA with decrease in wavelength [*Bergstrom et al.*, 2007].

While theory suggests the absorption Angstrom exponent will not exceed 1.5, several studies have observed larger absorption Angstrom exponents indicating a stronger wavelength dependence of absorption for certain aerosol species [*Bergstrom et al.*, 2007; *Bond*, 2001; *Kirchstetter et al.*, 2004]. Several studies have observed stronger absorption of UV radiation than visible radiation by mineral dust, resulting in lower SSA values at UV wavelengths than visible wavelengths [*Bergstrom et al.*, 2004; *Sokolik and Toon*, 1999; *Weaver et al.*, 2002; *Wetzel et al.*, 2003]. This dependence is largely explained by the mineral components of the dust particles, with the volume fraction of iron-containing minerals governing the degree of SSA spectral dependence [*Derimian et al.*, 2007; *Sokolik and Toon*, 1999]. Similarly, Jacobson [1999] suggested that nitrated and aromatic aerosol components preferentially absorb UV radiation thus resulting in lower SSA values at shorter wavelengths. In contrast, the SSA of black carbon containing aerosols has been shown to decrease with increase in wavelength, implying stronger absorption of visible and infrared radiation [*Bergstrom et al.*, 2002; *Eck et al.*, 1998]. Bergstrom et al. [2003] showed this dependence through the calculation of spectral SSA of an aerosol layer consisting primarily of biomass burning aerosol from irradiance data. An increase in the absorption Angstrom exponent (and thus an increase in the strength of the wavelength-dependence of particle absorption) may impact the how the SSA behaves as a function of wavelength by affecting the relationship between scattering Angstrom and absorption Angstrom.

Asymmetry Parameter

Assuming particle sphericity, a beam of radiation can be scattered in 360^o, with particle shape and composition governing the intensity and direction of scattering. The asymmetry parameter, *g* is the intensity-weighted average of the cosine of the scattering angle, used to describe the direction in which most of the radiation is scattered [*Seinfeld and Pandis*, 2006]. Mathematically, *g* is written

$$g = \frac{1}{2}\frac{\int_0^{\pi} \cos\Theta\Psi(\Theta)\sin\Theta d\Theta}{\int_0^{\pi} \Psi(\Theta)\sin\Theta d\Theta} \qquad 1.10$$

where Θ is the scattering angle and $\Psi(\Theta)$ is intensity. Values for *g* range from -1 to 1, with a value of -1 indicating most of the radiation is backscattered, a value of 1 indicating much of the radiation is forward scattered, and 0 indicating the radiation is scattered isotropically.

For spherical particles, g can be determined from theory. Larger particles ($D_p \geq 1\mu m$) are more efficient forward scatterers than smaller particles, which exhibit some backscattering in addition to forward scattering. Thus *g* has a pronounced dependence on particle size, with larger values indicating the presence of larger particles and smaller values indicating smaller particles. For atmospheric aerosols, values of *g* typically range from 0.6 to 0.8, with virtually no dependence on wavelength [*Madronich*, 1993]. Values in this range have been observed in several studies in the UV and are reported in Table 1.1.

1.3 Problem Statement

Several studies have modeled significant changes in the surface UV radiation field due to the presence of aerosols [e.g., *Diaz et al.*, 2000; *Junkermann*, 2005; e.g., *Reuder and Schwander*, 1999]. However, the aerosol UV optical properties needed to properly model UV surface irradiance are not widely known. Few studies have quantified asymmetry parameter and single scattering albedo [*Bergstrom et al.*, 2003; *Goering et al.*, 2005; *Krotkov et al.*, 2005b; *Petters et al.*, 2003; *Taylor et al.*, 2008; *Wenny et al.*, 1998; *Wetzel et al.*, 2003] in the UV range. Similarly, while studies suggest spectral absorption characteristics that extend into the UV [e.g., *Jacobson*, 1999], there has been little work done to compare aerosol optical properties (e.g., SSA) for the visible range to those calculated in the UV.

While UV aerosol optical properties are essential to accurately model surface UV irradiance, determining UV aerosol optical properties is not trivial. Unlike optical properties in the visible range, measurement of UV aerosol optical properties is difficult due to the lack of appropriate instrument availability. As a result, UV aerosol optical properties must be determined mathematically through the inversion of measured parameters. In such inversion methods, these measured parameters are compared to a set of the same parameters modeled for variable conditions. Inversion results are those conditions that yield a value for the model parameters that best match the measured parameters. Following this theory, "best-fit" UV aerosol optical properties are determined at the convergence of measured and modeled parameters such as irradiance. UV optical property retrieval methods are less-than-ideal as they require additional data sets or assumptions of aerosol physical properties (e.g.,

number size distribution), concentrations of UV-absorbing gases (e.g., O_3 and NO_2), as well as location- and time-specific properties (e.g., aerosol number size distribution, aerosol optical depth, ground albedo, etc.) to successfully run models involved in the retrieval processes. However, if additional data are available and UV optical properties are retrievable, retrieved UV aerosol optical properties provide more representative input values for UV optical properties needed in surface UV radiation models.

Two such retrieval methods, the single-wavelength method and the optimal estimation method, have been developed and successfully applied in a number of studies [*Goering et al.*, 2005; *Krotkov et al.*, 2005b; *Petters et al.*, 2003; *Taylor et al.*, 2008; *Wenny et al.*, 1998; *Wetzel et al.*, 2003]. Both methods use ground-based measurements of UV irradiance to determine best-fit UV aerosol optical properties. However, each method reaches solutions of UV aerosol optical properties differently. The single-wavelength method use ratios of direct, diffuse, and total (direct plus diffuse) irradiance (e.g., direct-to-diffuse ratio) to solve for UV aerosol optical properties at an individual wavelength, while the optimal estimation method uses both direct and diffuse irradiance to solve optical properties for a set of wavelengths simultaneously. While retrieval results from both methods have been shown to agree well with available ancillary measurements and/or estimates of parameters of interest (e.g., ozone) [e.g., *Goering et al.*, 2005], little work has been done to compare the retrieval results from each method to one another. With retrieval methods as the only means to determining UV aerosol optical properties, it is essential to compare results

from different methods to identify potential inconsistencies that might affect the reliability of results.

The ground-based irradiance measurements at UV wavelengths necessary to run both retrieval methods are widely available through two major networks: the United States Department of Agriculture (USDA) UV-B Monitoring Network (Fort Collins, Colorado) and the National Aeronautics and Space Administration (NASA) Aerosol Robotic Network (AERONET) (Greenbelt, Maryland). In addition to irradiance data, each network provides aerosol optical and physical data obtained via the inversion of collected visible and UV irradiance data. Both the USDA UV-B Monitoring Network and the NASA Aerosol Robotic Network determine AOD at UV wavelengths through simple mathematical relationship of these quantities to irradiance. The nature of the NASA Aerosol Robotic Network's instrumentation allows for the additional retrieval of aerosol number size distributions as well as SSA, g, and refractive index at select visible wavelengths. Both networks have extensive global coverage, allowing for the retrieval of aerosol optical properties at a number of locations that have a variety of characteristic aerosol types.

Accurately modeling changes in the intensity of surface UV radiation is especially important in polluted environments, such as urban areas, where concentrations of photochemically-active atmospheric species and aerosols are high. Elevated aerosol concentrations will enhance the aerosol direct effect in urban regions, both in the visible and UV ranges. Similarly, concentrations of aerosol species that exhibit spectral absorption trends (e.g., soot) will be higher, potentially resulting in additional decreases to UV radiation in urban areas. The additional

attenuation of UV radiation by aerosols will significantly impact the local atmospheric chemistry. While the concentrations of readily-photolyzed species such as NO_2 are higher in urban regions than remote regions, it has been suggested that photolysis rates will change in the presence of aerosols [*Dickerson et al.*, 1997; *He and Carmichael*, 1999; *Liao et al.*, 1999; *Reuder and Schwander*, 1999]. A decrease in photolysis rates (as is expected in the presence of strongly absorbing aerosols [e.g., *He and Carmichael*, 1999]), may increase the transport distance of these photochemically-active species, potentially leading to increased photochemical smog events further downwind of urban centers. Oppositely, increases in photolysis rates (as is expected in the present of strongly scattering aerosols [e.g., *Liao et al.*, 1999]) may increase the frequency and/or intensity of photochemical smog events within urban settings, adding to preexisting health threats that local pollution poses.

This work aims to address both the need for quantifying UV aerosol optical properties in urban regions and the need for an intercomparison of retrieval methods. Two field campaigns, the Megacity Initiative: Local and Global Research Objectives (MILAGRO) conducted in Mexico City, Mexico in March 2006 and the Texas Air Quality Study II/Gulf of Mexico Atmospheric Composition and Climate Study (TexAQS II/GoMACCS) conducted in Houston, Texas in September 2006, provide the opportunity to examine the UV aerosol optical properties in two urban areas. A USDA UV-B Monitoring Network and a NASA Aerosol Robotic Network station were in place during both campaigns thus ensuring irradiance data availability. Additionally, measurements of aerosol chemical and physical properties as well as gas phase chemistry taken during both TexAQS II/GoMACCS and MILAGRO

provide needed model input values. SSA will be retrieved using both the single-wavelength and optimal estimation retrieval methods described in Chapter 3. Results from both retrieval methods for both field campaigns will be compared and reasons for possible discrepancies explored. The results from this study will provide some insight into the general characteristics of the UV optical properties for urban aerosols as well as specific information on the UV optical properties of two major metropolitan centers. Such findings will have tremendous implications for modeling the surface UV irradiance in urban areas, ultimately increasing accuracy in tropospheric photochemistry and UV exposure risk forecasts for these regions.

Table 1.1Values for AOD (τ), SSA (ω), and g as determined in several studies by inversion methods.

	λ(s)	AOD	SSA	g
Wenny et al., 1998	312nm	0.059-0.384	0.75-0.93	0.63-0.76
Petters et al., 2003	300nm, 305nm, 311nm, 317nm, 325nm, 332nm, 368nm	---	0.65-0.99	---
Wetzel et al., 2003	368nm	0.1-0.25	0.63-0.95	---
Krotkov et al., 2005b	368nm	---	0.88-0.95	---

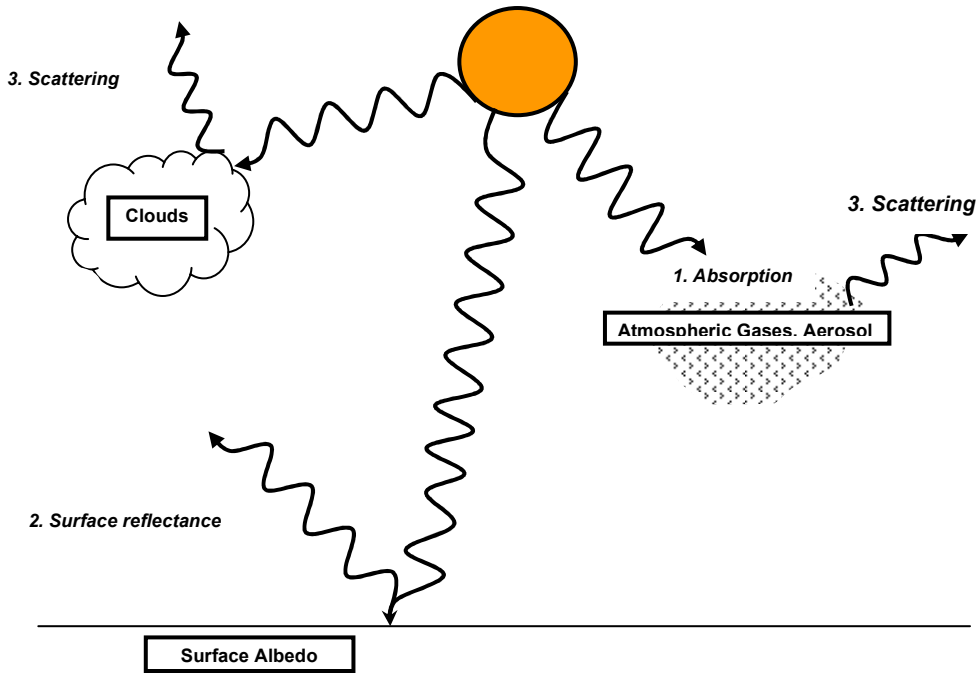

Figure 1.1 A general schematic for radiation in the atmosphere.

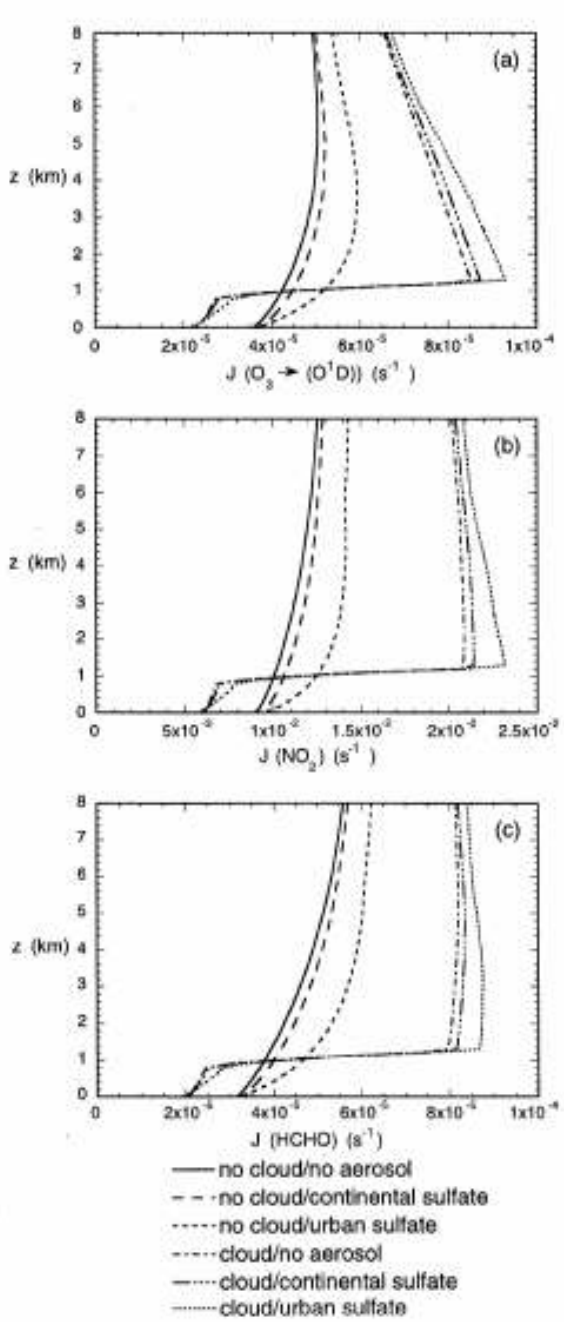

Figure 1.2 Vertical O_3 (a), NO_2 (b), and HCHO (c) photolysis rates determined in the presence of sulfate aerosol.

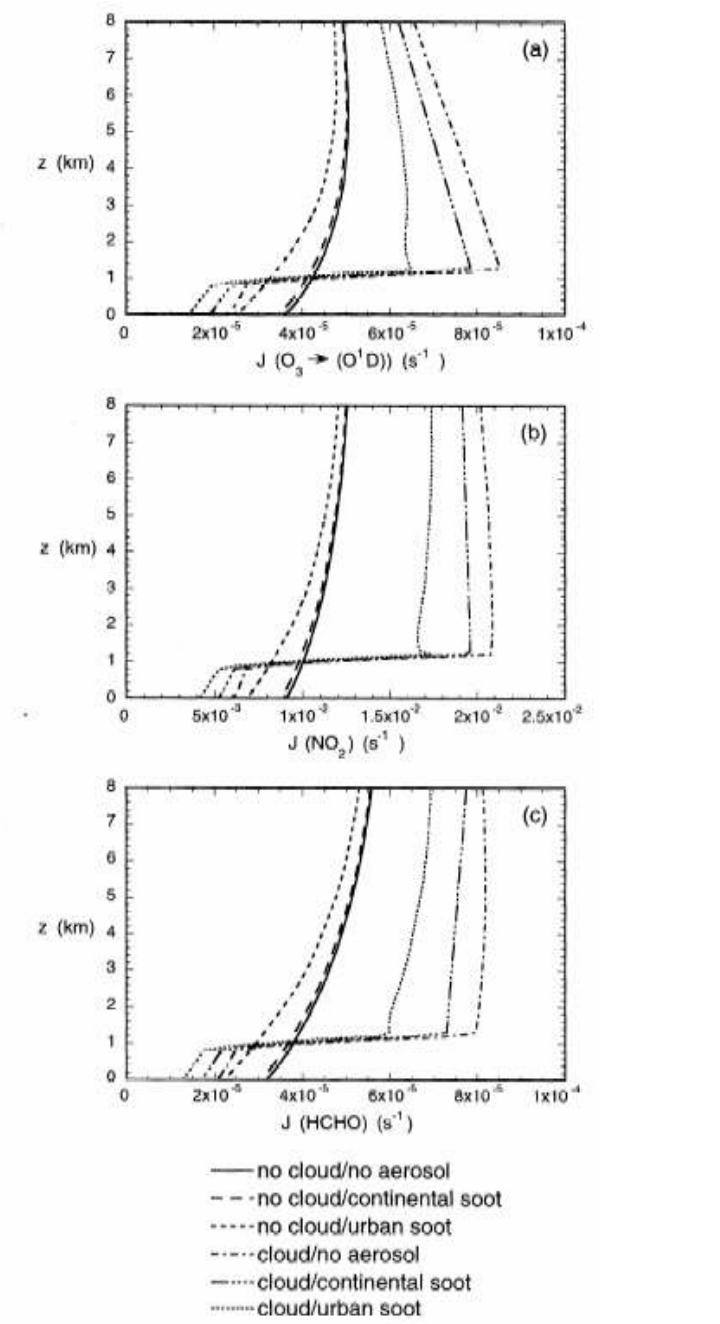

Figure 1.3 Vertical O_3 (a), NO_2 (b), and HCHO (c) photolysis rates determined in the presence of soot aerosol.

2 Measurements and Data Availability

As previously discussed, the potential increase in surface UV radiation due to a thinning stratospheric ozone layer has been well documented [*Blumthaler and Ambach*, 1990; *McKenzie et al.*, 1999]. Such findings, as well as the human and ecosystem health risks associated with UV radiation exposure, have motivated an interest in surface UV irradiance measurement. Two measurement programs, the Aerosol Robotic Network (AERONET) and the USDA UV-B Monitoring Program provide an extensive ground-based network of surface UV radiance (incident radiation into a unit solid angle) and irradiance (incident radiation integrated over all solid angles) measurements. The UV radiance and irradiance measured from these networks provide the data necessary for the retrieval of UV aerosol optical properties [e.g., *Petters et al.*, 2003].

2.1 The USDA UV-B Monitoring Program

The USDA established the UV-B Monitoring and Research Program (henceforth termed the UVMRP) in 1992 to provide a climatology of surface UV radiation within the United States. While the UVMRP primary aim is to examine how fluctuations of UV radiation in time and space relate to agricultural health and production, it also strives to provide information on those atmospheric constituents (e.g., aerosols, clouds, gases) and surface properties (e.g., ground albedo) that alter he surface radiation field [*Bigelow et al.*, 1998]. Currently, there are 37 climatological

sites in place, 32 of which are located in the continental United States, 2 in Canada, 1 in Alaska, 1 in Hawaii, and 1 in New Zealand. Additionally, several temporary sites (termed "research sites") have been set up to measure UV irradiance at the surface during intensive field campaigns.

2.1.1 Instrumentation and Data Collection

Whether climatological or research, each of the UVMRP sites is equipped with a suite of instrumentation used to measure solar radiation. Ancillary measurements of short-wavelength (280nm-360nm) irradiance, ambient conditions, and snow cover are provided by a collocated Yankee Evironmental Systems (YES) (Turner Falls, Massachusetts) UVB-1 broadband meter, a Vaisala temperature-humidity probe, and a downward-looking LI-COR photometer, respectively. A YES UV Multi-Filter Rotating Shadowband Radiometer (UV-MFRSR) and a visible Mult-Filter Rotating Shadowband Radiometer (Vis-MFRSR), manufactured by either YES or Pacific Northwest National Laboratory (Richland, Washington) provide the primary UV and visible irradiance data sets used by the UVMRP. Both instruments operate similarly as outlined in Harrison et al. [1994] with slight differences in instrument characteristics.

A summary of the properties of both the Vis- and UV-MFRSR is shown in Table 2.1. The raw data of the MFRSR instruments are voltages as measured by the horizontal diffuser photodiode detector system of each instrument [*Bigelow et al.*, 1998]. Each shadowband instrument measures at several wavelengths (listed in Table 2.1) with nominal 2nm and 10nm full width at half maximum (FWHM) for the UV-

MFRSR and Vis-MFRSR, respectively. The MFRSR allows for the measurement of total and diffuse voltages through the automatic adjustment of band position with respect to the diffuser during a measurement sequence. Total horizontal voltages are measured when the shadowband is at rest to the side of the diffuser. Diffuse horizontal voltages are determined internally via the addition of a shadowband direct-sun blocking measurement and two additional blocking measurements at 9^{o} off to each side of the direct-sun shadowband position to correct for excess sky blocking during the diffuse measurement [*Harrison et al.*, 1994]. The entire measurement sequence takes 10 and 20 seconds for the Vis-MFRSR and UV-MFRSR, respectively, however an internal microprocessor allows for data averaging over longer time intervals. The subtraction of the diffuse horizontal voltages from the total horizontal voltages yields direct horizontal voltages, which are further corrected to direct normal voltages by the division of direct horizontal voltages by the cosine of the SZA.

Currently two methods are used to calibrate the UV-MFRSR: the lamp method and the Langley regression/analysis method. Lamp calibrations are conducted once prior to the deployment of the instrument at the National Oceanic and Atmospheric Administration (NOAA) Central Ultraviolet Calibration Facility (Boulder, Colorado) using 1000W NIST-traceable lamps to examine and adjust the MFRSR measured voltage. Lamps are place 50cm from the detector and the measured voltages recorded. Spectral response functions (previously determined using methods outlined in [*Bigelow et al.*, 1998]) and the lamp absolute spectral irradiance are used together to determine the effective power of the detector. The division of the MFRSR measured lamp-voltages by the effective power yields

instrument-specific spectral responsivity that can be used to adjusted measured data accordingly [*Bigelow et al.*, 1998].

The Langley regression method is outlined in detail in Slusser et al [2000]. Briefly, values of the calibration coefficient, $V_{o,\lambda}$, are obtained using a modified version of the Beer-Lambert Law (Equation 1.4). Rearranging Equation 1.4,

$$\ln V_\lambda = \ln V_{o,\lambda} - m\tau \qquad 2.1$$

a linear relationship between *m* and the natural log of the measured direct beam voltage at a particular wavelength channel, V_λ , is evident. Thus, plotting *m* versus lnV_λ, yields a line whose slope is optical depth and intercept is the voltage intercept [*Bigelow et al.*, 1998]. This Langley regression method is done twice a day, once in the morning and once in the afternoon, under atmospherically stable conditions and for a range of SZA and therefore *m* values. For the UV-MFRSR, *m* spans from 1.2 to 2.2 (SZA of 33.6^o to 63.0^o) in the Langley regression analysis, a range shorter than what is used for the Vis-MFRSR due to the increase in optical depth at UV wavelengths with increases in ozone absorption and Rayleigh scattering in the UV [*Slusser et al.*, 2000]. A linear fit through a time series of $V_{o,\lambda}$ values for a particular MFRSR instrument at a particular site provides an average value of $V_{o,\lambda}$ used to convert measured and corrected voltages to irradiances as discussed below. However, this fit is not constant with time. Location-specific conditions (e.g., pollution) can cause soiling and/or bleaching of a detector resulting in decreases and increases in $V_{o,\lambda}$ over time, respectively. These new $V_{o,\lambda}$ values are used for the periodic post-collection recalibration of the UV-MFRSR data to ensure data quality.

Thus, unlike the lamp-calibrated data, Langley-calibrated data account for the degradation of the detector over time. Collected raw voltages are sent to the UVMRP located in Fort Collins, Colorado via telephone modems for data corrections and processing.

2.1.2 Data Processing and Products

Both the direct normal and diffuse horizontal irradiances are adjusted to correct for nighttime biases and variable cosine response functions as described in Krotkov et al [2005a]. The corrected voltages (V_λ) are converted to irradiance (I_λ) via the relationship

$$I_\lambda = V_\lambda k \tag{2.2}$$

where k is the calibration factor described by the equation

$$k = \frac{\int I_{o,\lambda} F_\lambda d\lambda}{V_{o,\lambda} \int F_\lambda d\lambda} \tag{2.3}$$

where F_λ is the filter/photodiode spectral response function, $I_{o,\lambda}$ is the extraterrestrial irradiance (the irradiance measured outside Earth's atmosphere), and $V_{o,\lambda}$ is the previously determined calibration coefficient.

In addition to irradiance calculations, corrected voltages are used by the UVMRP in AOD and total ozone column (TOC) retrievals. Total optical depth is determined via the Beer-Lambert law shown in Equation 1.4 for each m (SZA) and using the $V_{o,\lambda}$ determined from the Langley regression analysis. Measured surface pressure and retrieved O_3 are used to calculated Rayleigh and O_3 optical depth, respectively, which are subsequently subtracted from total optical depth to yield

AOD. UVMRP AOD is only calculated for the 368nm and 332nm channels of the UV-MFRSR due to increased error with increased absorption by trace gases (e.g., O_3, sulfur dioxide) at shorter wavelength channels.

TOC is retrieved using the Direct-sun method outlined in Gao et al [2001]. This method employs a version of the Beer-Lambert law modified to solve for TOC as a function of measured voltage, the voltage intercept, AOD, Rayleigh scattering, and SZA for two sets of wavelength pairs. The wavelength pairs of 305-325nm and 311-332nm are chosen based on assumptions of constant aerosol optical properties and a linear relationship between wavelength and Rayleigh scattering. With these assumptions, changes in measured voltage over these wavelength pairs can be attributed to absorption by O_3. The Direct-sun method has been shown to yield TOC values in agreement with those measured by collocated Brewer and Dobson spectrophotometer O_3 measurements [*Gao et al.*, 2001]. TOC retrievals were also shown to be insensitive to variable atmospheric (e.g., aerosol loading, pressure, etc.) and physical (e.g., surface albedo) conditions [*Slusser et al.*, 1999].

2.2 The Aerosol Robotic Network

The Aerosol Robotic Network (AERONET) was established by NASA and Centre National de la Recherche Scientifique (CNRS) (Paris, France) to provide an accessible, spatially and temporally complete data set of aerosol optical and physical properties. Initiated in the mid-1990's, AERONET has expanded internationally to include hundreds of sites world-wide.

2.2.1 Instrumentation and Data Collection

AERONET sites are equipped with the CIMEL Electronique 318A, an automatic sun-tracking spectral radiometer as described in Holben et al [1998]. The instrument has two detectors for the measurement of Sun/aureole and sky radiances. Both are constructed with a quartz window and enhanced silicon detector (designed for 10^{-5} straylight rejection) for the measurement of radiances between 300nm and 1020 nm. Eight ion-assisted deposition interference filters yield radiance measurements at 340nm, 380nm, 440nm, 500nm, 670nm, 870nm, 940nm, and 1020nm with band passes (FWHM) of 2nm for the 340nm channel, 4nm for the 380nm channel, and 10nm for all the visible wavelength channels [*Holben et al.*, 2001]. Sun position is computed internally based on time, latitude, and longitude and subsequently used to position the instrument sensor head.

Field CIMEL spectral radiometers are calibrated biannually at the Goddard Space Flight Center (GSFC) (Greenbelt, Maryland) using a 2m integrating sphere and two reference CIMELs for the adjustment of the wavelength channels and CIMEL $V_{o,\lambda}$, respectively. Integrating sphere measurements are used to determine the precision of the CIMEL via comparison of sphere-measured radiance to CIMEL-measured radiance at four specific wavelengths [*Holben et al.*, 1998]. Field CIMEL $V_{o,\lambda}$ are adjusted so that field CIMEL calculated optical depths match those recorded by the reference CIMEL instruments. Reference CIMEL optical depths are determined using Equation 2.1, with $V_{o,\lambda}$ values obtained during calibration at the NOAA Mauna Loa Observatory (Mauna Loa, Hawaii), and measured raw voltages [*Holben et al.*, 1998]. Using reference CIMEL optical depths, field CIMEL measured

raw voltages, and Equation 2.1 the field CIMEL $V_{o,\lambda}$ values can be adjusted accordingly. To examine the stability of instrument $V_{o,\lambda}$, morning and afternoon Langley calibrations are conducted for operating field CIMEL spectral radiometers automatically. To ensure minimal drift in $V_{o,\lambda}$, the ion-assisted filters are changed every two years [*Holben et al.*, 1998]. The entire calibration process has been shown to yield less than 0.01 and 0.02 uncertainty in AOD at the longer (>440nm) and shorter (<440nm) channels, respectively [*Holben et al.*, 1998].

The CIMEL performs two measurement sequences while operating: direct Sun measurements and sky. Both the direct Sun and sky measurements have several measurement types within the sequences, with measurement type governed by *m* (SZA) and wavelength. Direct Sun measurements record data for all eight wavelength channels and provide the most continuous data set from the AERONET network. The entire direct Sun sequence consists primarily of two measurement types and takes approximately 10 seconds to complete [*Holben et al.*, 1998]. All direct Sun measurements are made with the CIMEL sensor fixed at the sun's azimuth angle while stepping through zenith angle. Standard direct Sun measurements capture radiance measurements for the mid-day hours with a 15-minute data collection time when *m* is two or less. Direct Sun Langley measurements are made every 5 minutes when *m* equals 7 to 5 and every 25 minutes when *m* equals 5 to 2. Triplet measurements are also made throughout the direct Sun measurement sequence, with three measurements taken over one minute to determine the presence of clouds [*Holben et al.*, 1998].

Sky measurements are taken at four of the eight wavelengths: 440nm, 670nm, 870nm, and 1020nm. Similar to direct Sun measurements, the sky sequence includes Langley measurements at large *m* values [*Holben et al.*, 1998]. In addition to Langley, two measurements, the principle plane and almucantar, are standard in the sky measurement sequence and provide the necessary scattering angle information to determine aerosol physical and optical properties [*Holben et al.*, 1998]. Almucantar measurements are made at a fixed zenith angle and azimuth angle with sensor direction varying from 0^o to 359^o from the direct-sun point. A full almucantar rotation takes approximately 40 seconds to complete for all wavelengths and occurs at several specific times during a day: when $m = 4$, 3, 2, and 1.7 as well as hourly between 9 A.M. and 3 P.M., local solar time [*Holben et al.*, 1998]. The principle plane sequence provides additional scattering angle information by measuring over a range of azimuth angle (6^o above and below the direct Sun azimuth angle) for a fixed zenith angle and takes approximately 30 seconds to complete for the four wavelengths [*Holben et al.*, 1998].

2.2.2 Data Processing and Products

Both direct Sun and sky radiance data are used to determine a number of aerosol optical and physical properties. Similar to UVMRP, AERONET total optical depth is determined using the modified Beer-Lambert law (Equation 2.1) using previously derived CIMEL $V_{o,\lambda}$ values (described in Section 2.2.1) and measured V and m values [*Holben et al.*, 2001]. NO_2, O_3, and Rayleigh optical depths are determined from climatological and, when available, measured NO_2 concentrations,

O_3 concentrations, and surface pressure and are subtracted from total optical depth to yield AOD. AOD values are determined for all eight wavelengths for all available direct Sun measurements. CIMEL-derived AOD has been shown to compare well with AOD values calculated from other ground-based measurements [*Schmid et al.*, 1999].

The AOD values calculated from the raw measured voltages are considered Level 1 data as the data points have not been edited for cloud contamination, shifts in $V_{o,\lambda}$ values, and inconsistencies with ancillary measurements. Level 1 AOD values are considered Level 1.5 after passing cloudscreening and quality control algorithms outlined in Smirnov et al [2000] where four checks are applied to every AERONET data set in order to eliminate periods of unrealistic AOD values, such as those produced in the presence of clouds. Instances where calculated AOD values are less than -0.101 imply instrument calibration and correction errors and are automatically eliminated from the data set along with the corresponding radiance measurement. Additional Level 2.0 checks including a temperature sensor check, instrument performance check, and checks against additional data sets (e.g., MODIS, HYSPLIT, etc.) produce AERONET's highest quality-assured data sets.

In addition to AOD, AERONET aerosol size distribution, refractive index, phase function, and single scattering albedo are determined using AERONET sky radiance measurements. The inversion scheme involves the optimal minimization of a solution matrix and is outlined in detail in Dubovik and King [2000] and described briefly here. Ground-measured radiance and optical depth are best described as a

function refractive index (μ), aerosol size distribution ($dV/dlnr$), and surface albedo (A) as seen in the equation

$$I(\Theta;\lambda) = I[\frac{dV}{d\ln r};\mu(\lambda);A(\lambda)] + \Delta(\lambda;\Theta) \quad 2.4$$

$$AOD(\lambda) = AOD[\frac{dV}{d\ln r};\mu(\lambda)] + \Delta(\lambda) \quad 2.5$$

where Δ denotes some degree of uncertainty attributed to instrument error [*Dubovik et al.*, 2000]. Using this concept, values of aerosol size distributions and complex refractive indices restricted by *a priori* constraints are used to calculate radiance, assuming some amount of error. The optimized solution of the resulting solution matrix is considered where the quadratic formula that calculates offsets between measured optical depths and radiance and those modeled based on microphysical properties and the error and variance associated with these microphysical properties is at a minimum.

From these retrieved microphysical properties, scattering ($\tau_{scat}(\lambda)$) and total optical depth as well as phase function ($P(\Theta,\lambda)$) are modeled as a function of size distribution, optical depth ($AOD(\Theta;\lambda;\mu;\rho)$) and scattering cross-section ($K_{scat}(\Theta;\lambda;\mu;\rho)$)) as indicated by the equations

$$\tau_{scat}(\lambda)P(\Theta;\lambda) = \int_{r_{\min}}^{r_{\max}} \frac{C_{scat}(\Theta;\lambda;\mu;\rho)}{g_n(\rho)} x_n(\ln\rho)d\ln\rho \quad 2.6$$

$$\tau_T(\lambda) = \int_{r_{\min}}^{r_{\max}} \frac{AOD(\lambda;\mu;\rho)}{g_n(\rho)} x_n(\ln\rho)d\ln\rho \quad 2.7$$

which are approximated by equations

$$\tau_{scat} \approx K_{scat}(\Theta;\lambda;n;k)x_n \quad 2.8$$

$$\tau_T \approx AOD(\lambda;n;k)x_n \quad 2.9$$

where x_n is aerosol size distribution and n represents the moment (number, radius, surface area, or volume) of the distribution. The dependence of AOD and K_{scat} on scattering angle (Θ), wavelength (λ), complex refractive index (μ), and particle radius (ρ) are approximated by matrices and look-up tables to improve inversion efficiency ([*Dubovik and King*, 2000]. Using these equations, and the additional relationship between τ_{scat}, AOD, and SSA

$$SSA_0^{total}(\lambda) = \frac{\tau_{scat}^{total}}{AOD^{total}} \quad 2.10$$

where *total* is molecular plus aerosol, a solution matrix of aerosol optical properties is obtained and are subsequently used to model radiances. Final inversion products include aerosol 22-bin volume size distributions ($0.05\mu m<r<15\mu m$), effective radius, complex refractive index, asymmetry parameter (determined from the retrieved phase function), single scattering albedo, downwelling/upwelling flux, and top of the atmosphere radiative forcing at sky radiance wavelengths and measurement times.

There are currently two versions of the AERONET inversion scheme: Version 1 and Version 2. Both versions employ the Dubovik and King [2000] inversion, however, the inversion method has been modified to include additional aerosol microphysical properties (i.e., percentage of spherical particles, fine and coarse mode distinction) retrievals in Version 2 [*Dubovik et al.*, 2006]. Furthermore, Version 2 uses MODIS-derived surface reflectances (necessary for modeling

irradiances as seen by Equation 2.4) in the inversion and not a singular assumed value as is done in Version 1 [*Dubovik et al.*, 2006; *Sinyuk et al.*, 2007].

2.3 Data Sets

This work uses data from both AERONET and UVMNP sites as well as additional aerosol and gas measurements for the retrieval of UV aerosol optical properties. Data were obtained during two urban field campaigns described below.

2.3.1 Houston

Data were collected during the Texas Air Quality II/Gulf of Mexico Atmospheric Composition and Climate Study (TexAQS II/GoMACCS) campaign conducted in Houston, Texas in August, September, and October 2006. A UVMRP climatological site was initiated in Houston, Texas at the top of the North Moody Tower (NMT) building (76 meters above sea-level) at the University of Houston (29.710 ^{o}N, 95.34^{o}W) on August 4, 2006 and remains in operation. A UV-MFRSR (serial number 528) was included with the site at set-up and was later switched out with a new UV-MFRSR (serial number 302) on July 26, 2007. Three-minute averaged, lamp-calibrated irradiances and UVMRP AODs from August 5, 2006 to October 7, 2006 were retrieved from the UVMRP website (http://uvb.nrel.colostate.edu/). This period was chosen as it coincides with the intensive field campaign period and thus the period with the richest ancillary data sets. Lamp-calibrated irradiances were chosen for data-set consistency between retrieval methods as described in Chapter 3. Both irradiances and AODs were obtained after UV-MFRSR 528 was replaced by UV-MFRSR 301 to ensure the data

were finalized and would not undergo further adjustments due to recalculated $V_{o,\lambda-}$ values.

Collocated with the UVMRP site on the NMT was an AERONET CIMEL spectral radiometer. Level 2.0 UV and visible AERONET AODs as well as available Version 2, level 2.0 AERONET size distributions and 440nm refractive indices were gathered from this measurement site for the three months of interest from the AERONET website (http://aeronet.gsfc.nasa.gov/). The infrequency of the almuncantar measurements and quality control procedure yielded few final Version 2 inversion results. Of these obtained inversion results, there were only a handful of times in which the full retrieval (refractive index, SSA, etc.) was run, however size distribution data are provided for every inversion run. Table 2.2 summarizes the Version 2 data availability during the Houston campaign. Trace gas concentrations (O_3, NO_2) and surface pressure values needed to run the Tropospheric Ultraviolet model (TUV) used in the retrieval were also obtained from AERONET. The reported trace gas concentrations and surface pressure are climatological and measured values collected from satellite retrievals and NCEP/NCAR surface station reanalysis, respectively.

Additional aerosol physical data were obtained for the August-October 2006 period. Such data are necessary to successfully run the retrieval and to understand the possible relationships between particle composition and size and aerosol UV optical properties. Scanning Mobility Particle Sizer (SMPS) size distributions were measured at NMT and were provided by the Brooks research group of Texas A&M University (College Station, Texas). Number size distributions are measured every

seven minutes and cover a range of diameters from 0.011μm to 1.083 μm. The SMPS data set extends from August 18, 2006 at 20:42 CST to October 12, 2006 at 19:12 CST with periods of missing data from August 20, 2006 12:06 CST to August 23, 2006 7:19 CST and from August 24, 2006 at 13:30 CST to August 25, 2006 at 17:55 CST.

2.3.2 Mexico City

Aerosol optical and irradiance data measured during the Megacity Initiative: Local and Global Research Observations (MILAGRO) campaign conducted in Mexico City, Mexico in March 2006 were also collected. A UVMRP research site set up for measurement during the MILAGRO campaign was in operation from March 11, 2006 to April 1, 2006 at the MILAGRO field site T1 (19.7^{o}N, 98.99^{o}W, 2270m elevation). One UV-MFRSR at the site during the campaign was used to produce irradiance measurements every 20 seconds. Irradiances (lamp-calibrated) and AODs from March 12, 2006 to March 31, 2006 were obtained from the UVMRP website. Irradiance (and therefore AOD) data were not available for March 16th, March 26th, or March 28th.

A Temporary AERONET site was initiated in Mexico City at a location the T1 site and was in operation for the duration of the MILAGRO campaign (March 6, 2006 to April 1, 2006). Level 2.0 AOD data are available for most days during the MILAGRO campaign with the exception of March 8th, 9th, 25th, and 26th. Additionally, surface pressure, NO_2, and O_3 data were retrieved from this AERONET data set and subsequently used in as input to TUV. While version 2 level 2.0

inversion data were available for several days during the MILAGRO campaign, these data were not obtained as the full single-wavelength retrieval (discussed in Chapter 3) was not performed for MILAGRO.

Table 2.1UV- and Vis-MFRSR general instrument properties.

	UV-MFRSR	Vis-MFRSR
Center Wavelengths	300nm, 305nm, 311nm, 317nm, 325nm, 332nm, 368nm	415nm, 500nm, 610nm, 665nm, 860nm, 940nm
Diffuser Material	Teflon	Spectralon
Standard Measurement Time	20 seconds	10 seconds
Full width at half maximum	2nm	10nm

Table 2.2AERONET Version 2, level 2.0 inversion data availability during the TexAQS II/GoMACCS field campaign in Houston, Texas.

	Days With Available Size Distribution ONLY	Days With Available Size Distribution and Refractive Index
August	10,11, 12, 13, 15, 16, 18, 20, 25, 30, 31	29
September	14, 19, 20, 25, 26, 27, 30	1, 2, 3, 13, 28
October	7	5, 6

3 Methods for the Retrieval of Aerosol Ultraviolet Optical Properties

In this work, UV SSA were retrieved for several days during each of the urban field campaigns. Retrievals were done using two retrieval methods: the single-wavelength method and the optimal estimation method. Both methods are widely used for the retrieval of aerosol UV optical properties and have been shown to yield reasonable results (e.g., Taylor et al. [2008], Petters et al. [2003]). However, the two methods have yet to be compared with one another. Such a comparison is necessary in order to properly assess the accuracy of the retrieved results. Comparisons between the single-wavelength and the optimal estimation methods were made in this work using SSA values retrieved using both methods. Descriptions of the single-wavelength and optimal estimation retrieval procedures are provided below.

3.1 Models

3.1.1 General Radiative Transfer in the Atmosphere

The extinction of monochromatic radiation (dI_λ) over a path of length ds is described by the equation

$$\frac{dI_\lambda}{ds} = -b_{ext} I_\lambda \qquad 3.1$$

whose solution is the Beer-Lambert Law (Equation 1.3). Equation 3.1 describes the direct beam of monochromatic radiation as it does not account for atmospheric

scattering. However, in order to accurately depict the change in the intensity of monochromatic radiation, multiple scattering processes must be considered in addition to extinction. Thus, a more exact representation of radiative transfer in the atmosphere is given by the equation

$$\frac{dI_\lambda}{ds} = -b_{ext}[I_\lambda - H_\lambda] \tag{3.2}$$

where H_λ represents emission due to multiple scattering. The application of the plane-parallel atmosphere approximation allows for the measurement of linear distances normal to the plane of stratification, thus allowing for the measurement of changes in monochromatic radiation intensity with respect to the surface. Using this approximation, the radiative transfer equation can then be written

$$\cos\theta \frac{dI_\lambda(z;\theta;\phi)}{b_{ext}dz} = -I_\lambda(z;\theta;\phi) + J_\lambda(z;\theta;\phi) \tag{3.3}$$

where z is altitude, θ is SZA, and ϕ is azimuth angle.

3.1.2 The Tropospheric Ultraviolet Model

The Tropospheric Ultraviolet model used in both retrieval methods of this work was developed by Dr. Sasha Madronich of the National Center for Atmospheric Research (NCAR) and is available for download on the web (http://cprm.acd.ucar.edu/Models/TUV/). TUV is a one-dimensional, radiative transfer code used to calculate direct, diffuse, and/or total irradiances using a set of user-defined surface atmospheric and physical inputs listed in Table 3.1.

In addition to the inputs, the user must also specify the range and desired number of vertical layers and wavelengths so that appropriate space and wavelength

grids may be created in TUV. Such grids are important as they provide the necessary means to scale surface data (i.e., AOD, NO_2, O_3, pressure) to a vertical profile and wavelength range. Assuming the appropriate wavelength-dependent absorption cross-sections of the respective gases, column trace gas concentrations and surface pressure data are used to determine NO_2, O_3, SO_2, and Rayleigh optical depths which are subsequently scaled to the U.S. Standard Atmosphere (1976) profile to yield altitude-dependent gaseous absorption and scattering. AOD is scaled similarly, however instead of using the U.S. Standard Atmosphere, a predefined vertical distribution is used. The default vertical aerosol profile used to scale AOD is the continental aerosol distribution profile reported at 340nm in Elterman et al [1969], however the user may specify an alternative profile if desired. If the AOD profile is at a wavelength different from that of the input AOD, an Angstrom exponent calculation is performed using the user-specified Angstrom exponent. Once the profile is scaled to the input AOD, another Angstrom exponent calculation is performed to produce a vertical distribution of AOD at the user-specified wavelength(s).

The radiative transfer equation may be solved using either the 2-stream approximation or the discrete ordinate method (DISORT) in TUV both of which assume a two-directional (upwards and downwards) beam. There are nine 2-stream method options in TUV, including the Delta-Eddington approximation for a 2-stream radiative transfer system outlined in Toon et al [1989]. Unlike the 2-stream method, the discrete ordinate method allows for multiple scattering to occur within the column through the discretization of the radiative transfer equation. The number of scattering

angles considered in the code are determined from a user-specified stream number, which is an even number ranging from 2 to 32. In addition to irradiances, the model can be set up to calculate actinic fluxes with additional calculations of indices used in the evaluation of human exposure risks including UV-B and UV-A dose rates, DNA damage, CIE human erythema, and the UV index.

3.1.3 Mie Code

A Mie code is used in this work in the full single-wavelength retrieval method as is discussed later. The code uses requires inputs of particle diameter and number concentration, complex refractive index, and wavelength to solve the Lorenze-Mie scattering equations and assumes all particles are spherical.

The particular Mie code used here determines the scattering (Q_{scat}), absorption (Q_{abs}), extinction (Q_{ext}), backscattering fraction (Q_{back}), backscattering in the 180^o direction (Q_{180}), nephelometer scattering (Q_{neph}), and nephelometer backscattering fraction ($Q_{nephback}$) efficiencies. These output are then used to compute additional aerosol optical parameters. For simplicity's sake, only scattering, absorption, and extinction will be discussed here, though the following relationships may apply to all efficiencies. Scattering, absorption, and extinction efficiencies are related to the scattering, absorption cross-sections (C_{scat}, C_{abs}, C_{ext}) by the equations

$$C_{ext} = Q_{exy}\pi\frac{D_{p,i}^{\ 2}}{4} \quad 3.4$$

$$C_{abs} = Q_{abs}\pi\frac{D_{p,i}^{\ 2}}{4} \quad 3.5$$

$$C_{scat} = Q_{scat}\pi\frac{D_{p,i}^{\ 2}}{4} \quad 3.6$$

where $D_{p,i}$ is particle diameter of size bin, i. Furthermore, the C_{scat}, C_{abs}, and C_{ext} are used to calculate scattering, absorption, and extinction coefficients (b_{ext}, b_{abs}, and b_{scat}) via the relationship

$$b_{ext} = C_{ext} \bullet N_i \quad 3.7$$

$$b_{abs} = C_{abs} \bullet N_i \quad 3.8$$

$$b_{scat} = C_{scat} \bullet N_i \quad 3.9$$

where N_i is the number concentration in bin i. The efficiencies may also be used to determine the volumetric optical properties which represent the optical properties for a distribution of aerosol. Volumetric SSA ($\{\omega_\lambda\}$) and g ($\{g_\lambda\}$) are computed using the equations outlined in Wendisch et al [2005]

$$\{\omega_\lambda\} = \frac{\int \omega_\lambda(D')b_{ext,\lambda}(D')d\log D'}{\{b_{ext}\}} \quad 3.10$$

$$\{g_\lambda\} = \frac{\int g_\lambda(D')b_{scat,\lambda}(D')d\log D'}{\int b_{scat,\lambda}(D')d\log D'} \quad 3.11$$

where $\{b_{ext}\}$ is the volumetric extinction coefficient described by the equation

$$\left\{b_{ext,\lambda}\right\} = \int b_{ext,\lambda}(D')d\log D' \qquad 3.12$$

3.2 Data Selection

In order to ensure high quality retrievals, several data quality criteria were set-up to screen out irradiance data that would yield unphysical results. Retrievals were only run for days during both TexAQS II/GoMACCS and MILAGRO that exhibited periods of cloud-free conditions, high AOD, and SZAs less than 65^{o}.

3.2.1 Cloud-Free Criteria

Clouds frequently appear in AOD sets derived from irradiance measurements and are represented by unphysically large AOD values. In order to ensure the integrity of the retrieved aerosol optical properties, these cloud-contaminated data must be removed prior to running the retrieval for a data set. Several cloudscreening algorithms have been developed to do this, however these algorithms have varying success. As discussed below, the cloudscreening algorithm of the OE method does not sufficiently remove data likely collected in the presence of the clouds and is therefore deemed unreliable. The cloudscreening algorithm used by AERONET has the opposite problem; while the algorithm successfully screens out cloud-contaminated data, it also appears to remove useful data leaving little data to be used in analysis (Figure 3.1).

The visual inspection of irradiance profile or cloud camera data has been successfully used in previous studies for the removal of cloud-contaminated data [*Petters et al.*, 2003; *Wetzel et al.*, 2003]. In this study, the 368nm direct irradiance profile for each day during each campaign was examined in order to properly remove

the influence of clouds in the TexAQS II/GoMACCS and MILAGRO data sets. Periods were considered cloud-free if the 368nm direct irradiance profile exhibited the characteristic smooth, bell-shaped curve (Figure 3.2). The 368nm direct irradiance profiles from several days and partial days during both campaigns were characterized as cloud-free based on the profile criteria and are listed in Table 3.2.

3.2.2 AOD Criteria

Once the cloud-free days and partial days were selected from both campaigns, the 368nm AOD values were examined for each day. Several studies have shown difficulty in retrieving aerosol optical properties at low values of AOD; Krotkov et al. [2005b] determined a cut off 440nm AERONET AOD of 0.4 for the retrieval of aerosol optical properties while Wetzel et al. [2003] were unable to retrieve 368nm SSA at AOD values less than 0.1 under high surface albedo conditions due to the resulting effect on diffuse irradiance.

This effect is largely explained by the relationship between AOD, SSA and the direct-to-diffuse ratio (DDR), or the ratio of direct irradiance to diffuse irradiance. As shown in Figure 3.7, as AOD decreases, DDR becomes increasingly less sensitive to values of SSA and the best-fit SSA is not sufficiently constrained. This decrease in the sensitivity to DDR is strongest below an AOD of 0.2 (Figure 3.7). Thus, this work defines 0.2 as the lower 368nm AOD limit and cloud-free periods that have an average AOD below 0.2 are not used in the retrieval. Those days from TexAQS II/GoMACCS and MILAGRO that pass the AOD criteria are summarized in Table 3.3.

3.2.3 Solar Zenith Angle Criteria

Both the AERONET CIMEL and the UVMRP UV-MFRSR have ideal SZA ranges at which they operate. As previously stated, AERONET almucantar measurements require larger SZAs (>45^{o}) and thus sky inversion data availability is limited to larger SZAs [*Dubovik and King*, 2000; *Dubovik et al.*, 2000]. Oppositely, the UV-MFRSR-produced irradiances and AODs are most accurate at SZA smaller than 70^{o} due to increases in cosine correction errors with increases in SZA [*Krotkov et al.*, 2005a]. Keeping these instrument properties in mind, SSA retrievals using UVMRP-derived AODs were limited to times with SZA less than 65^{o}.

3.3 Single-wavelength Retrieval Method

3.3.1 Previous Work

The single-wavelength method used here is similar in design to those methods used successfully in a number of previous studies [*Krotkov et al.*, 2005b; *Petters et al.*, 2003; *Wenny et al.*, 1998; *Wetzel et al.*, 2003]. Such retrieval methods commonly involve iterations between a radiative transfer code and a Mie code in order to match modeled irradiances or irradiance ratios to measured irradiances or irradiance ratios.

Wenny et al [1998] employed this procedure for the retrieval of SSA and g at 312nm over a layer of atmosphere extending from the top of a mountain to a valley floor. Retrievals were done using aerosol size distributions measured using a Differential Mobility Particle Sizer, an assumed imaginary refractive index (real part held fixed at 1.5), and AOD at 312nm calculated from AODs determined from an on-site Vis-MFRSR via the extrapolation of the Angstrom exponent. A radiative transfer

code used first-guess values for SSA and g and the AOD at 312nm to calculate transmission at 312nm where transmission is simply described by the equation

$$T = \frac{I_{out}}{I_{in}} \tag{3.13}$$

where I_{out} is the irradiance measured at the based of a layer of atmosphere and I_{in} is the irradiance measured at the top of the layer. This value was then compared to a transmission value calculated from the ratio of irradiance measured by a Yankee Environmental Systems UVB-1 at the valley site divided by the UVB-1 at the mountain site. The radiative transfer code was looped until the code-calculated transmission matched this transmission calculated from the data. The values for g and SSA at which the two values for transmission converged were then used as "true" values in the Mie code. Using the measured size distributions and these "true" g and SSA values, the Mie code was looped over imaginary refractive indices until calculated values of SSA and g matched these "true" values to obtain a best-fit imaginary refractive index.

A similar method was used in Krotkov et al [2005b]. In the study several different ratios of transmittances were modeled using a radiative transfer code with a Mie code embedded within it at UV-MFRSR wavelengths. The transmittance ratios included the diffuse-to-direct ratio (*DDR*), the diffuse fraction (D_T), and the total transmission (T) which are described by the following equations

$$DDR = \frac{T_{DH}}{T_{DN}} \quad 3.14$$

$$D_T = \frac{T_{DH}}{T_{DN}} \quad 3.15$$

$$T = \frac{V_T}{V_o} \quad 3.16$$

where T_{DN} is the direct irradiance, T_{DH} is the diffuse irradiance, V_T is the measured transmittance in voltage, V_o is the voltage intercept. Such ratios are used to eliminate the potential errors associated with the UV-MFRSR calibration coefficient.

The transmittance ratios were modeled by varying the imaginary part of the refractive index, *k*. All other input variables (e.g., surface albedo, aerosol extinction optical depth, asymmetry parameter, aerosol vertical distribution, real part of the refractive index, size distributions) were constrained using ancillary measurements taken at the Goddard Flight Space Center, CIMEL-derived parameters (AOD, g, *n*, and $n(D_p)$) or assumptions (e.g., no wavelength dependence of the real part of the refractive index) thereby allowing *k* to be the only adjustable variable in the radiative transfer code. A best fit *k* was determined at the point where modeled transmission ratios matched the measured ratios. Values of *k* were then used in the Mie code to determine best fit SSA and g, using the AERONET size distributions and real part of the refractive index.

A single-wavelength method was also used by Petters et al [2003], however the retrieval procedure differs slightly from the previously discussed studies. Unlike Wenny et al [1998] and Krotkov et al [2005b], Petters et al [2003] determined only SSA using only TUV. TUV 4.1 was used to determine aerosol single scattering

albedo (SSA) at all UV-MFRSR wavelengths through the comparison of modeled DDR to measured DDR. TUV inputs of AOD, g, surface albedo, and TOC were set to fixed values thus allowing SSA to be the only variable. AOD inputs were taken at 340nm as determined from the Angstrom exponent (calculated using the 4 longer wavelengths of the UV-MFRSR). The asymmetry parameter was assumed to be 0.70 as this value was deemed appropriate for the measurement site based on previous studies [*Wenny et al.*, 1998] and reported values [*Madronich*, 1993]. Surface albedo was assumed to be 0.04 a value consistent with values for albedo in the UV over grassy surfaces. Like AOD, TOC was determined from the UV-MFRSR using a retrieval method outlined in Wenny et al. [1998]. All calculations were done at a solar zenith angle of 45 degrees.

3.3.2 The Partial and Full Single-Wavelength Methods

A schematic of the single-wavelength method used in this work is shown in Figure 3.3. This method is a combination of the procedures from all three previously-mentioned studies. TUV Version 4.4 was modified to solve for the direct-to-diffuse ratio (DDR) which is described as the ratio of the direct normal (DN) irradiance to the diffuse horizontal (DH) irradiance

$$DDR = \frac{I_{DN}}{I_{DH}} \tag{3.17}$$

As is explained in Krotkov et al [2005b], using ratios is ideal for such retrieval methods as they eliminate the possible errors associated with the calculated UV-MFRSR $V_{o,\lambda}$. The TUV-calculated direct irradiance was divided by the cosine of the SZA to maintain consistency with the UV-MFRSR lamp-calibrated irradiance data.

Values of DDR were calculated using the 4-stream discrete ordinate method, over 80 equally-spaced vertical layers, for 368nm and 332nm to correspond with the UV-MFRSR measurements for each field campaign. For this work, the default Elterman et al [1969] profile with input AOD values at 368nm and 332nm was used. Location-specific TUV inputs for each field campaign location are listed in Table 3.4.

As indicated by Figure 3.3, the single-wavelength method used here consists of two parts: a partial retrieval phase, and a full retrieval phase, both of which compare the modeled DDR values to measured DDR values (calculated from the UVMRP lamp-calibrated irradiance data sets) to determine UV SSA. The partial retrieval phase was done on days that passed the previously mentioned criteria and follows a procedure similar to that used in Petters et al [2003]. The TUV code was set up to loop over 52 values for SSA ranging from 0.5 to 1.0 (at 0.01 steps) and 32 values for g ranging from 0.6 to 0.9 (at 0.01 steps). These SSA and g ranges were chosen as they are values relevant for atmospheric aerosol [*Madronich*, 1993]. In addition to the location-specific inputs, a TUV input file was created for each day and included AOD, O_3 column concentration, NO_2 column concentration, surface pressure, and Angstrom Exponent for each UV-MFRSR time step (every 3 minutes for the TexAQS II/GoMACCS data sets and every 1-minute for the MILAGRO data sets). As stated in Chapter 2, the TexAQS II/GoMACCS and MILAGRO inputs of NO_2, O_3, and surface pressure data were all daily-averaged climatological or, when available, measured AERONET values. UVMRP AOD values at 368nm and 332nm provided the necessary AOD inputs. The Angstrom exponent is irrelevant for single-

wavelength methods and was therefore set to a value of 1 for both wavelengths and both field campaigns.

For both field campaigns and both wavelengths, DDR was calculated for all possible SSA and g pairs for each of the UV-MFRSR data points yielding 1612 DDR calculations for each time interval. These 1612 modeled DDR values were compared to the measured DDR value corresponding to the time interval. Values of SSA were considered "good" if the combination of the variables (along with the previously mentioned inputs) yielded less than 1% relative error between modeled and measured DDR (DDR_{TUV} and DDR_{UVB}, respectively) for the given range in g values where relative error (δ) is

$$\delta = \frac{\left| DDR_{UVB} - DDR_{TUV} \right|}{DDR_{UVB}} \times 100 \qquad 3.18$$

This percent was chosen to account for error in input values as well as error in the UV-MFRSR irradiance measurements. Values of g were not retrievable using the partial single-wavelength method as they were not constrained by additional aerosol data (e.g., size distribution, refractive index). However, the range of g values used in the analysis (0.6 to 0.9) represents an atmospherically-relevant range and yielded fairly constrained retrieved SSA values.

In addition to meeting the previously discussed criteria, an AERONET 440nm refractive index was required in order to run the full retrieval phase of the single-wavelength method. The full retrieval was only run for one day during the TexAQS II/GoMACCS campaign (September 13th) to test the effects of size distribution, AOD, and surface albedo on retrieved SSA as described in Chapter 4.

The full retrieval phase uses a Mie code and TUV to determine a best-fit SSA. The first step in the full retrieval used a Mie code to determine unique pairs of g and SSA for the specified size distribution and refractive index. Similar to Krotkov et al [2005b], the real part of the refractive was assumed not to vary with wavelength. Thus AERONET *n* at 440nm (n_{440}) was used as the *n* for 368nm and 332nm. To test this assumption, the Mie code was looped over a range of *n* and *k* values for both 368nm and 332nm and the resulting effects on SSA and g were evaluated. As is shown in Figure 3.4, SSA exhibits more sensitivity to *k* than *n*, changing about 0.4 with a 0.1 change in *k*. Oppositely, g is more sensitive to *n*, however the change in g over a sizeable range of *n* values (1.30 to 1.60) is much smaller than the change in SSA (~0.01) (Figure 3.5). Thus, the assumption of a fixed *n* is taken to be acceptable. A constant value of *n* was only assumed to exist for a two-hour period before and a two-hour period after the AERONET *n* value was recorded as it is unlikely the aerosol type remains constant for a longer period of time.

Both AERONET and SMPS size distribution data were used in the Mie code to test the effects of a coarse mode on the retrieved optical properties as is discussed in Chapter 4. Using these inputs, the Mie code was set up to loop over 100 *k* values, for each of which volumetric SSA and g were calculated. Each SSA and g pair was assumed to be unique to the size distribution and the refractive index. Volumetric SSA and g were used as inputs in TUV along with the previously described TUV input files of AOD, NO_2, O_3, surface pressure, and Angstrom exponent. During the full retrieval phase, TUV was set up to determine DDR for all 100 of the SSA and g pairs for each size distribution. These DDR values were subsequently compared to

the corresponding measured DDR value and a relative error determined using Equation 3.12. Best-fit SSA values were determined where the relative error between modeled and measured DDR was at a minimum. The full retrieval phase was performed for all possible combinations of the two available size distribution data sets (SMPS and AERONET) and two values for AOD: those determined by the UVMRP and those determined using the AERONET Angstrom extrapolation method outlined in Krotkov et al [2005a]. Additionally, full retrievals were run using three different surface albedo values to examine the effect of surface albedo on retrieved SSA and g values. The results from all full retrieval input (size distribution, AOD, surface albedo) sensitivity tests are reported in Chapter 4.

3.3.3 Single-wavelength Sensitivity Studies

In addition to the previously mentioned tests of the impact of various choices for some TUV inputs on best-fit UV optical properties, the relative sensitivities of AOD and surface albedo to the other aerosol optical inputs were tested in TUV. The accuracy in both AOD and surface albedo values used in the partial wavelength method is unknown. It is therefore important to understand how the TUV model responds to large, but atmospherically-relevant ranges, in both parameters with respect to those input values not constrained (SSA and g). The sensitivity of the TUV-calculated DDR to trace gas (NO_2, O_3) concentrations and surface pressure was also examined. These sensitivity tests provided information regarding the effects of the potential error associated with using multiple data sets to obtain the certain input values. All sensitivity studies were done at both 332nm and 368nm and were

completed using the Houston location inputs and a TexAQS II/GoMACCS day and SZA (September 13, 2006 at 46.97^{o}). A list of the additional default input parameters used in the sensitivity analysis can be found in Table 3.6.

AOD

As discussed previously, there is some concern regarding the accuracy and stability of the UV-MFRSR $V_{o,\lambda}$. Inaccurate $V_{o,\lambda}$ values lead to inaccurate optical depth values which ultimately yield inaccurate AOD values. To examine the effects of the potential error associated with the UVMRP AOD, TUV was set up to calculate DDR over a range of AOD spanning from 0 to 1.1 for both 332nm and 368nm. The relative sensitivity of DDR to AOD compared to the other three aerosol optical inputs (SSA, g, and Angstrom) is seen in Figures 3.6 and 3.7. DDR clearly exhibits more sensitivity to AOD with respect to other aerosol optical inputs as the DDR changes more rapidly with a 1.1 increase AOD (-2.3 and -1.2 for 368nm and 332nm, respectively) than with 0.5 increase SSA (DDR decreases of 0.75 and 0.46 for 368nm and 332nm, respectively), 0.3 increase g (DDR decreases of 0.1 and 0.05 for 368nm and 332nm, respectively), or increase Angstrom (no change in DDR for 368nm or 332nm) for both wavelengths. This emphasizes the need for accurate AOD values for input into the partial single-wavelength retrieval as subtle changes in AOD may results in notable changes to the DDR and thus notable changes in the ranges of SSA values.

Surface Albedo

In addition to the aerosol physical inputs, the effects of a variable surface albedo on DDR was examined. TUV was set to loop over 10 values of surface

albedo, ranging from 0 to 1, a range spanning all possible terrestrial surface albedos. The change in DDR with a 0.1 increase in surface albedo (-0.26 and -0.17 for 368nm and 332nm, respectively) is greater than that between DDR and g, however, the DDR is still most sensitive to AOD and SSA for both wavelengths (Figure 3.8 and 3.9).

This sensitivity of DDR to surface albedo is of concern in the retrieval of aerosol properties, as accurate measurements of surface albedo in the ultraviolet range are fairly limited; while several studies report values for UV surface albedo over specific surfaces (e.g., asphalt, grass) [e.g., *Webb et al.*, 2000], there are few measurements of UV surface albedo for an area that includes multiple surface types. Such information is particularly important for studies involving surface irradiance measurements as it is this integrated surface albedo that changes the radiation field and not the localized albedos of specific surfaces. To address this issue, the albedos of specific surfaces found in urban areas were examined to evaluate the effects of the urban settings of both field campaigns on the DDR. Castro et al [2001] reported broadband UV surface albedos ranging from approximately 0.01 to 0.1 for several urban surface types including asphalt, cement, and mixtures of building and asphalt. This range is consistent with albedo values of similar surfaces measured in additional studies [*Madronich*, 1993; *Webb et al.*, 2000]. Based on this range, a surface albedo of 0.05 was chosen to represent an aerial average of surface albedo in urban areas and was used in TUV for both wavelengths and both campaigns.

Trace Gas Concentrations and Surface Pressure

To identify the possibility of error from the use of AERONET climatological trace gas concentration and surface pressure data sets, TUV was set up to loop over

atmospherically-relevant concentrations of NO_2, O_3, and surface pressure for both 368nm and 332nm and the resulting DDR values examined. NO_2 and O_3 are the strongest gaseous attenuators in the UV, however neither are particular strong absorbers of the wavelengths of interest. In TUV variations in NO_2 of nearly a factor of 10 (0.1 Dobson Units (DU) to 0.95 DU) only resulted in changes to the DDR by 0.005 at 368nm 0.002 at 332nm (Figure 3.10). O_3 absorption is maximum in the UV-B region (280nm to 315nm) and therefore has no discernable affect on the DDR at either 368nm or 332nm as is seen in Figure 3.10. While changes in the DDR at both wavelengths are more pronounced with changes in surface pressure, the decrease in the DDR for each wavelength is small for a substantial change in pressure (-0.083 and -0.062 for 150 mb increase in pressure at 368nm and 332nm, respectively). It was therefore assumed that using different data sets for trace gas concentrations and surface pressure would not introduce a large source of error into the retrieval of SSA.

3.4 Optimal Estimation Retrieval Algorithm

In addition to the single-wavelength retrievals, an Optimal Estimation (OE) retrieval algorithm was used in this work to retrieve SSA for both TexAQS II/GoMACCS for the comparison of retrieval methods. The OE algorithm used was developed at Colorado State University (Fort Collins, Colorado) by Christian Goering and Thomas Taylor. The theory behind the OE algorithm used here is similar to other such algorithms used to determine precipitation and cloud microphysical properties [e.g., *L'Ecuyer and Stephens*, 2002] but has been modified for the specific retrieval of aerosol UV optical properties and TOC [*Goering et al.*, 2005; *Taylor et al.*, 2008].

3.4.1 OE Algorithm Theory

Following Rodgers [2000], the OE algorithm is built from the relationship between a set of measured observations (y) and a set of retrieved properties or a state vector ($\hat{x}$)

$$y = F(\hat{x}, \beta) + \varepsilon \tag{3.19}$$

where F represents a forward model, b is a set of fixed model inputs, and ε is error associated with fitting the state vector to the observations. In order to deduce the values of the state parameters, an inversion method is required. Such a system is solvable in principle using linear algebra, however the complexities associated with a real system, such as the atmosphere, require the application of a framework designed to tackle such a system. To address this issue, the OE algorithm uses Bayes' theorem to apply probability distribution functions (PDFs) to the measurement space, state space, and a combination of the measurement and state spaces to determine a best-fit solution. Assuming these PDFs are normal and using the maximum *a posteriori* linear optimal estimation technique, the most probable solution can be found by the minimization of a scalar cost function

$$\Phi = (y - F(\hat{x}))^T S_y^{-1} (y - F(\hat{x})) + (\hat{x} - x_a)^T S_a^{-1} (\hat{x} - x_a) \tag{3.20}$$

where y is the measurement, $\hat{x}$ is the state vector, x_a is the vector of *a priori* values for the state parameters, S_y is the covariance of the measurements, S_a is the covariance of the *a priori* values, and $F(\hat{x})$ are the contribution functions from the forward model (e.g., irradiance calculated from retrieved state parameters). In essence, the scalar cost function is a measure of the difference between state parameters and *a*

priori parameters and forward model results and measurements, thus yielding the best-fit solution where the cost function is at a minimum. In order to properly reach a solution the Newtonian iteration method was used to ensure convergence of the solution yielding an ultimate solution described by the equation

$$\hat{x} = \hat{x}_{i-1} + \hat{S}(K^T S_y^{-1}(y - F(\hat{x}_{i-1})) + S_a^{-1}(x_a - \hat{x}_{i-1})) \quad 3.21$$

where i is the number of iterations. $\hat{S}$ represents the error covariance matrix which is a combination of the error associated with the measurements and *a priori* parameters and is described by the equation

$$\hat{S} = (S_a^{-1} + K^T S_y^{-1} K)^{-1} \quad 3.22$$

K is the Jacobian weighting matrix of state parameters with i rows and j columns

$$K_{ij} = \frac{\delta F_i(x)}{\delta x_j} \quad 3.23$$

In addition to retrieved parameters, the OE algorithm calculates and outputs a suite of diagnostics useful for the determination of the validity of the retrieved parameters including a parameter used to examine the statistical significance of the OE algorithm result: the chi-squared (χ^2) statistic. χ^2 is identical to the cost function (Equation 3.17), and thus assuming a normally distributed population, χ^2 values can be used to examine the validity of retrieved parameters allowing for the elimination of retrieved parameters that are unphysical, such as those that include contamination from clouds. The user may specify the χ^2 criterion, with options including the 95%, 98%, and 99% threshold levels. Additional outputted diagnostic parameters include: the covariance error which describes the overall error associated with the retrieved

parameters in percent, the Gain and A-matrices outputted which provide information regarding how much the measurement/model error and the *a priori* values of the state parameters contribute to the overall solution, and degrees of freedom and information content associated with the mathematical system.

The OE algorithm is set up to run a maximum of five Newtonian iterations to save computational time. If a retrieval calculation does not converge in five iterations, it is flagged as poor and the data time interval skipped. This value of five was chosen based on a number of sensitivities studies as described in Taylor [2006].

3.4.2 The Forward Model

The forward model used in the OE algorithm is TUV Version 4.2. The TUV input file was modified for use in the OE algorithm as outlined in Taylor [2006]. It is important to note that the version of TUV in the OE algorithm is different than that used in the single wavelength retrieval method (TUV 4.4). However, the two versions differ only in the photochemical reactions considered for the calculation of photolysis rate coefficients and not in the radiative transfer solver [Sasha Madronich, *personal communication*]. Thus, no additional error due to discrepancies between TUV versions in retrieval results is expected.

As previously discussed, TUV includes several options for solving the radiative transfer equation. However, only five methods for solving the radiative transfer equation with TUV 4.2 are specified in the OE algorithm: the Delta-Eddington method, the 4-stream discrete ordinate method, a Delta-Eddington/4-stream discrete ordinate hybrid method, the 8-stream discrete ordinate method, and

the 32-stream discrete ordinate method. Goering et al [2005] has shown that the 32-stream discrete ordinate method provides the most accurate retrieval results. However, in order to make the OE algorithm operational, radiative transfer solvers with fewer streams are favored as they take less computation time to produce retrieval results. Sensitivities studies described in Taylor [2006] indicate that that the 4-stream discrete ordinate method is the preferred choice for the radiative transfer solver as it provides reasonable results and is computationally inexpensive. Furthermore, the hybrid delta-Eddington/4-stream discrete ordinate method saves additional computational time without sacrificing the accuracy of the retrieval [*Taylor et al.*, 2008].

3.4.3 Retrieval Cloudscreening

A cloudscreening algorithm was written for the OE algorithm to provide a means to remove contaminated data from the data set prior to running the retrieval. As described in Taylor et al [2008], clouds are detected using χ^2 values calculated using the Delta-Eddington method in TUV to solve the radiative transfer equation. Data are flagged as cloudy if the χ^2 value exceeds the 98% confidence level or if the retrieval fails to converge due to the unrealistic nature of the retrieved parameters. Data that are determined to be cloud-free are passed on to the main retrieval where UV optical properties are determined.

While the cloudscreening algorithm is necessary to make the OE algorithm operational, there is a question on the accuracy of the OE algorithm's cloudscreening program. As seen in Figure 3.1, several presumed contaminated data points remain

after the data have been passed through the cloudscreening algorithm. This has also been shown in a comparison of the cloudscreened results from OE algorithm and the AERONET algorithm outlined in Smirnov et al [2000]. Taylor et al [2008] showed that the OE algorithm cloudscreening program agreed only 65.7% of the time with the AERONET cloudscreening algorithm and passed 23.2% of the retrieval scans that were flagged as cloud-contaminated by AERONET. Caution should thus be exercised when using retrieved UV optical properties from the OE algorithm as the data may still contain clouds.

3.4.4 Optimal Estimation Algorithm Settings

The OE algorithm was run for September 13th for the TexAQS II/GoMACCS campaign to compare OE-derived UV SSA and the single-wavelength-derived UV SSA. SSA values were retrieved at all UV-MFRSR wavelength channels for all UV-MFRSR data point times, however, only OE-retrieved SSA at 368nm and 332nm were used in the comparison. Location-specific TUV inputs were the same as those used in the single-wavelength method as seen in Table 3.4, however, only 50 equally-spaced layers were specified for the OE algorithm. All retrieval runs were completed using the Delta-Eddington/4-stream radiative transfer solver and assuming a 98% χ^2 threshold. A list of the default *a priori* values for SSA and AOD at all wavelengths and the wavelength-independent g are listed in Table 3.7.

Tests were performed with the OE retrieval in order to examine how user-specified parameters affect the retrieved properties. To test the effects of the choices of *a priori* SSA and g values on retrieved SSA values, the OE retrieval was run for a

few additional *a priori* values. Additionally, tests were done to remove the influence of the shorter-wavelength UV-MFRSR channels on the error and solution matrices. Because of the large errors associated with irradiance values at the lower UV-MFRSR wavelength channels and the nature of the optimal estimation technique, bad measurement data at one or more wavelengths will yield inaccurate values for SSA at 368nm and 332nm. To test this effect, the retrieval was run using large standard deviations associated with the PDFs at the shorter wavelengths in order to effectively "eliminate" the influence of the shorter wavelengths on the retrieval of SSA at 368nm and 332nm. Results from both OE sensitivity studies are reported in Chapter 4.

Table 3.1 TUV 4.4 input parameters.

Atmosphere-Specific		
Gases	*Aerosol*	*Cloud*
-NO_2 column concentrations (Dobsons) -O_3 column concentrations (Dobsons) -SO_2 column concentrations (Dobsons) -Surface pressure (mb)	-AOD -SSA -g -Angstrom exponent	-Cloud optical depth -Cloud base (km above sea level (a.s.l.)) -Cloud top (km a.s.l.)

Radiation-Specific	***Location-Specific***	***Time-Specific***
-Wavelength (nm)	-Latitude (degrees) -Longitude (degrees) -Time zone (offset from GMT) -Surface elevation (km a.s.l.) -Surface albedo	-Starting hour/SZA -Ending hour/SZA

Table 3.2 Days during TexAQS II/GoMACCS and MILAGRO that pass the cloudscreening criteria.

TexAQS II/GoMACCS		***MILAGRO***	
August	31st	*March*	12th, 13th, *17th**, 19th, *21st**
September	*3rd**, *7th**, 13th, *14th**, 19th, 20th, 25th, 26th, 27th		
October	*5th**, 6th		

*Only a fraction of the full day passed cloudscreening.

Table 3.3 Cloudscreened days from TexAQS II/GoMACCS and MILAGRO that pass the AOD criteria.

TexAQS II/GoMACCS		***MILAGRO***	
August	31st	*March*	12th, 13th, *17th**, 19th, *21st**
September	*3rd**, *7th**, 13th, *14th**		
October	*5th**, 6th		

*Only a fraction of the full day passed cloudscreening.

Table 3.4 Location-specific TUV inputs for TexAQS II/GoMACCS and MILAGRO.

	TexAQS II/GoMACCS	***MILAGRO***
Latitude (degrees)	29.71	19.70
Longitude (degrees)	-95.34	-98.99
Time zone (offset from GMT)	-6.0	-6.0
Surface elevation (km a.s.l.)	0.076	2.270
Surface albedo	0.05	0.05

Table 3.5 Summary of AERONET inversion data availability during TexAQS II/GoMACCS.

	Time(s) with Available AERONET Size Distribution (LST)	***Time(s) with Available AERONET 440nm Refractive Index (LST)***
September 3rd	7:35, 8:52	7:35, 8:52
September 13th	7:40, 15:19, 15:41, 16:10, 16:59	7:40
October 5th	8:45, 9:11	8:45, 9:11

Table 3.6 Default aerosol, trace gas, and surface pressure inputs used in the sensitivity studies.

	Default Values
SSA	0.85
AOD_{368}	0.619
AOD_{332}	0.717
g	0.70
Surface albedo	0.05
NO_2	0.358
O_3	286.3
Surface Pressure	1006.3

Table 3.7 Default *a priori* values of the OE algorithm.

	Default Values
SSA	0.85
AOD	0.80
g	0.70

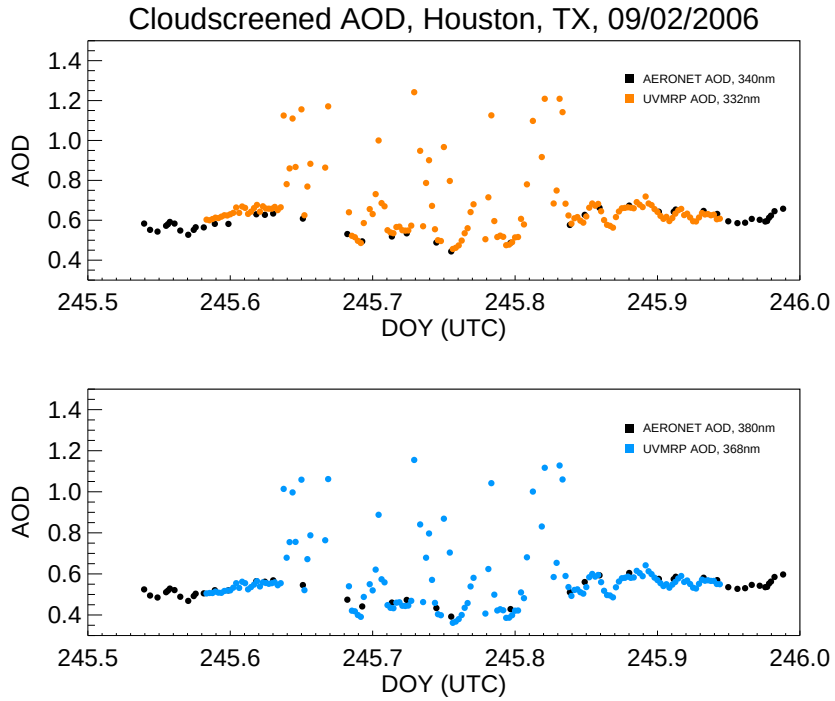

Figure 3.1 UVMRP AOD_{368} (orange) and AOD_{332} (blue) values cloudscreened using the OE algorithm cloudscreening mechanism and AERONET AOD_{380} (black, top) and AOD_{340} (black, bottom) cloudscreened during AERONET data processing.

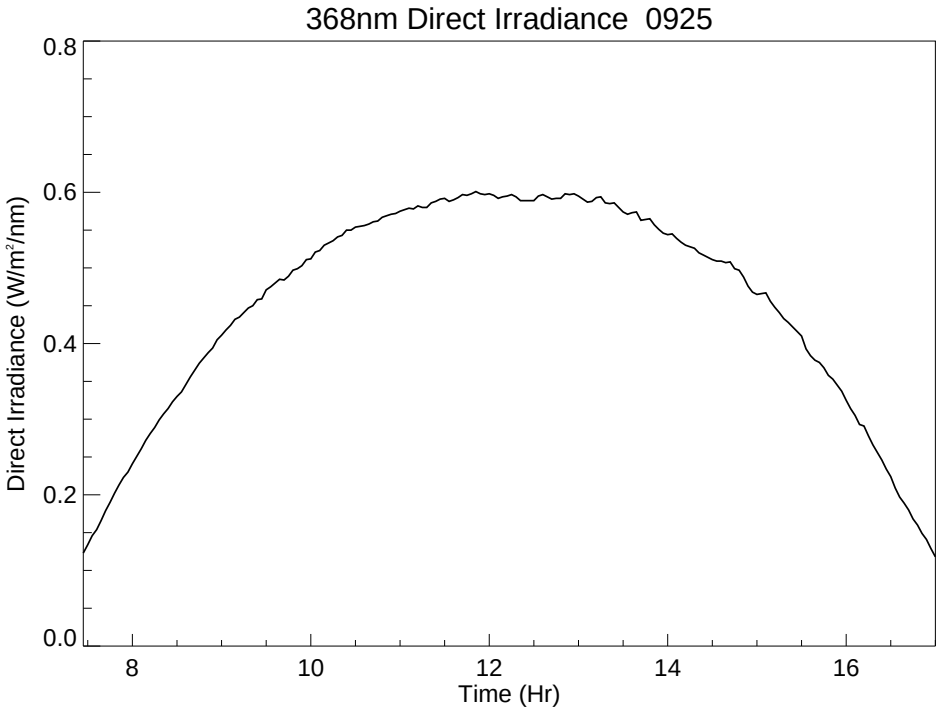

Figure 3.2 The 368nm direct irradiance profile under cloud-free conditions from September 25th.

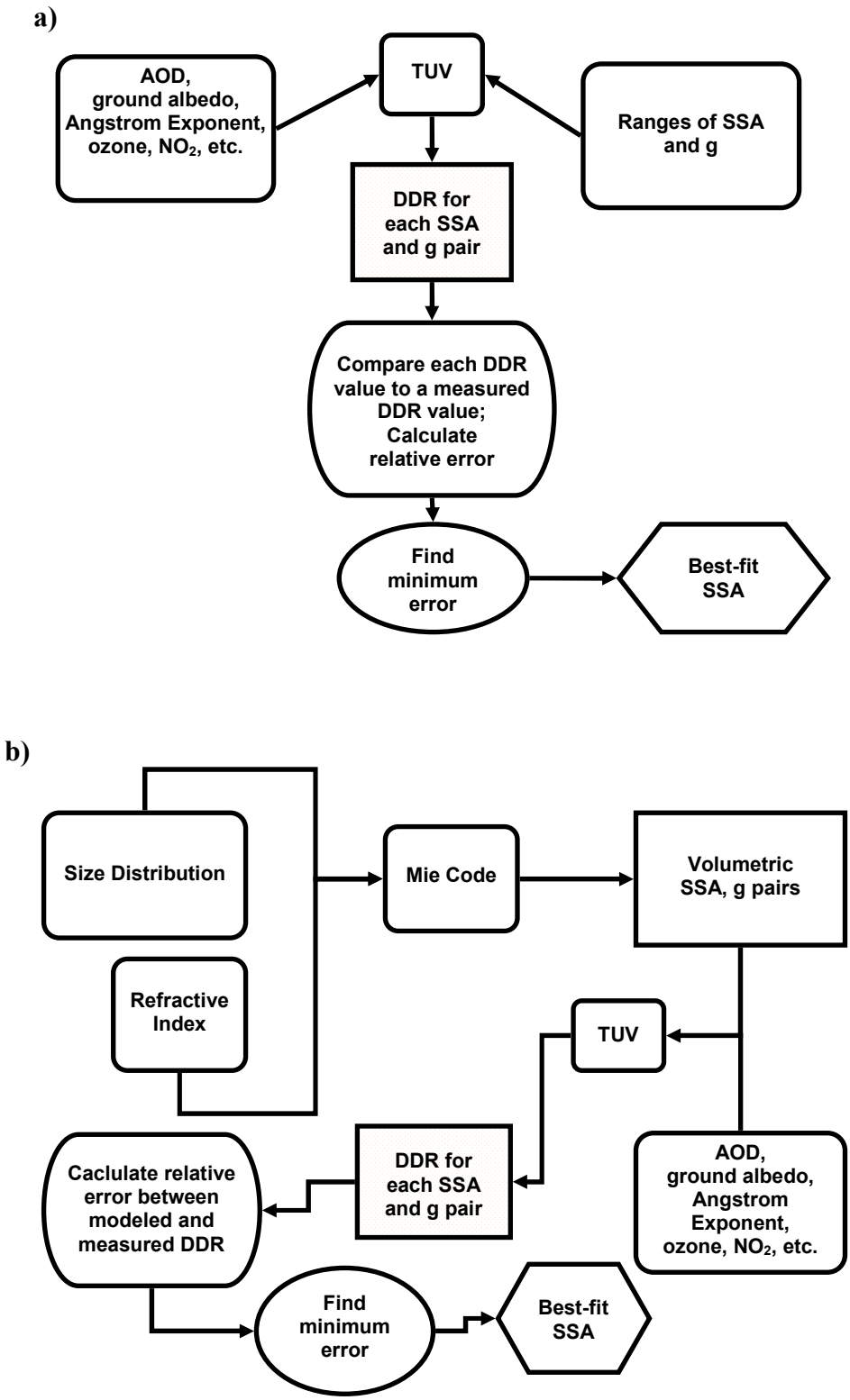

Figure 3.3 Schematics for the partial single-wavelength method (a) and the full single-wavelength method (b) used in this work.

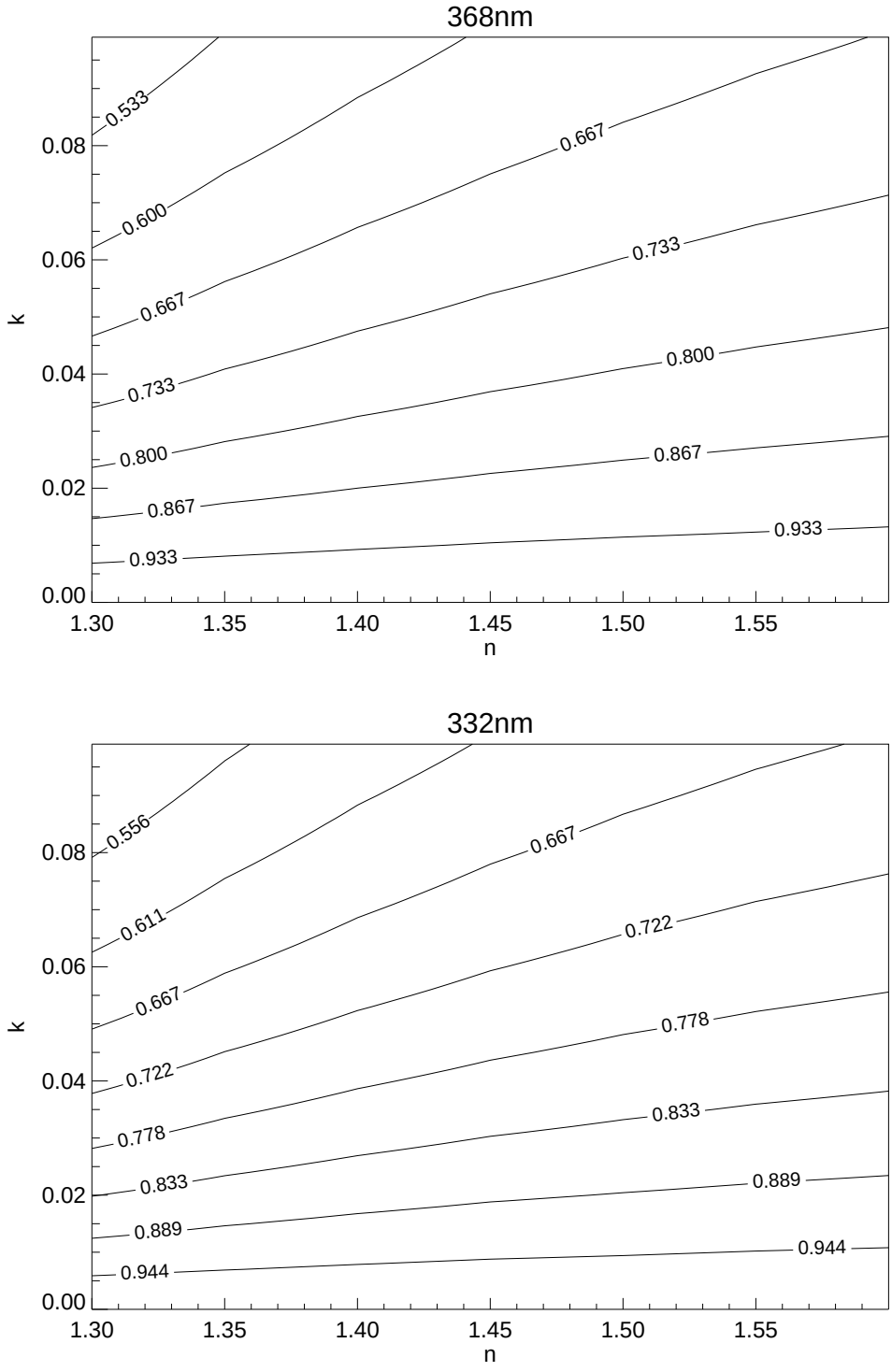

Figure 3.4 Sensitivity of SSA to the refractive index for 368nm (top) and 332nm (bottom).

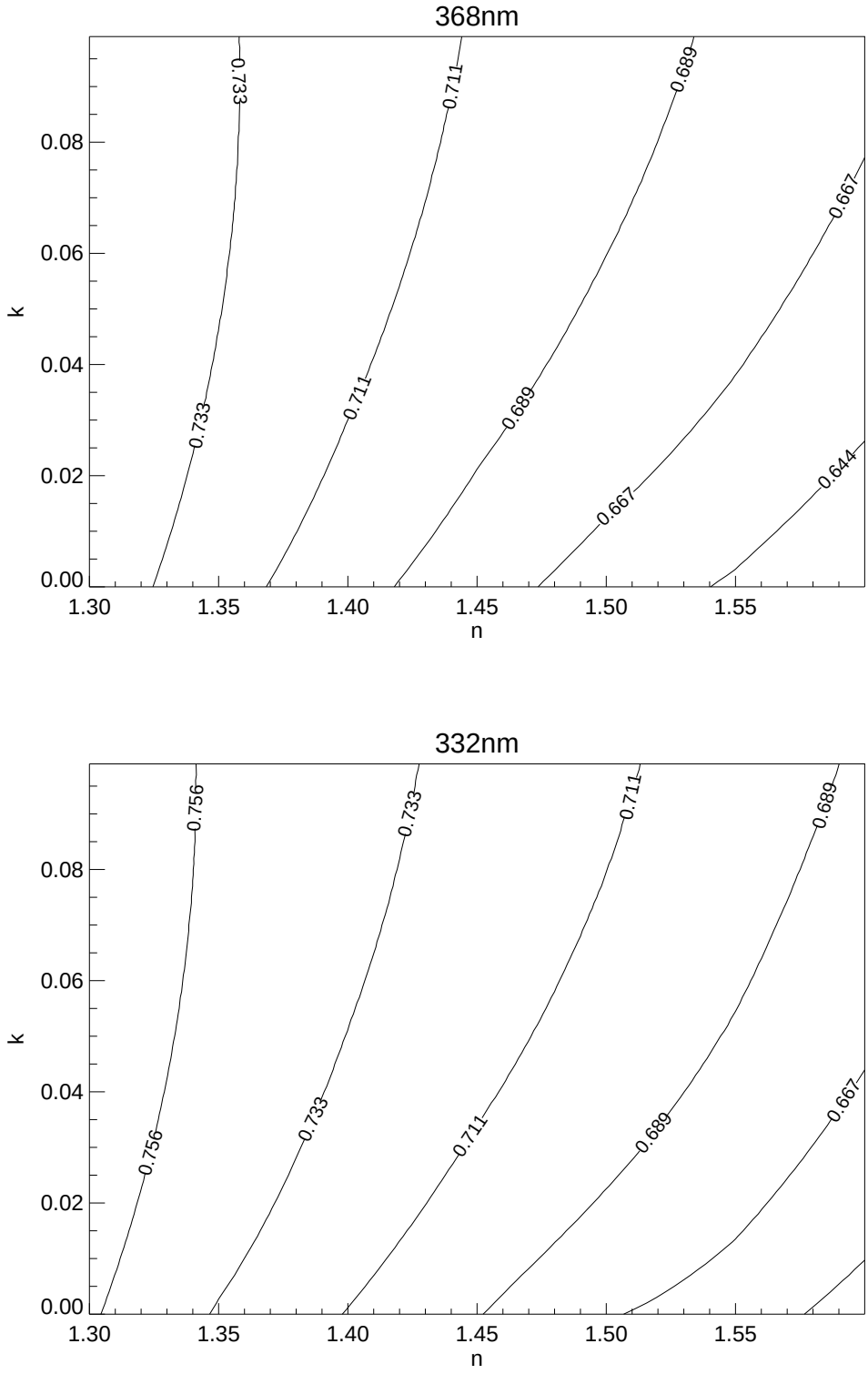

Figure 3.5 Sensitivity of g to *n* and *k* for 368nm (top) and 332nm (bottom).

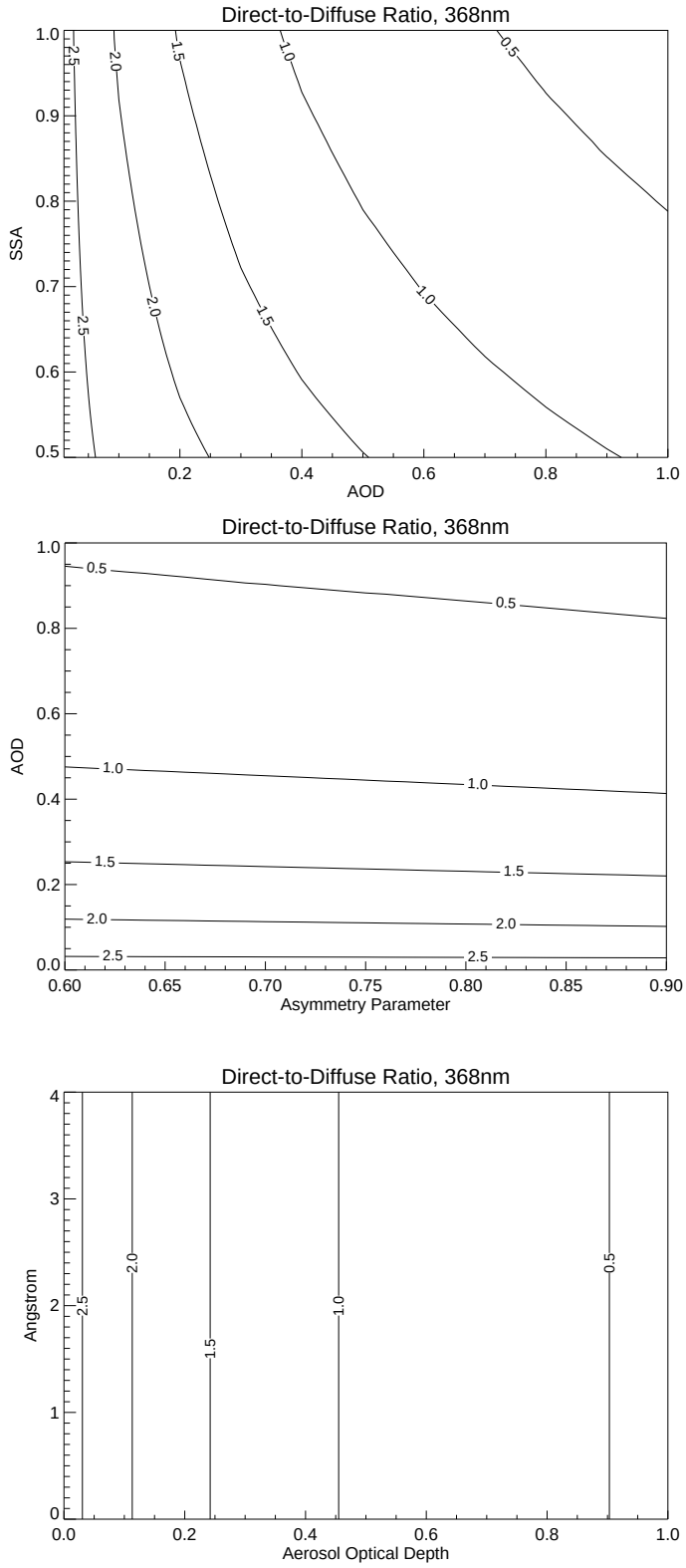

Figure 3.6 Sensitivity of the DDR to AOD and SSA (top), AOD and g (middle), and AOD and Angstrom (bottom) for 368nm.

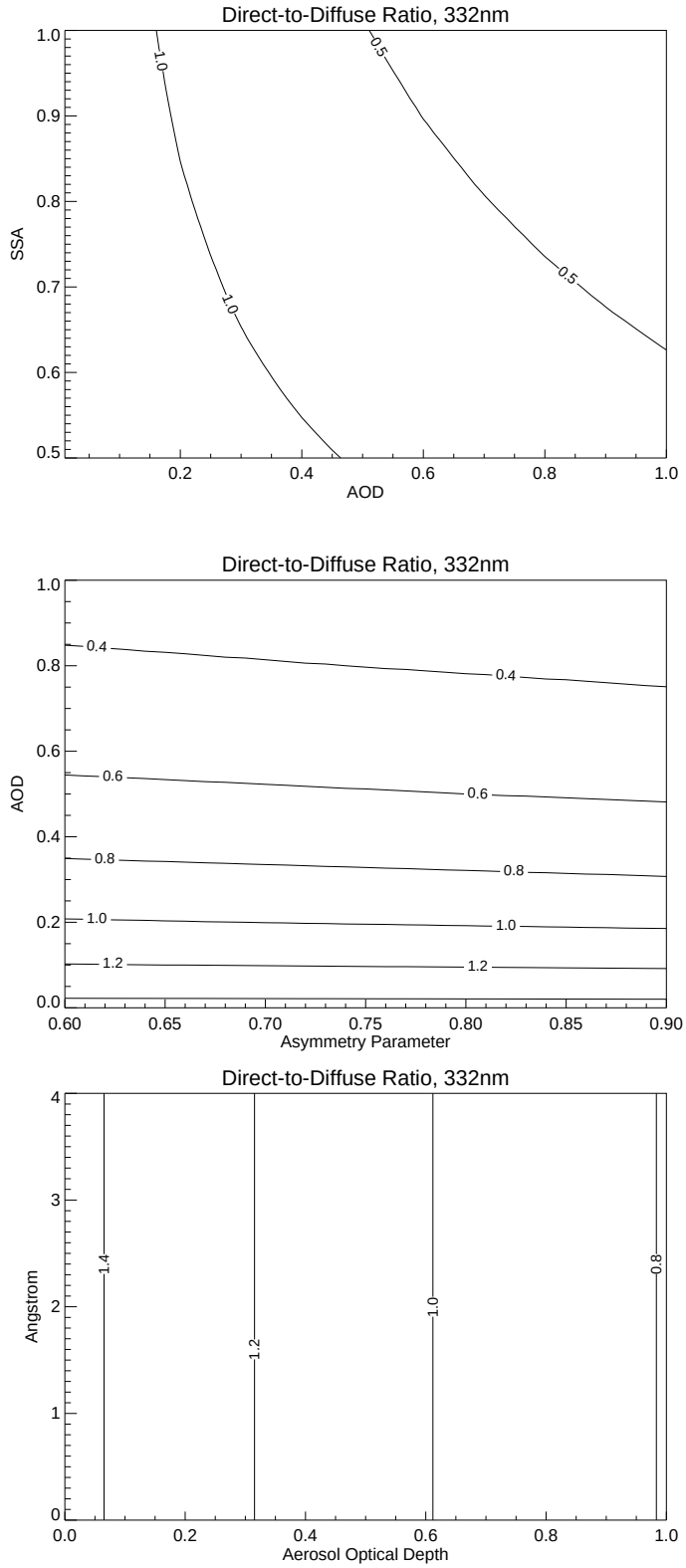

Figure 3.7 Sensitivity of the DDR to AOD and SSA (top), AOD and g (middle), and AOD and Angstrom (bottom) for 332nm.

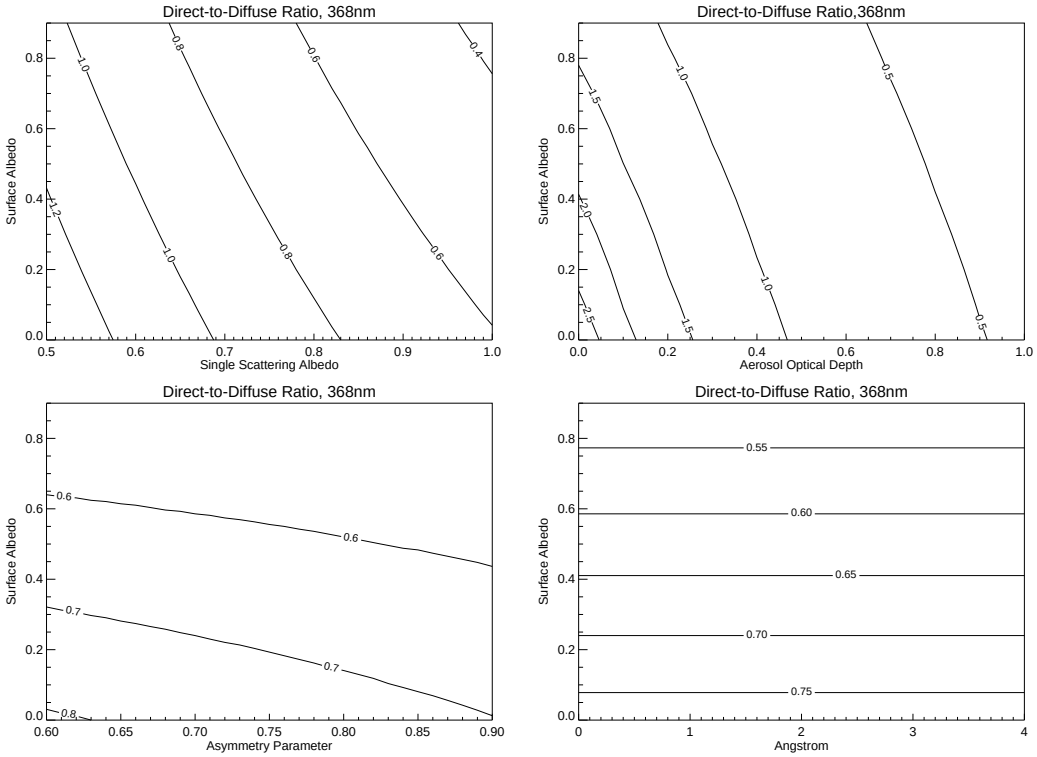

Figure 3.8 Sensitivity of the DDR to surface albedo and SSA (top left), surface albedo and AOD (top right), surface albedo and g (bottom left), and surface albedo and angstrom (bottom right) at 368nm.

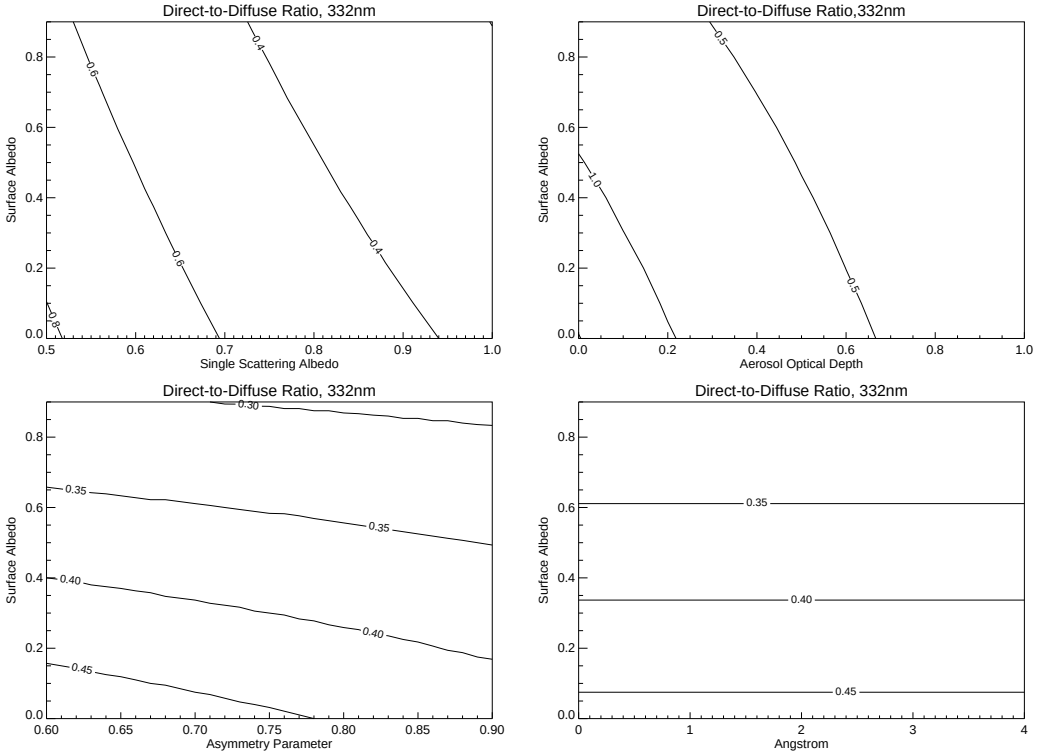

Figure 3.9 Sensitivity of the DDR to surface albedo and SSA (top left), surface albedo and AOD (top right), surface albedo and g (bottom left), and surface albedo and angstrom (bottom right) at 332nm.

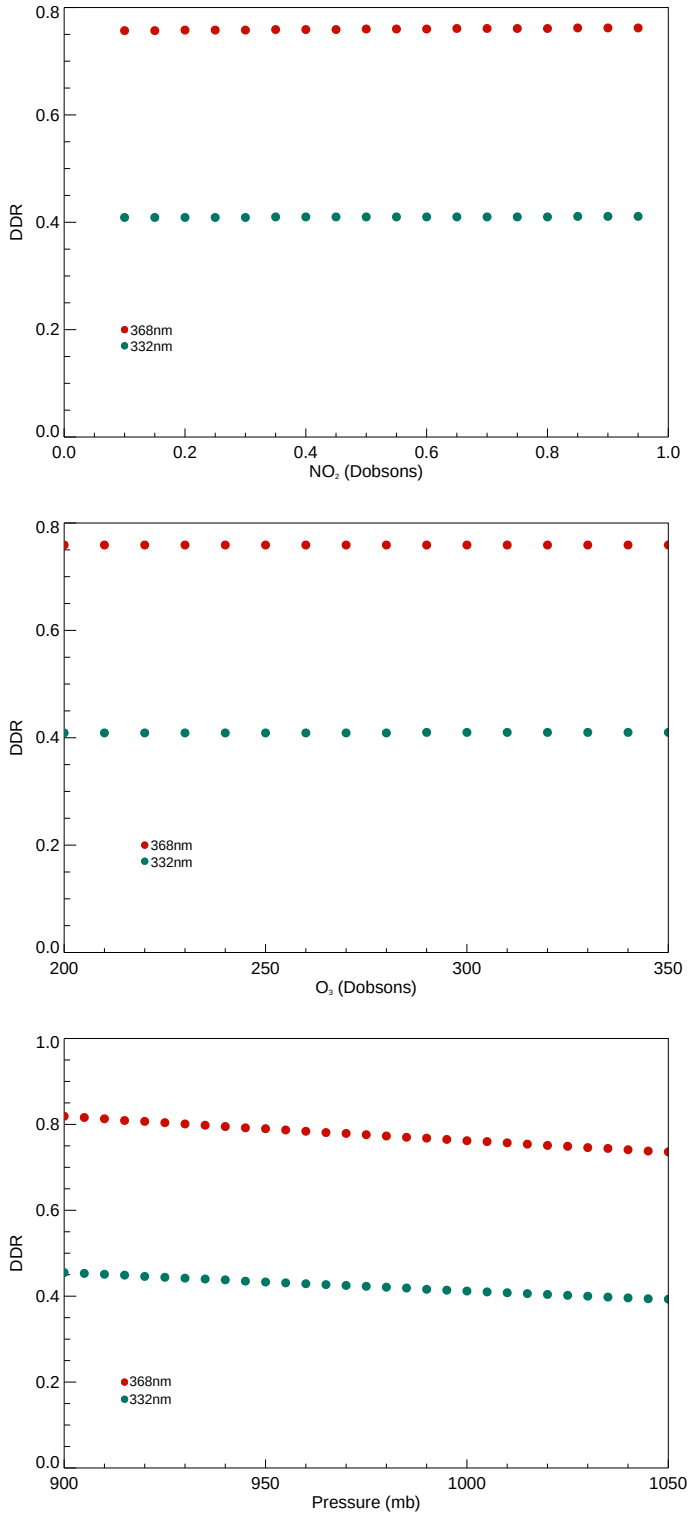

Figure 3.10 Sensitivity of the DDR to changes in NO_2 (top), O_3 (middle), and surface pressure (bottom) for 368nm (red) and 332nm (blue).

4 Retrieval Results and Discussion

Due to the previously shown relationship between SSA, g, and the DDR, values of g were not retrievable using the partial single-wavelength method as they were not constrained by additional aerosol data (e.g., size distribution, refractive index). However, the range of g values used in the analysis (0.6 to 0.9) represents an atmospherically-relevant range and yielded fairly constrained retrieved SSA values. Thus, the results for SSA only will be discussed here.

4.1 MILAGRO

The partial single-wavelength retrieval method was run for four days during the MILAGRO campaign: March 12th, March 13th, March 19th, and March 21st. These days were chosen as they met the data selection criteria discussed in Chapter 3. Ranges of SSA at 368nm (SSA_{368}) and SSA at 332nm (SSA_{332}) were retrieved following the partial single-wavelength procedure (Figure 3.3) where the retrieval reports SSA-g pairs that yielded a calculated DDR within 1% of the measured DDR. Ranges of SSA_{368} and SSA_{332} were averaged at each 1-minute time interval to yield range-averaged SSA_{368} and SSA_{332} values for the chosen range in g. It is important to note that these range-averaged SSA values do not necessarily represent the best-fit SSA.

4.1.1 Overall Campaign Results

Retrieval results for 368nm for SZA less than 65^{o} are shown in Figures 4.1 to 4.4 where the gray shaded regions represent the retrieved range of SSA_{368} and the points represent the range-averaged SSA_{368}. Daily SSA_{368} were calculated by time-averaging the range-averaged SSA_{368} values for each day and are reported in Table 4.1. The March 2006 Mexico City aerosol is dark with all of the retrieval days yielding daily SSA_{368} values below 0.72. The lowest daily SSA_{368} (0.606) was on March 19th largely due to a substantial drop in SSA_{368} over the afternoon hours. The highest value of daily SSA_{368} was found on March 12th with a value of 0.710. The maximum and minimum range-averaged SSA_{368} values were also determined for each of the analyzed MILAGRO days and are reported in Table 4.2. The study-wide maximum range-averaged SSA_{368} occurred on March 21st with a value of 0.805 while the minimum range-averaged SSA_{368} occurred on March 19th (0.518) due to the considerable dip in SSA_{368} during the afternoon hours on March 19th.

Ranges and range-averaged SSA_{332} are shown in Figures 4.5 to 4.8 and daily SSA_{332} values are reported in Table 4.1. Similar to the daily SSA_{368} values, the minimum daily SSA_{332} (0.500) is found on March 19th. It should be noted that this minimum value is the lowest SSA value considered in the retrieval and thus this minimum value may be a function of retrieval resolution and may not represent a true minimum. As was the case with SSA_{368}, the maximum daily SSA_{332} was found on March 12th at 0.699. Daily maximum and minimum average SSA_{332} were determined for each day and are listed in Table 4.2. Similar to SSA_{368}, the maximum range-

averaged SSA_{332} occurred on March 21st while the minimum range-averaged SSA_{332} occur on March 19th due to a large drop in SSA in the afternoon hours

4.1.2 Daily Results

A two-tailed Student's t-test was used to examine the statistical significance of the difference between range-averaged SSA_{368} and range-averaged SSA_{332} at each time interval using the equation

$$t = \frac{\bar{x}_1 - \bar{x}_2}{\sigma\sqrt{\frac{1}{N_1} + \frac{1}{N_2}}} \tag{4.1}$$

where

$$\sigma = \sqrt{\frac{N_1 s_1^{\,2} + N_2 s_2^{\,2}}{\nu}} \tag{4.2}$$

N_1 is the number of SSA_{368} values for a given time interval, N_2 is the number of SSA_{332} values for a given time interval, s_1 is the standard deviation of the SSA_{368} values per time interval, s_2 is the standard deviation for averaged SSA_{332} values per time interval, $\bar{x}_1$ is the range-averaged SSA_{368} for a given time interval, and $\bar{x}_2$ is the range-averaged SSA_{332} for the same time interval. The parameter ν represents the degrees of freedom and is expressed by the equation

$$\nu = N_1 + N_2 - 2 \tag{4.3}$$

The degrees of freedom values were used to compute a critical t-value (t_{crit}) at the 95% confidence level for each time interval. The range-averaged SSA_{368} was

considered statistically different from the range-averaged SSA_{332} if the t-value calculated for the time interval of interest (Equation 4.1) exceeded the t_{crit} value.

March 12th

SSA_{368} and SSA_{332} ranges were retrieved for the entire day (838 to 1653 CST) on March 12th. As seen in Figure 4.9, SSA_{368} and SSA_{332} track each other fairly well; both SSA ranges start at low values in the morning hours (~0.700 for both range-averaged SSA_{332} and range-averaged SSA_{368}), remain fairly stable through the late morning and early afternoon hours, and then gradually increase to the highest range-averaged value in the late afternoon (0.752 and 0.743 for range-averaged SSA_{368} and range-averaged SSA_{332}, respectively). Both SSA ranges also show some high frequency variability in the early afternoon. While this variability may represent aerosol, it may also indicate the presence of clouds. As seen in Figure 4.10, there is some high frequency variability in the 368nm direct irradiance profile, likely indicating the presence of a broken cumulus or cirrus cloud field. However, as seen in Figure 4.11, UVMRP AOD values remain fairly low and have little scatter over the course of the day, indicating there is likely no significant influence on the aerosol optical properties from clouds on March 12th. Such a finding emphasizes the need for an accurate, mathematical cloudscreening program.

Daily SSA_{368} and SSA_{332} were calculated as 0.710 and 0.699, respectively. As seen in Figure 4.9, the ranges of SSA_{332} and SSA_{368} overlap for much of the day. Between approximately 1000 and 1600 CST, the SSA_{332} range extends slightly lower than the SSA_{368} range, suggesting the presence of an aerosol that absorbs more strongly at shorter wavelengths at these hours. According to statistical analysis,

range-averaged SSA_{368} is significantly higher than range-averaged SSA_{332} for 60.9% of the day on March 12th. These significant differences occur at time intervals primarily between 1000 and 1600 CST, the same period in which the range of SSA_{332} is lower than the range of SSA_{368} (Figure 4.9).

March 13th

The trends in the partial single-wavelength retrieval results for March 13th are similar to those seen on March 12th (Figure 4.12). Ranges of both SSA_{368} and SSA_{332} start fairly low and rise to maximum range-averaged values in the late afternoon (0.773 and 0.771 for range-averaged SSA_{368} and range-averaged SSA_{332}, respectively). There is also substantial high frequency variability in both of the SSA ranges from the late morning through the early afternoon (approximately 1100 to 1400 CST). As seen in Figures 4.13 and 4.14, both the direct irradiance profile and the AOD values also show high frequency variability over the same three hour period as the SSA values. Thus, while it is hypothesized that this variability is due to the presence of a broken cloud field, changes in SSA due to rapid fluctuations in AOD cannot be ruled out.

The daily SSA_{368} and SSA_{332} were fairly low with values of 0.649 and 0.638, respectively. Similar to March 12th, the range in SSA_{368} is higher than the range in SSA_{332} from the late morning through the afternoon, indicating the presence of an aerosol that absorbs more strongly at shorter wavelengths. This trend is observed in the statistical analysis of the difference in range-averaged SSA values at each time interval. Range-averaged SSA_{368} was found to be significantly higher than SSA_{332}

for 65.0% of the time intervals on March 13th with significant differences largely found between the hours of 1000 and 1600 CST.

March 19th

Retrieved ranges of SSA_{368} and SSA_{332} for March 19th are shown in Figure 4.3 and 4.7, respectively. Perhaps most striking is the substantial dip in both SSA_{368} and SSA_{332} beginning approximately at 1000 CST and lasting through the afternoon. Prior to the dip, both SSA_{368} and SSA_{332} start out at the highest range-averaged values (0.728 and 0.702 for range-averaged SSA_{368} and range-averaged SSA_{332}, respectively). Between approximately 1300 and 1400 CST, values of both SSA_{368} and SSA_{332} fall to the lowest values of the day, remaining around 0.53 and 0.500 for range-averaged SSA_{368} and range-averaged SSA_{332} respectively. It is also at this time that the campaign minimum values of 0.518 and 0.500 for 368nm and 332nm are reached. In examining the AOD_{368} and AOD_{332} values for March 19th, a notable increase in both AOD values is seen over the same period as SSA decrease (Figure 4.15). Similarly, the direct irradiance at each wavelength decreases fairly rapidly beginning at approximately 1000 CST as shown in Figure 4.16. Clear skies were reported for the entire day on March 19th [*Fast et al.*, 2007]and thus it therefore unlikely such changes in the irradiance profile and AOD are driven by clouds, but rather indicate the presence of a UV-absorbing aerosol.

As stated previously, the lowest daily SSA values for the campaign were determined for March 19th, with values of 0.606 and 0.557 for daily SSA_{368} and daily SSA_{332}, respectively. While these daily SSA values appear to be fairly close, there is a substantial difference in retrieved SSA_{368} and SSA_{332} ranges; the range in SSA_{332} is

almost entirely below the range in SSA_{368} for a majority of the retrieval time period (Figure 4.17). The noteable exception is between the hours of 1300 and 1400 CST when both SSA_{368} and SSA_{332} fall to minimum values. Statistical analysis of the difference in range-averaged SSA_{368} and range-averaged SSA_{332} for each time interval on March 19th indicated that range-averaged SSA_{368} is significantly higher than range-averaged SSA_{332} for 93.3% of the retrieval time intervals.

March 21st

Ranges of SSA_{368} and SSA_{332} were only retrieved between 830 and 1400 CST on March 21st CST due to late afternoon cloud cover (Figure 4.18). There is little to no high frequency variability in either of the average SSA trends, however, the overall trends in SSA_{368} and SSA_{332} are not the same. The range-averaged SSA_{368} values are fairly constant, remaining around 0.7, while range-averaged SSA_{332} has more variability over the retrieval time period. These different trends yield a notable offset between SSA_{368} and SSA_{332} (Figure 4.18). Similar to March 19th, the range in SSA_{332} lies below the range in SSA_{368} for nearly the entire March 21st retrieval period. This is reflected in the statistical analysis of the difference between range-averaged SSA values which indicated range-averaged SSA_{368} is significantly different from range-averaged SSA_{332} for all time intervals.

4.1.3 Discussion of Daily Results

A meteorological synopsis for each day of MILAGRO was reported in Fast et al [2007]. The campaign was characterized by three meteorological regimes based on relative humidity, cloud cover, and temperature. Regime 1 extended from March 7th

to March 14th and was characterized by hot, dry conditions with minimal cloud cover. March 14th to March 23rd defined regime 2 during which more humid conditions existed and afternoon convective activity was more persistent. Regime 3 was identified as the period between March 23rd and 29th and was characterized by increases in afternoon convection and cloud cover as well as precipitation.

Both March 12th and 13th had generally low humidity (<~30%) and high temperatures (~30°C) as was characteristic for days within regime 1. However, skies were not cloud free for either day, with cirrus clouds reported on March 12th and isolated deep convection in the afternoon of March 13th. These reports support the suggested relationships between SSA and direct irradiance for both days. Surface flow was out of the South-Southwest for both days indicating transport from Mexico City's urban center was probable for both March 12th and 13th. Fairly low wind speeds (6-10 m/s) persisting for both days.

This hypothesis is supported by the aerosol chemistry data collected for the MILAGRO and presented in Doran et al [2007] and shown in Figure 4.19. Organic carbon (OC) and elemental carbon (EC) are moderately high for March 12th (day of year (DOY) 71). Both species spike in the morning, with values of approximately 16 $\mu gC/m^3$ and 4 $\mu gC/m^3$ for OC and EC, respectively, concentrations are representative of an urban plume. Through the afternoon hours on the 12th, OC and EC concentrations decrease, with OC dropping to approximately 5 $\mu gC/m^3$ and EC to 0.5 $\mu gC/m^3$. Recalling results presented in Bergstrom et al [2007], SSA of urban aerosol exhibits spectral absorption trends such that SSA is lower at longer wavelengths than

at shorter wavelengths. This signal is largely explained by the previously discussed behavior of SSA with respect to wavelength and particle size such that

$$SSA = 1 - \left(\frac{b_{abs,0}}{b_{ext,0}}\right)\left(\frac{\lambda}{\lambda_o}\right)^{-1+\alpha} \qquad 4.4$$

where α is the angstrom exponent [*Bergstrom et al.*, 2002]. If the aerosol is dominated by smaller particles (i.e., freshly emitted aerosol), such as those associated with an urban plume, α would be greater than 1 and thus, SSA should decrease with an increase in wavelength. However, such a trend was not observed for March 12th, rather, SSA decreased with a decrease in wavelength.

To understand why such a trend may be observed, the composition of the aerosol must be considered in addition to aerosol size. Several studies have noted carbonaceous aerosol species to have a strong spectrally dependent absorption characteristics [*Bond*, 2001; *Kirchstetter et al.*, 2004]. As a result, these organic aerosol species have larger absorption Angstrom exponents than are predicted by size alone. Recalling the relationship between SSA, absorption Angstrom, and scattering Angstrom discussed in Chapter 1, an increase in the absorption Angstrom could potentially remove or even reverse the predicted increase in SSA with decrease in wavelength. It is likely that OC measured on March 12th may include organics that preferentially absorb at shorter wavelengths due to the presence of biomass burning activity near the measurement site on March 12th [Sasha Madronich, *personal communication*]. The highest absorption Angstrom exponents have been determined from OC aerosol collected from biomass burning events [*Bond*, 2001; *Kirchstetter et*

al., 2004], supporting the notion that OC with spectral absorption characteristic is present at the measurement site on March 12th.

While a similar relationship between SSA_{368} and SSA_{332} was shown for March 13th, aerosol chemical data are unavailable for much of the 13th (DOY 72) [*Doran et al.*, 2007]. However, data collected in the morning of the 13th indicate spikes in both OC and EC. Morning OC concentrations were lower for the 13th than the 12th, with concentrations of approximately 11 $\mu gC/m^3$. A substantial spike in EC much larger than what was seen on March 12th was observed on the morning of March 13th. EC concentrations reached 7.5 $\mu gC/m^3$ for the 13th, the largest for the entire campaign [*Doran et al.*, 2007].

While the relationship between SSA and particle size (Equation 4.6) would suggest an increase in SSA with a decrease in wavelength, the opposite is observed. This may also be explained by the presence of an organic species with spectral absorption characteristics. Similar to March 12th, a biomass burning event was reported on March 13th [Sasha Madronich, *personal communiciation*]. Based on the previously discussed characteristics of biomass burning OC, it is likely carbonaceous aerosol with spectrally absorption characteristics is present at the T1 site on March 13th.

Characteristic of the regime 2 meteorology, slight increases in humidity were observed on March 19th and 21st with relative humidity values of approximately 60% and 40% for the 19th and 20th, respectively [*Fast et al.*, 2007]. Temperatures for both days were lower than those observed on March 12th and 13th (~25°C for both the 19th and 21st) [*Fast et al.*, 2007]. Though there was an increase in the frequency of deep

convection regime 2 days compared to regime 1, clear skies were reported for the morning hours of both March 19th and 21st [*Fast et al.*, 2007]. Clear skies were also observed during the afternoon hours of the 19th, however partly cloudy conditions were reported for the afternoon of the 21st [*Fast et al.*, 2007]. As discussed earlier, these clouds were seen in the direct irradiance profile and thus the retrieval was not run after 1400 CST on March 21st. Surface and upper-level flow was out of the South-Southwest for both March 19th and 21st, however, surface wind speeds were quite different between March 19th and 21st. Winds were sustained at moderate speeds (~10 m/s) for the entire day of the 19th while winds were generally calm (less than 5 m/s) for the 21st.

While the upper-level and surface flow conditions were favorable for transport from Mexico City on both March 19th and March 21st, the trends in SSA for both days are not consistent with what is expected in the presence of fresh emissions. As were the cases for March 12th and 13th, SSA appears to decrease rather than increase with a decrease wavelength as would be expected if small particles were present. Concentrations of OC (average concentration of ~6 $\mu gC/m^3$) and EC (average concentration of ~1 $\mu gC/m^3$) are lower on the 19th than on the 12th and 13th, suggesting fewer small particles at the measurement site. Additionally, as shown in Figure 4.15, AOD_{368} and AOD_{332} appear to get closer, indicating an increase in the Angstrom exponent in the afternoon hours. Examining Equation 4.6, an angstrom exponent around 1 would yield spectrally independent SSA values, such as those seen for the 19th.

This is consistent with findings of Querol et al [2008] who report large campaign mean concentrations of coarse mode material (PM_{10}) at the measurement site suggesting elevated concentrations of dust at the T1 measurement site compared to surrounding areas. Increases in dust concentrations were attributed to dust resuspension events during times of moderate to high wind speeds at the measurement site due to the site's proximity to a cement plant and limestone quarry [*Querol et al.*, 2008]. With wind speeds sustained at 10 m/s over the course of the day, it is likely local dust was present on March 19th. Additionally, mineral dust has been shown to strongly absorb in the UV [*Derimian et al.*, 2007] thus explaining the substantial drop in SSA_{368} and SSA_{332} over the late morning and afternoon hours of March 19th.

Retrieval results for March 21st indicated that range-averaged SSA_{368} values were significantly higher than range-averaged SSA_{332} for the entire retrieval period. While, such a spectral signal is likely to be driven by an aerosol species with short-wavelength preferential absorption characteristics, available aerosol chemistry data suggests such species are not present at the T1 measurement site. Similar to March 19th, March 21st concentrations of OC and EC were fairly low, with approximate average values of 7 $\mu gC/m^3$ and 2 $\mu gC/m^3$ for OC and EC, respectively [*Doran et al.*, 2007], possibly suggesting small particles did not dominate the aerosol type on the 21st. However, unlike March 19th, wind speeds for the 21st were low and therefore it is unlikely the T1 measurement site is influenced by local dust. Concentrations of inorganic aerosol species (e.g., ammonium sulfate, ammonium nitrate, seasalt) at T1

are needed to make further conclusions regarding the aerosol type responsible for such a trend in SSA values.

4.2 TexAQS II/GoMACCS

4.2.1 Overall Campaign Results

The partial single-wavelength retrieval was used to retrieve a range of SSAs for a chosen range in g for seven days during the TexAQS II/GoMACCS campaign that passed the previously discussed data quality criteria: August 31st, September 3rd, September 7th, September 13th, September 14th, October 5th, and October 6th.

Partial single-wavelength results for TexAQS II/GoMACCS are shown in Figures 4.20 to 4.26 where the gray shaded region represents the range of retrieved SSA_{368} values and the points represent the range-averaged SSA_{368}. The range-averaged SSA_{368} values were subsequently time-averaged to yield daily SSA_{368}. Daily SSA values indicate that the Houston aerosol is generally fairly bright with daily SSA_{368} values above 0.9 for five out of seven of the days (Table 4.3). The lowest daily average SSA (0.816) occurred on August 31st. September 3rd had the highest daily SSA_{368} with a value of 0.969. The maximum and minimum range-averaged SSA_{368} values for each partial retrieval day are reported in Table 4.4. The minimum and maximum average TexAQS II/GoMACCS campaign were seen on August 31st (SSA_{368} = 0.738) and September 3rd (SSA_{i368} = 1.00), respectively.

Retrieved SSA_{332} values are shown in Figure 4.27 to 4.33 where the gray shaded region represents the range of SSA_{332} values and the points represent the range-averaged SSA_{332}. The range-averaged SSA_{332} values were time-averaged to

yield a daily SSA_{332} for each partial retrieval day. Daily SSA_{332} values show a similar trend to the daily SSA_{368} as is seen in Table 4.3; daily SSA_{332} is minimum on August 31st with a value of 0.802 while daily SSA_{332} is highest on September 3rd with a value of 0.936. It is important to note that all daily SSA_{332} values are lower than SSA_{368} indicating possible spectral dependence of SSA during the entire TexAQS II/GoMACCS campaign.

4.2.2 Daily Results

As was done for the MILAGRO retrieval days, statistical analysis was performed using the Student's t-test (Equation 4.1) to determine if range-averaged SSA_{368} was significantly different from range-averaged SSA_{332} at each time interval.

August 31st

As mentioned previously, the lowest daily and averaged SSA values for both wavelengths were found on August 31st. This is largely attributed to the dip in retrieved SSA values between the hours of 800 and 1100 CST observed at both 368nm and 332nm (Figures 4.20 and 4.27, respectively). An increase in AOD_{368} and AOD_{332} values was also observed over the 3-hour morning period (Figure 4.34). To examine the relationships between the retrieved range-averaged SSA_{368} and AOD_{368} and range-averaged SSA_{332} and AOD_{332}, correlation coefficients between AOD and SSA at each wavelength were calculated using regression analysis. AOD and SSA are inversely correlated for both wavelengths, with correlation coefficients of -0.514 and -0.239 for 368nm and 332nm, respectively. The statistical significance of these

correlation coefficients was tested using a two-tailed Student's t-test for correlation coefficients

$$t = r\frac{\sqrt{N-2}}{\sqrt{1-r^2}} \qquad 4.5$$

where r is the correlation coefficient and N is the sample size. For the morning period, the correlation between AOD_{368} and SSA_{368} is statistically significant. However, the correlation between AOD_{332} and SSA_{332} for the same period is not statistically significant.

An additional increase in AOD_{368} and AOD_{332} values occurs later in the day on August 31st (4.34). Regression analysis was again performed to determine the correlation coefficients between AOD_{368} and range-averaged SSA_{368} and between AOD_{332} and range-averaged SSA_{332} for the afternoon hours of interest (1200 to 1645 CST). The analysis yielded correlation coefficients of -0.146 and +0.321 for 368nm and 332nm, respectively. Testing with the Student's t-test indicated that the correlation at 368nm was not significant while the correlation at 332nm was. The different relationship between AOD and SSA at both wavelengths between the morning hours and afternoon hours possibly indicates aerosol composition and/or size changed midday.

The Student's t-test was performed to test the statistical significance in the difference between the range-averaged SSA_{368} and the range-averaged SSA_{332} at each time interval. As seen in Figure 4.35, the range of SSA_{332} extends to higher values than the range of SSA_{368} during the morning hours (800 to 1000 CST). This trend reverses during the late morning hours and extends into the afternoon (~1000 to 1600

CST). Statistical analysis indicates that the observed trend in SSA in the morning hours is not significant, while the difference in range-averaged SSA_{368} and SSA_{332} for the afternoon hours is. As a result, 63.6% of August 31st has significantly different range-averaged SSA_{368} and SSA_{332} values.

September 3rd

Ranges of SSA_{368} and SSA_{332} were only retrieved for the morning hours (803 to 1200 CST) of September 3rd due to the presence of afternoon clouds. Daily SSA_{368} and SSA_{332} are therefore an average of these morning hours only. The daily SSA_{368} and SSA_{332} for September 3rd were the highest for the whole campaign (0.969 and 0.936, respectively) indicating the presence of a UV-scattering aerosol for the morning hours of this day. Range-averaged SSA_{368} and SSA_{332} remain high throughout this period with the range of SSA_{368} and SSA_{332} values remaining above 0.9 (Figure 4.36). SSA_{368} and SSA_{332} values also remain fairly constant throughout the morning hours. This stable trend in SSA_{368} and SSA_{332} is reflected in the fairly constant UVMRP AOD_{368} and AOD_{332} as seen in Figure 4.37.

There is a notable difference between the ranges of SSA_{368} and SSA_{332} values with the range of SSA_{332} generally lower than the range of SSA_{368} throughout the morning hours (Figure 4.37). Statistical analysis indicated that the range-averaged SSA_{368} was significantly higher than the range-averaged SSA_{332} for nearly the entire day of September 3rd (93.8%).

September 7th

Due to afternoon cloud contamination, ranges of SSA_{368} and SSA_{332} values were only obtained for 803 to 1200 CST on September 7th. As shown in Figure 4.38,

there is considerably more variation in both SSA_{368} and SSA_{332} over the morning hours than there was on September 3rd. Both SSA_{368} and SSA_{332} gradually decrease over the 4 hour time period with additional short duration dips in SSA seen around 830 and 945 CST for both wavelengths. The range in SSA_{332} extends to lower values than the range in SSA_{368} for much of the day (Figure 4.38). This is reflected in the statistical analysis of the difference between range-averaged SSA_{368} and range-averaged SSA_{332} which indicated range-average SSA_{368} was significantly higher than range-averaged SSA_{332} for 81.3% of September 7th.

September 13th

Ranges of SSA_{368} and SSA_{332} were determined for the entire day of September 13th (806 to 430 CST). Calculated daily SSA_{368} and SSA_{332} were fairly high, with values at 0.962 and 0.924 for SSA_{368} and SSA_{332}, respectively. Examining the range-averaged SSA_{368} and SSA_{332} values in Figures 4.23 and 4.30, the trends in SSA_{368} and SSA_{332} are fairly different over the 8 ½ hour period. Average SSA_{368} appears to be fairly constant through the early afternoon with increased variability after approximately 1400 CST. However, SSA_{332} gradually decreases throughout the entire day.

The difference between the ranges of SSA is substantially more pronounced on September 13th than the other six TexAQS II/GoMACCS retrieval days. As seen in Figure 4.39, the range in SSA_{332} extends to lower values for the entire day on September 13th. Statistical analysis indicated that range-averaged SSA_{368} was significantly higher than range-averaged SSA_{368} at all time intervals for September 13th.

September 14th

SSA_{368} and SSA_{332} were only retrieved for the morning hours of September 14th (809 to 1200 CST) due to the presence of afternoon clouds. As seen in Figure 4.40 both ranges of SSA_{368} and SSA_{332} values decrease in the morning through approximately 1030 CST and then subsequently increase between 1030 and 1200 CST. This increase is reflected in the UVMRP AOD values (Figure 4.41).

The range of SSA_{332} extends to lower values than the range in SSA_{368} for much of the day with the except for approximately one hour in the late morning (1030 to 1130 CST) where the range in SSA_{332} and the range in SSA_{368} appear to overlap. Range-averaged SSA_{368} is significantly higher than range-averaged SSA_{332} for 87.2% of the day as indicated by statistical analysis.

October 5th

Values of SSA_{368} and SSA_{332} retrieved for the morning hours of October 5th (821 to 1200 CST) show little variation over the retrieval time period. The minimal change in the SSA_{368} and SSA_{332} ranges is reflected in the fairly constant average SSA_{368} and SSA_{332} values (Figures 4.25 and 4.32). The average SSA values are also generally high, with values remaining above 0.9 for both wavelengths yielding higher daily SSA_{368} and SSA_{332} values of 0.946 and 0.926, respectively.

As seen in Figure 4.42, there is only a slight difference in the retrieved range of SSA_{368} and the retrieved range of SSA_{332}. This difference persists over the retrieval time period with the range in SSA_{332} extending to lower values than the range in SSA_{368}. This is reflected in the statistical analysis of the difference in range-averaged SSA_{368} and range-averaged SSA_{332} which indicated range-averaged SSA_{368}

was significantly higher than range-averaged SSA_{332} for 100% of the time intervals on October 5th.

October 6th

Ranges of SSA_{368} and SSA_{332} were only retrieved for the morning and early afternoon hours of October 6th (824 to 1400 CST) due to late afternoon cloud contamination (Figures 4.26 and 4.33). Similar to October 5th, the ranges of both SSA_{368} and SSA_{368} were fairly constant throughout the retrieval period. Additionally, the ranges of both SSA_{368} and SSA_{332} were fairly high with respect to the rest of the retrieval days as reflected in the daily SSA_{368} and SSA_{332} (0.935 and 0.908, respectively).

Over the retrieval time period the range of SSA_{332} is consistently lower than the range of SSA_{368} (Figure 4.43). As was the case for October 5th, statistical analysis indicated range-averaged SSA_{368} was significantly higher than range-averaged SSA_{332} for all retrieval time intervals for October 6th.

4.2.3 Discussion of Daily Results

Aerosol chemistry and meteorological data obtained during the TexAQS II/GoMACCS campaign has not been made available at the present time. However, some conclusions regarding the retrieval results from Houston may be inferred from the relationship between wavelength and SSA described in Equation 4.6. All five of the retrieval days that had significantly different daily SSA_{368} and SSA_{332} values had similar trends, with higher values of SSA_{368} than SSA_{332}. Such a trend is possible with a slightly negative Angstrom exponent, as is possible with large particles.

Because of Houston's proximity to the Gulf of Mexico, it is likely the area is influenced by large seasalt particles. Such particles potentially yield a slightly negative Angstrom exponent and thus may be responsible for the observed trends in SSA. Wind speed, wind direction, and inorganic aerosol concentration datasets are needed to examine this possibility. Another possibility is that these trends may reflect the presence of small, but strongly UV-absorbing, aerosols, such as nitrated aromatics [*Jacobson*, 1999] or the presence of an unaccounted for absorbing gas species, such as SO_2. Aerosol and gas chemical data would be useful in determining if a preferentially-absorbing material was in fact present.

4.3 Retrieval Comparison

4.3.1 Full Single-Wavelength Retrieval Comparison

Full single-wavelength retrievals were performed following the procedure depicted in Figure 3.3 for the morning hours of September 13th (724 to 939 CST) during the TexAQS II/GoMACCS campaign to validate the robustness of retrieved range of SSA values to uncertainties in surface albedo, aerosol optical depth, and size distribution. As discussed in Chapter 3, best-fit SSA were determined where the relative error (Equation 3.18) between the DDR calculated using TUV and the UVMRP DDR was at a minimum. The determination of best-fit SSA was possible as the data were additionally constrained by aerosol size distribution and refractive index. September 13th was chosen because of the availability of AERONET 440nm refractive index and AERONET and SMPS size distribution data in the morning hours. Additionally, the full retrieval was run for SZA's less than 75^{o} instead of the

65^{o} SZA set at the SZA criteria described in Chapter 3 to select a time period over which AERONET 440nm refractive index and size distribution were assumed valid.

Surface Albedo

As discussed in the previous chapter, the DDR is strongly dependent on the surface albedo and thus it is essential to use an accurate albedo value to ensure quality retrieval results. To test the effect of albedo on retrieved results, the full retrieval was run for both wavelengths using three surface albedos: 0.01, 0.05, and 0.1. Values were chosen to represent the full range of possible surface albedos within an urban setting [e.g., *Castro et al.*, 2001]. SMPS size distributions and UVMRP AOD were used as input.

Best-fit SSA_{368} and SSA_{332} values determined using each albedo value are shown in Figure 4.44 and Figure 4.45, respectively. Best-fit SSA values at both wavelengths appear to decrease in the morning hours and trend together no matter what input surface albedo is used, however the magnitude of the best-fit SSA_{368} and SSA_{332} values are different depending on the value used for surface albedo. As shown in Figures 4.44 and 4.45, the darker the surface (and therefore the lower the surface albedo) the brighter the retrieved SSA_{368} and SSA_{332} values. For a 0.1 increase in surface albedo, average best-fit SSA_{368} and SSA_{332}, determined by time-averaging all obtained best-fit SSA values for each wavelength, decreased by 0.02 for both wavelengths. However, all values of SSA_{368} and SSA_{332} fall within their respective ranges of SSA values (denoted by the gray shaded regions). Therefore, though the assumed surface albedo value of 0.05 used in the partial single-wavelength

retrieval method may not be the exact albedo of the two urban centers, it is expected to have minimal impact on the retrieval ranges of SSAs.

AOD

To examine how an expected AOD offset due to calibration errors may affect retrieval results, the full single-wavelength retrieval was run using extrapolated AOD values for 368nm and 332nm calculated using the Angstrom exponent determined from a linear fit through AERONET AOD values at 340nm and 380nm. Assuming AERONET CIMEL $V_{o,\lambda}$ values are more stable and more accurate than the UV-MFRSR, the difference in UVMRP-derived AOD and extrapolated AOD is representative of the potential range in AOD values to be expected with incorrect UV-MFRSR $V_{o,\lambda}$ values. Krotkov et al [2005a] used this extrapolation method to determine 368nm and 332nm AOD and $V_{o,\lambda}$ values for the UV-MFRSR.

Best-fit SSA_{368} and best-fit SSA_{332} values are shown in Figures 4.46 and 4.47 respectively and are denoted by the gold stars. Black stars represent best-fit SSA_{368} and best-fit SSA_{332} calculated using UVMRP AOD values. SMPS size distributions were used in both cases. The orange and red stars seen in both Figures are those best-fit SSA values determined using the AERONET size distribution as discussed in the following section.

Extrapolated AOD_{368} values were consistently higher than UVMRP AOD_{368} as show in Table 4.5. As seen in Figure 4.46 and Table 4.5, these higher AOD values yielded generally best-fit SSA_{368} values lower than those determined using UVMRP AOD_{368} values. Oppositely, as shown in Table 4.6 and Figure 4.47, extrapolated AOD_{332} values were generally lower than those determined by the UVMRP resulting

in higher best-fit SSA_{332} values than those calculated using UVMRP AOD_{332}. This relationship is best explained by the previous described relationship between the DDR, SSA, and AOD (Figure 3.7). The 1% relative error assumption and chosen range in g generally includes these potential offsets in AOD due to incorrect $V_{o,\lambda}$ as all best-fit SSA values lie within the SSA ranges. However, as seen in Figure 4.46, a value of best-fit SSA_{332} determined using the extrapolated AOD_{332} lies outside of the SSA_{332} range, possibly implying there is some additional error associated with the retrieval of AOD_{332} using the Langley method of the UVMRP.

Size Distribution

Both AERONET and SMPS size distribution data were used in the full retrieval phase of the single wavelength retrieval. Both size distribution data sets have desirable qualities as well as drawbacks. As described previously, the size bins of the AERONET distributions include a coarse mode and represent the optical properties of the aerosol column. However AERONET size distributions have limited availability as they correspond with AERONET almucantar measurements and inversion runs. Additionally, AERONET size distributions rely on a mathematical fitting model and are not direct observations. The SMPS size distributions, on the other hand, are high-resolution measured distributions. However, these measurements are only taken at the surface and thus may not include lofted transported particles such as dust and biomass burning aerosol that will substantially affect the surface radiation field. The SMPS also only measures particles up to 1 μm and therefore the SMPS distributions do not include the potentially important coarse mode.

Best-fit SSA_{368} and SSA_{332} determined using the available AERONET size distribution are shown in Tables 4.7 and Figures 4.46 and 4.47 and are represented by the red and orange stars, where the red star is the best-fit SSA value calculated using the extrapolated AOD values and the orange star is the best fit SSA value calculated using UVMRP AOD. The AERONET size distribution yields a decrease in best-fit SSA_{368} regardless of AOD value used with respect to the best-fit SSA_{368} calculated using the SMPS size distribution. Similarly, a decrease in best-fit SSA_{332} determined using the AERONET size distribution and UVMRP AOD_{332} is seen with respect to those best-fit SSA_{332} values calculated with the SMPS distribution and UVMRP AOD_{332}. However, as seen in Figure 4.46, the best-fit SSA_{332} calculated using the AERONET size distribution and extrapolated AOD_{332} values is equal to the best-fit SSA_{332} value calculated using the SMPS size distribution and extrapolated AOD_{332}, suggesting the retrieval of SSA is more sensitive to AOD values rather than size distribution. This is reflected in the use of a range of g values that produce DDR values within 1% of the measured DDR values over a small range in SSA. Similar to comparisons made between full retrieval results obtained with different values of AOD and partial single-wavelength results, differences in size distributions are also captured with the exception of one data point (AERONET size distribution, extrapolated AOD) at 332nm.

4.3.2 Optimal Estimation Comparison

The OE algorithm described in Chapter 3 was used to retrieve SSA_{368} and SSA_{332} for the morning hours (724 to 939 CST) on September 13th for temporal

consistency with the full single wavelength tests. Retrievals were run using the default retrieval settings and *a priori* values reported in Table 3.7. Retrievals were also run for a two additional values of *a priori* SSA (0.80 and 0.90) values and under two retrieval scenarios: one in which all the wavelengths (300nm, 305nm, 311nm, 317nm, 325nm, 332nm, and 368nm) were considered in the solution matrix and the other in which all but the wavelength of interest (either 332nm or 368nm) were effectively removed from the solution matrix via methods discussed in Chapter 3.

OE retrieval results for 368nm and 332nm are shown in Figures 4.48 and 4.49, respectively. Regardless of the *a priori* SSA value and the number of wavelengths considered in the solution matrix, all retrieval results appear to trend with one another. These trends in both OE retrieved SSA_{368} and SSA_{332} also appear fairly consistent with the average values of SSA_{368} and SSA_{332} obtained with the partial single-wavelength method for the morning hours of the 13^{th} as both OE SSA values and the partial single wavelength SSA values remain fairly constant over the two hour period.

While the trends of the OE results and the partial single-wavelength results seem to be in agreement, there is a substantial difference in the magnitude of retrieved values. First to notice is that there are notable differences between OE results. When all wavelengths are considered in the solution matrix, averaged values of both OE SSA_{368} and SSA_{332} increased by 0.04 with increases in the *a priori* values of SSA by 0.1. Additional increases in the SSA values are also seen when only one wavelength was considered in the solution matrix. The largest average OE SSA values were obtained with only one wavelength considered in the solution matrix and

with *a priori* SSA values of 0.9 for both wavelengths with values of 0.924 and 0.920 for 368nm and 332nm, respectively. Even more striking are the differences in the OE SSA values and the partial single-wavelength SSA values. As shown in Figures 4.48 and 4.49, regardless of the *a priori* SSA values and the number of wavelengths considered in the solution matrix, OE SSA_{368} are not within the 1% relative error and g-range bounds that define the ranges of SSA_{368} values for the partial single wavelength retrieval. Those OE SSA_{332} values retrieved using 332nm only in the solution matrix and an *a priori* SSA value of 0.90 do appear to fall within the lower bounds of the partial retrieval SSA_{332} range however, the OE SSA_{332} still remain substantially below the average SSA_{332} values.

This considerable difference is likely due to the additional error in the OE algorithm associated with error in the input irradiance values at the lower UV-MFRSR channels. As discussed in Chapter 2, there is concern regarding the accuracy in the measured irradiance and calculated AOD at the shorter-wavelength channels of the UV-MFRSR due to the presence of strongly absorbing trace gases not considered in the determination of the $V_{o,\lambda}$. Since the OE algorithm reaches a solution through the minimization of the error associated with the whole system, this error in the measurement will effect the OE retrieval of SSA at the longer wavelength channels. When these shorter-wavelengths are not considered, the OE algorithm is still incorporating the error associated with the $V_{o,\lambda}$ values used to calibrate the longer wavelength channels through it's use of the independent measurements of the direct and diffuse irradiance to determined aerosol optical properties. Such error is not considered in the partial single wavelength method through the use of the DDR.

These sources of error can be significant and need to be considered in the OE algorithm to ensure accuracy of retrieved UV optical properties.

Table 4.1 Daily SSA values for the MILAGRO retrieval days.

Date	*Daily-averaged SSA_{368}*	*Daily-averaged SSA_{332}*
03/12	0.710	0.699
03/13	0.649	0.638
03/19	0.606	0.557
03/21	0.699	0.635

Table 4.2 Maximum and mimimum average SSA_{368} and SSA_{332} values for the MILAGRO retrieval days.

Date	*Maximum Average SSA*		*Minimum Average SSA*	
	368nm	*332nm*	*368nm*	*332nm*
03/12	0.773	0.771	0.632	0.611
03/13	0.752	0.743	0.575	0.569
03/19	0.728	0.702	0.518	0.500
03/21	0.805	0.709	0.661	0.603

Table 4.3 Daily SSA values for the TexAQS II/GoMACCS retrieval days.

Date	*Daily-averaged SSA_{368}*	*Daily-averaged SSA_{332}*
08/31	0.816	0.802
09/03	0.969	0.936
09/07	0.911	0.895
09/13	0.962	0.924
09/14	0.892	0.869
10/05	0.946	0.926
10/06	0.935	0.908

Table 4.4 Maximum and mimimum average SSA_{368} and SSA_{332} values for the TexAQS II/GoMACCS retrieval days.

Date	*Maximum Average SSA*		*Minimum Average SSA*	
	368nm	*332nm*	*368nm*	*332nm*
08/31	0.868	0.854	0.738	0.757
09/03	1.000	0.971	0.845	0.903
09/07	0.942	0.924	0.865	0.873
09/13	0.983	0.956	0.929	0.896
09/14	0.982	0.914	0.845	0.842
10/05	0.963	0.934	0.934	0.919
10/06	0.949	0.921	0.925	0.894

Table 4.5 UVMRP and extrapolated AOD_{368} values and the resulting best-fit SSA_{368} values.

UVMRP AOD_{368}	*Extrapolated AOD_{368}*	*Best-fit SSA_{368}, UVMRP AOD*	*Best-fit SSA_{368}, Extrapolated AOD*
0.648	0.655	0.992	0.984
0.621	0.627	0.992	0.985
0.653	0.694	0.993	0.944
0.602	0.633	0.986	0.951
0.619	0.637	0986	0.965

Table 4.6 UVMRP and extrapolated AOD_{332} values and the resulting best-fit SSA_{332} values.

UVMRP AOD_{332}	*Extrapolated AOD_{332}*	*Best-fit SSA_{332}, UVMRP AOD*	*Best-fit SSA_{332}, Extrapolated AOD*
0.778	0.726	0.976	1.00
0.749	0.696	0.965	1.00
0.760	0.759	0.959	0.959
0.708	0.696	0.953	0.966
0.717	0.697	0949	0.967

Table 4.7 Best-fit SSA_{368} and SSA_{332} calculated using several combinations of AOD and size distribution data sets.

	UVB AOD, SMPS Distribution	*Extrapolated AOD, SMPS Distribution*	*UVB AOD, AERONET Distribution*	*Extrapolated AOD, AERONET Distribution*
368nm	0.992	0.984	0.972	0.960
332nm	0.972	1.000	0.953	1.000

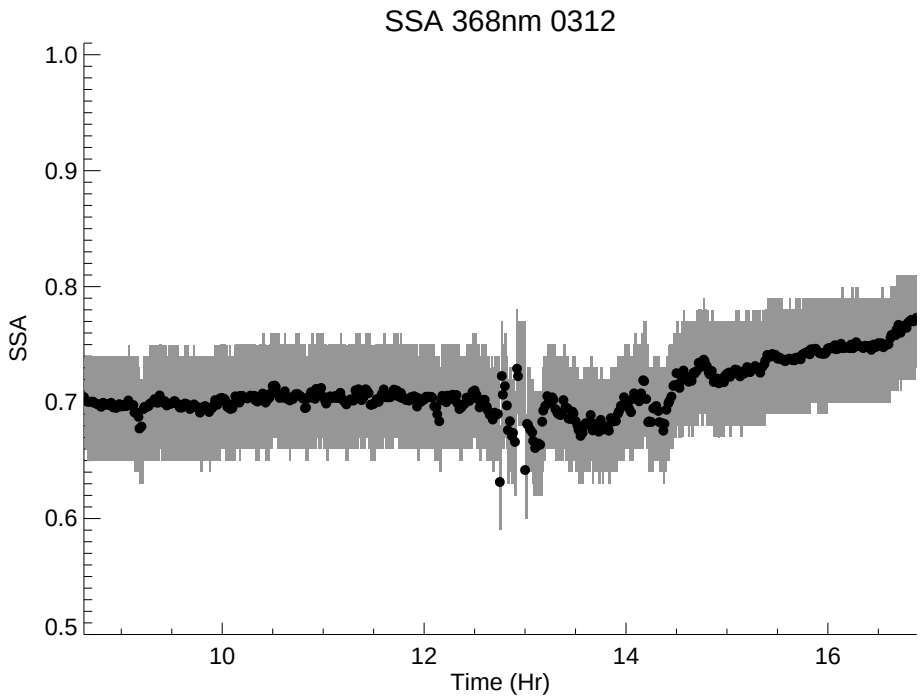

Figure 4.1 Ranges of SSA_{368} (gray area) and average SSA_{368} (points) values for March 12th during MILAGRO.

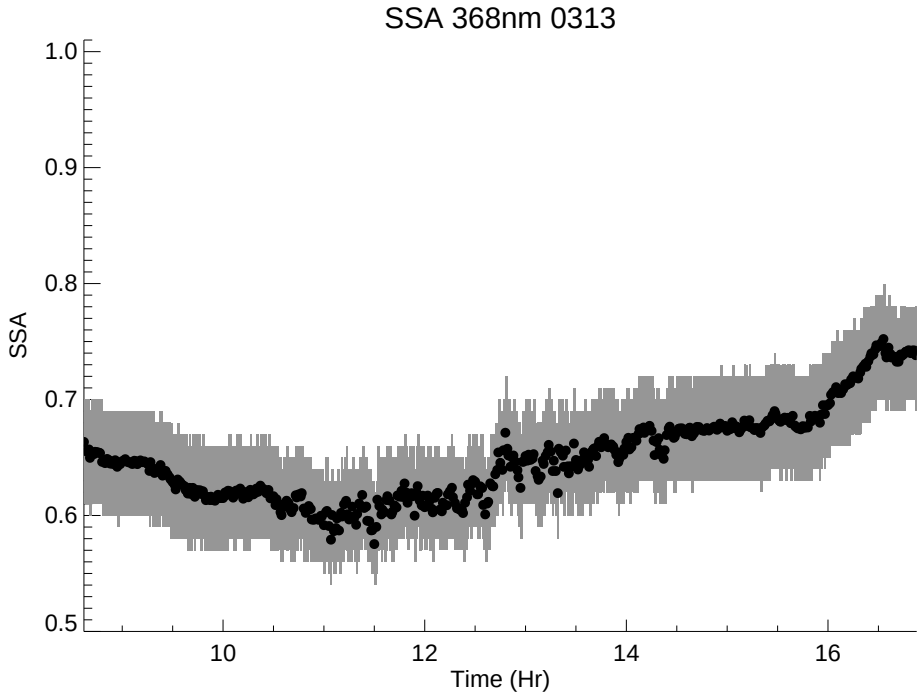

Figure 4.2 Ranges of SSA_{368} (gray area) and average SSA_{368} (points) values for March 13th during MILAGRO.

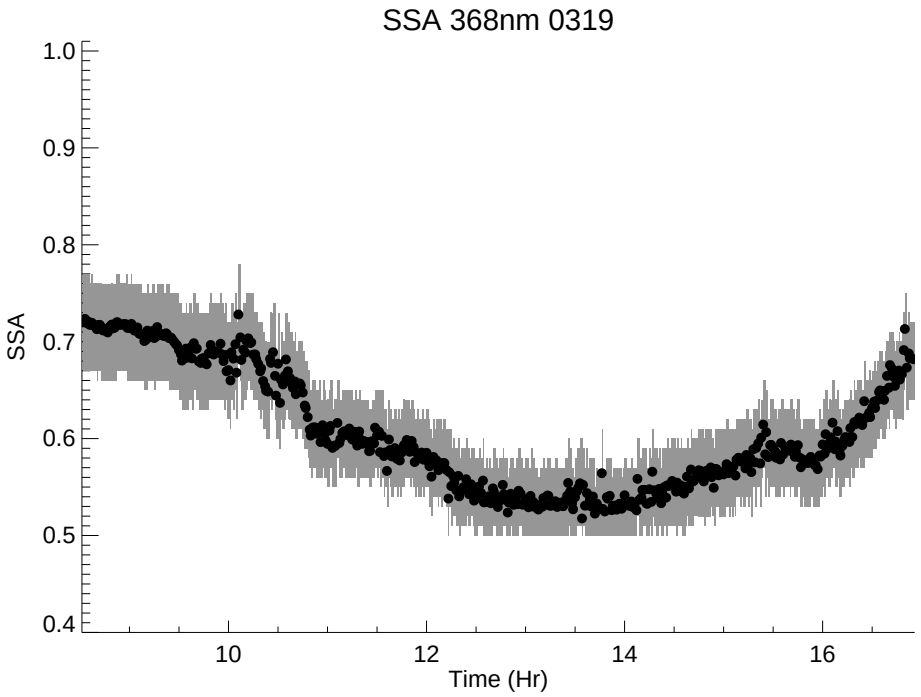

Figure 4.3 Ranges of SSA_{368} (gray area) and average SSA_{368} (points) values for March 19th during MILAGRO.

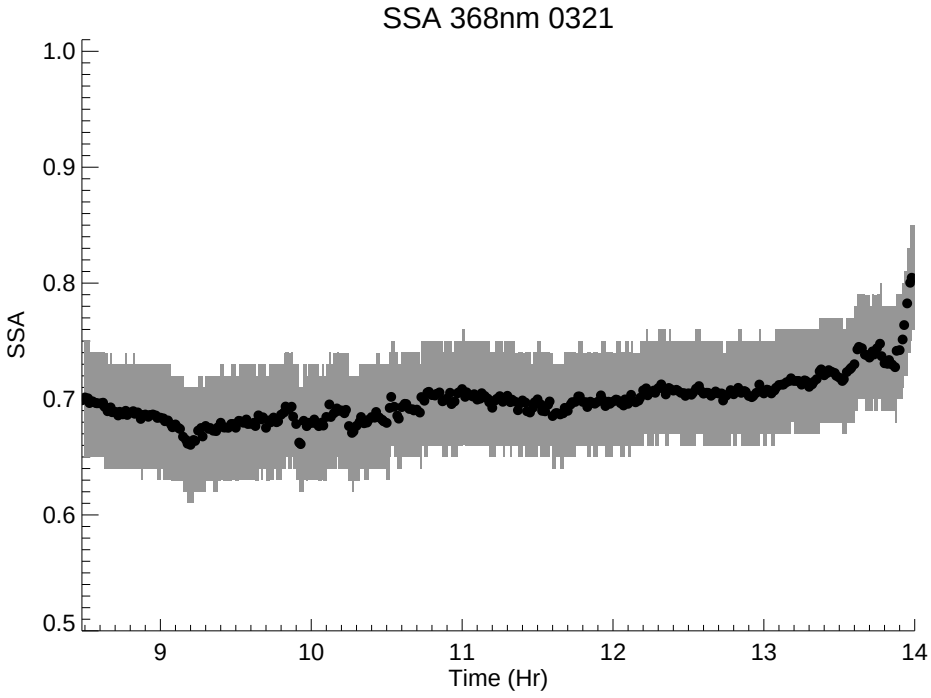

Figure 4.4 Ranges of SSA_{368} (gray area) and average SSA_{368} (points) values for March 21st during MILAGRO.

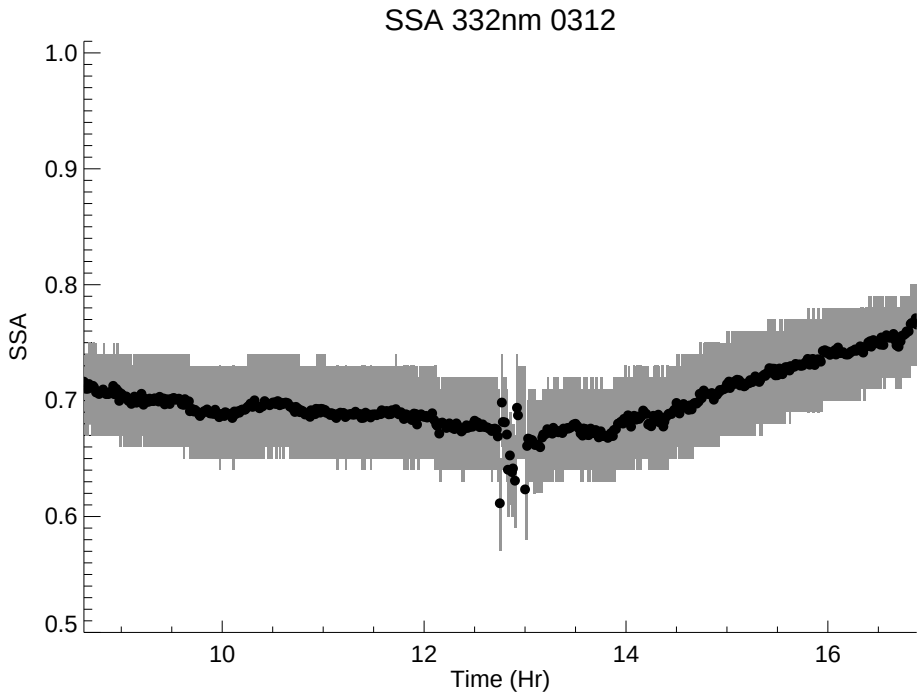

Figure 4.5 Ranges of SSA_{332} (gray area) and average SSA_{332} (points) values for March 12th during MILAGRO.

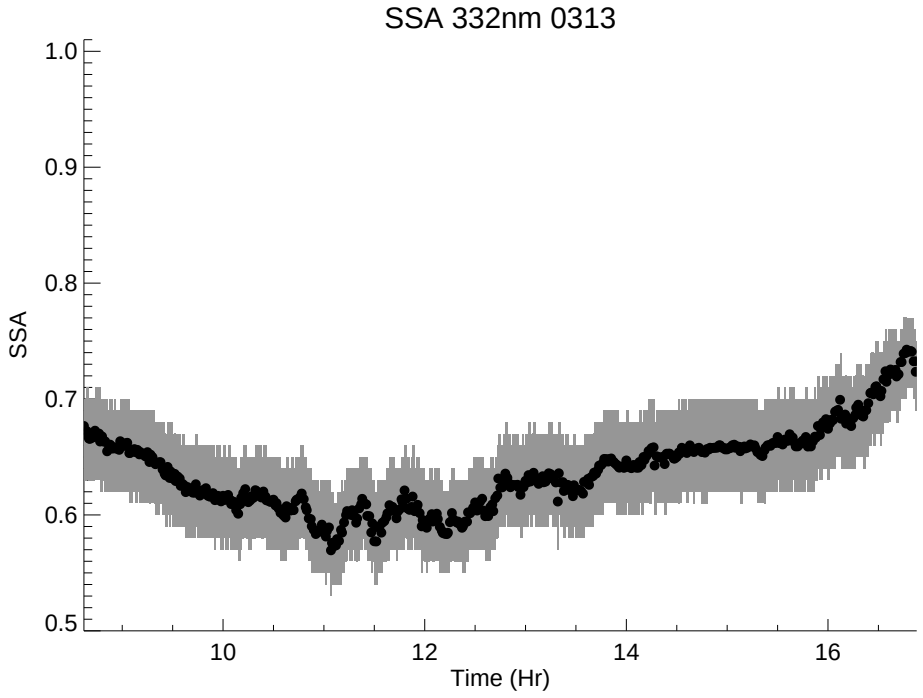

Figure 4.6 Ranges of SSA_{332} (gray area) and average SSA_{332} (points) values for March 13th during MILAGRO.

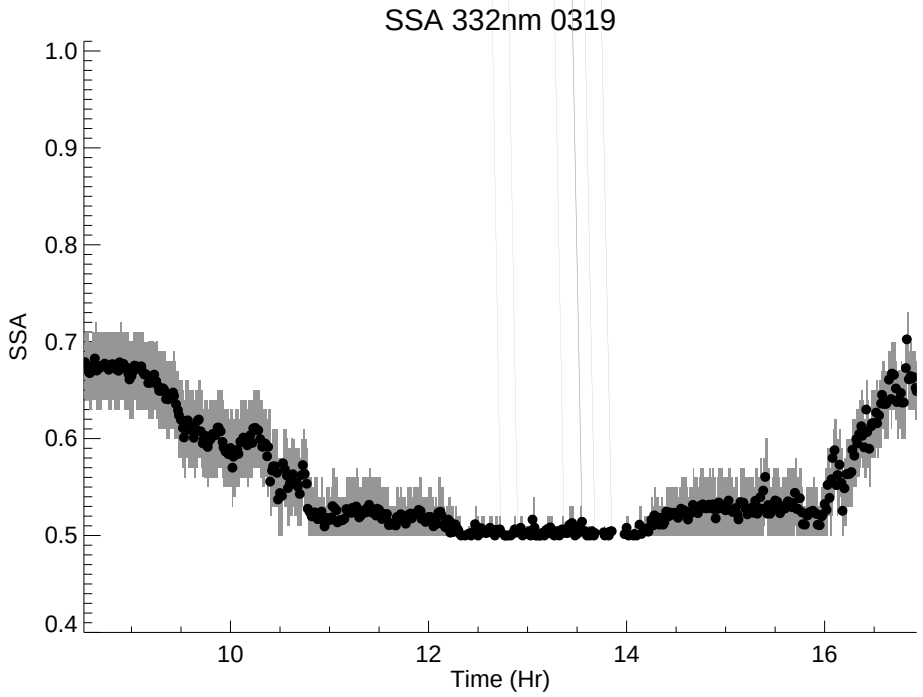

Figure 4.7 Ranges of SSA_{332} (gray area) and average SSA_{332} (points) values for March 19th during MILAGRO.

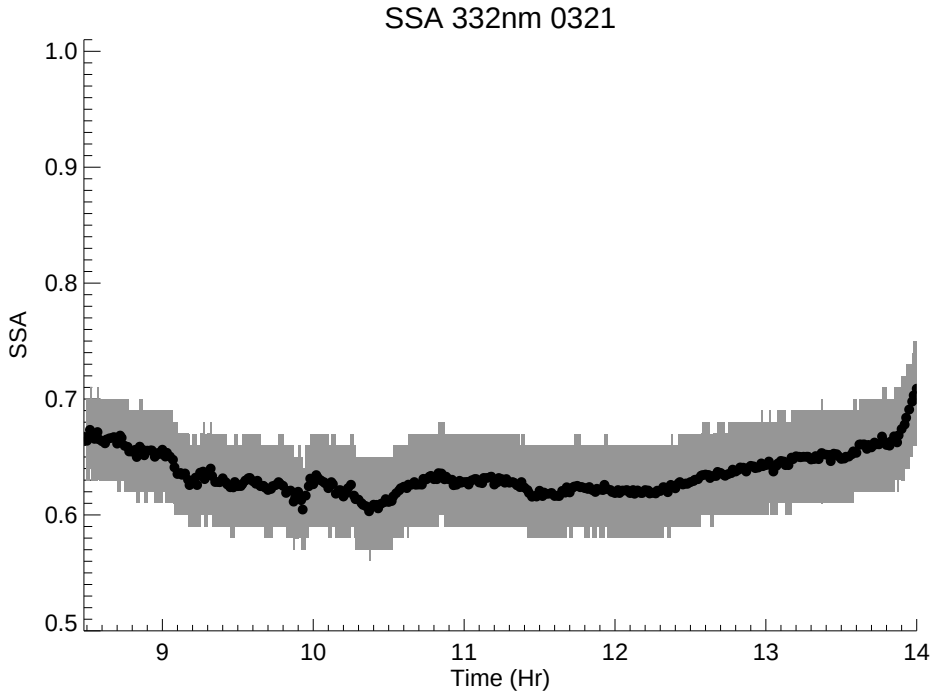

Figure 4.8 Ranges of SSA_{332} (gray area) and average SSA_{332} (points) values for March 21st during MILAGRO.

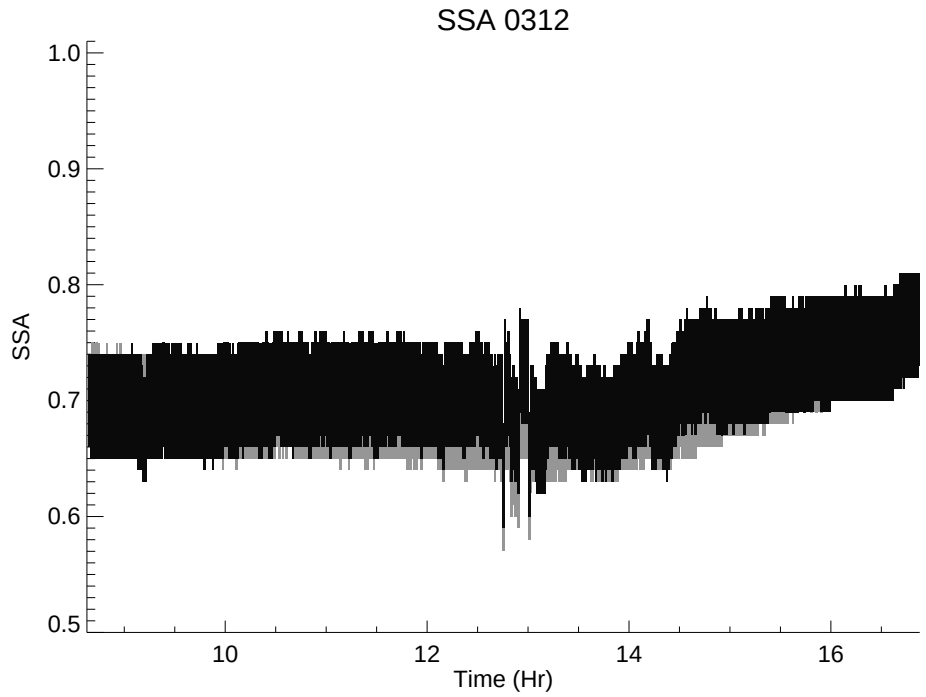

Figure 4.9 Ranges of SSA_{368} (black) and SSA_{332} (gray) for March 12th during MILAGRO.

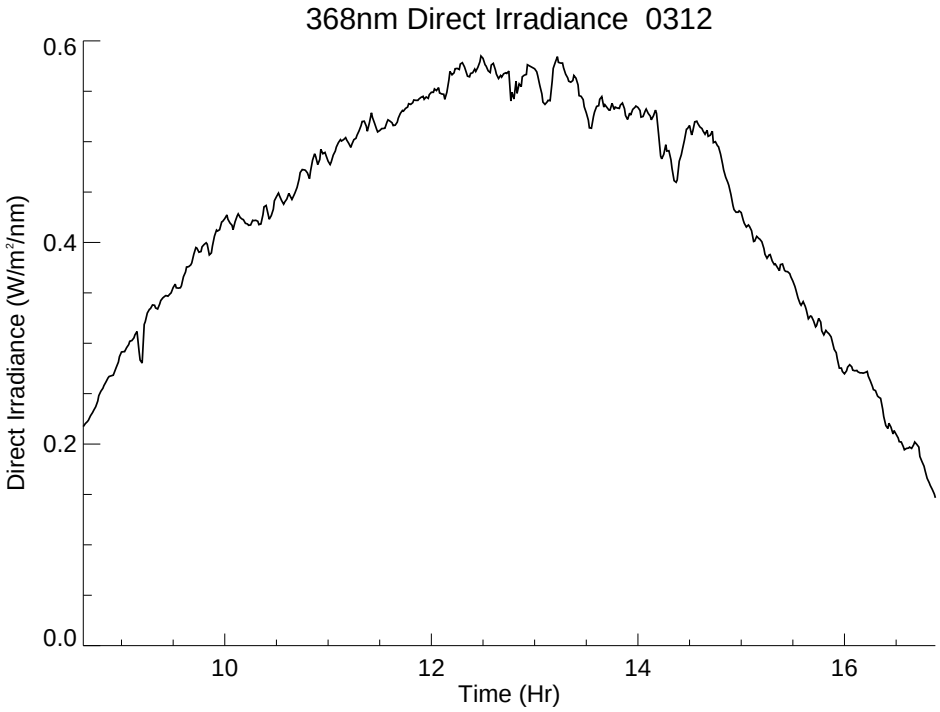

Figure 4.10 The 368nm direct irradiance profile for March 12th during MILAGRO.

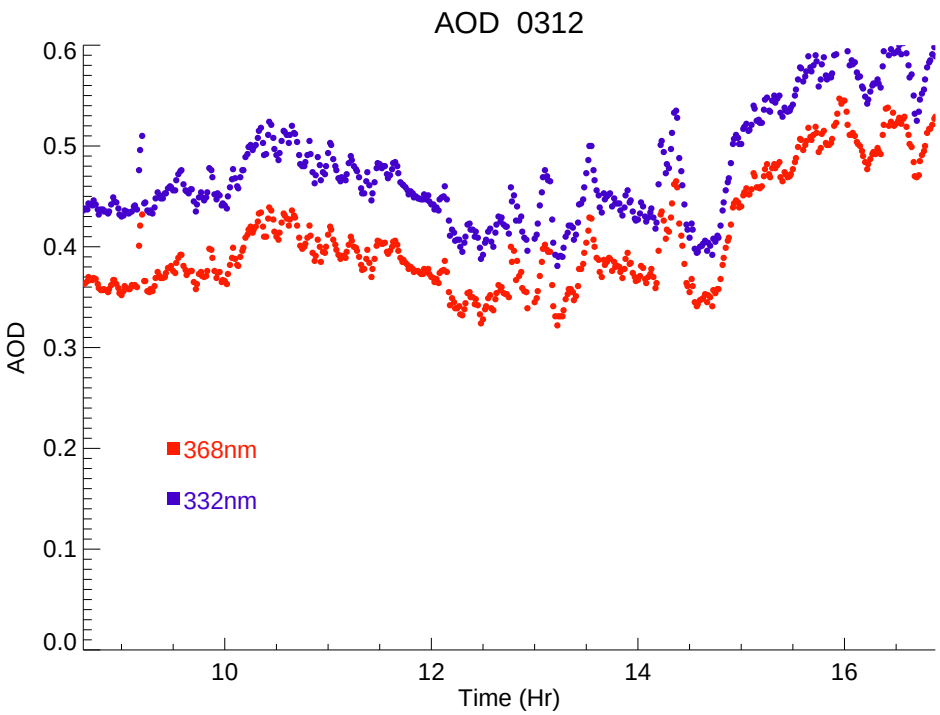

Figure 4.11 UVMRP AOD_{368} (red) and AOD_{332} (blue) values for March 12th during MILAGRO.

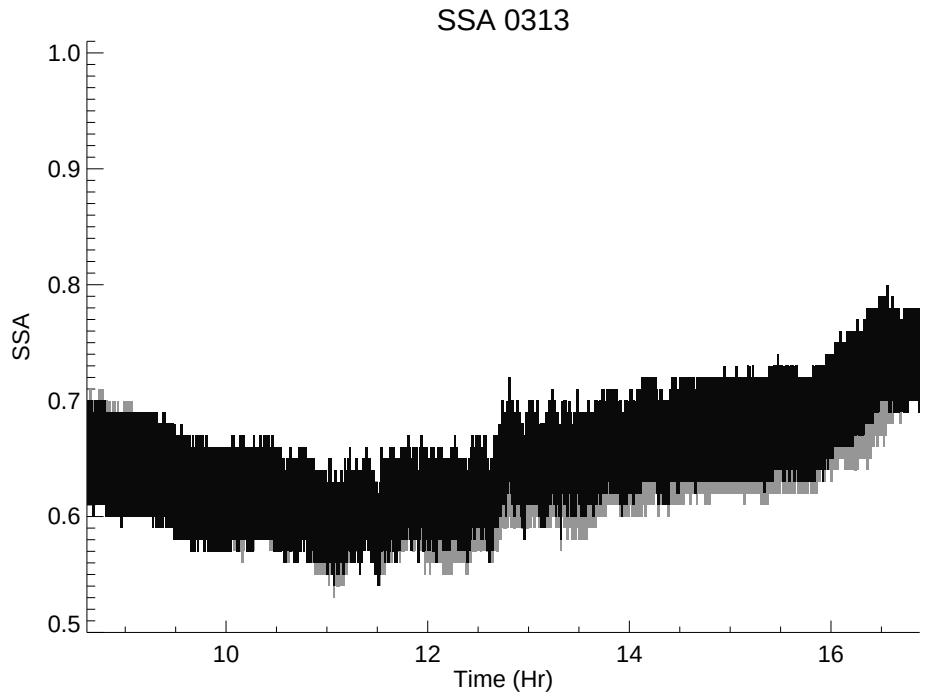

Figure 4.12 Ranges of SSA_{368} (black) and SSA_{332} (gray) for March 13th during MILAGRO.

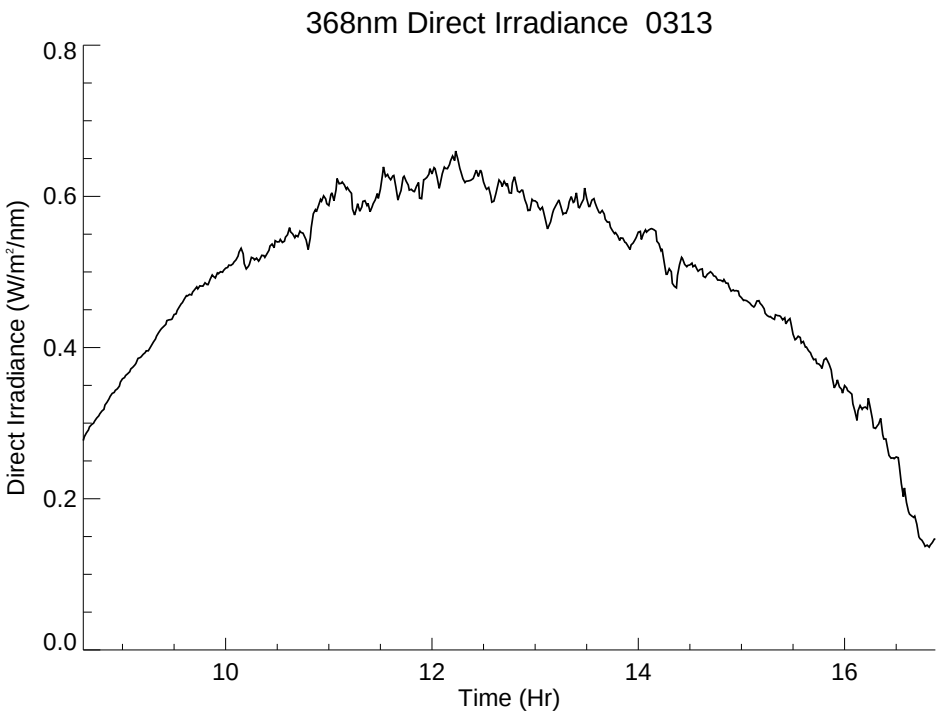

Figure 4.13 The 368nm direct irradiance profile for March 13th during MILAGRO.

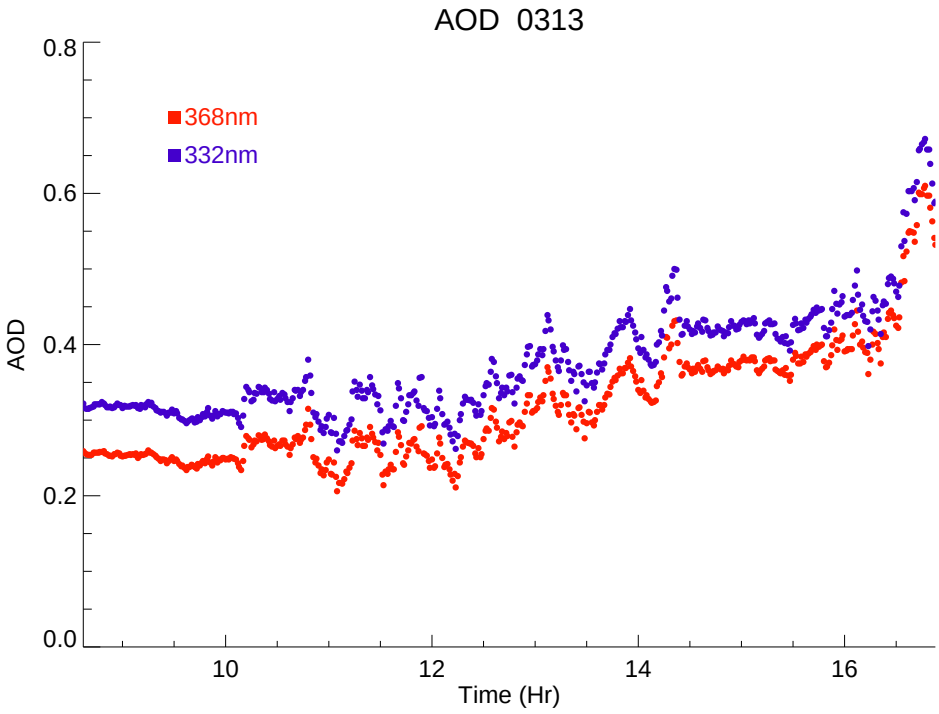

Figure 4.14 UVMRP AOD_{368} (red) and AOD_{332} (blue) for March 13th during MILAGRO.

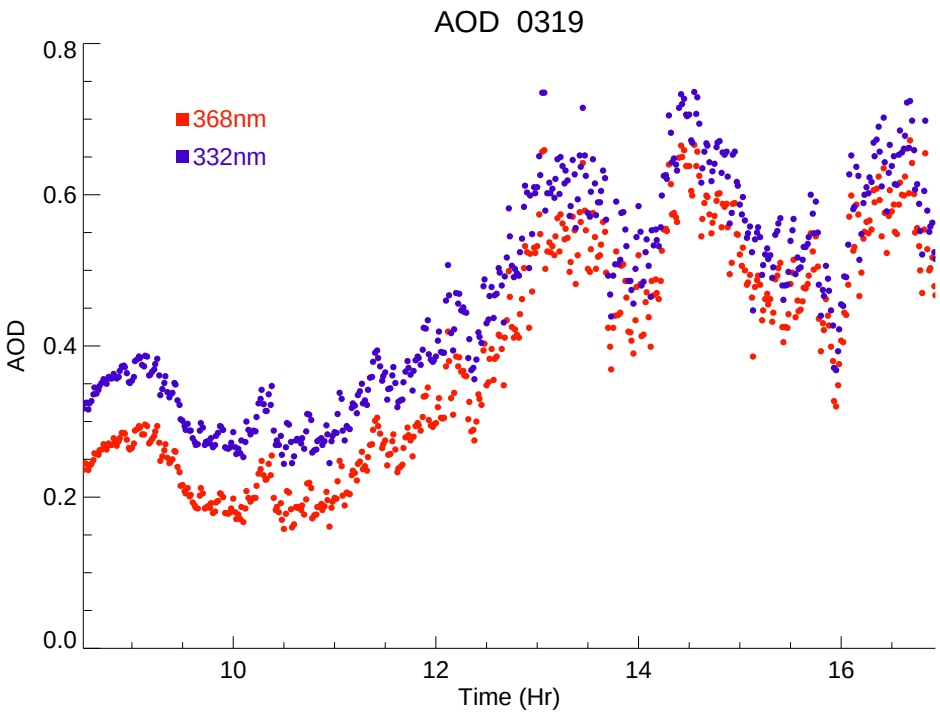

Figure 4.15 UVMRP AOD_{368} (red) and AOD_{332} (blue) for March 19th during MILAGRO.

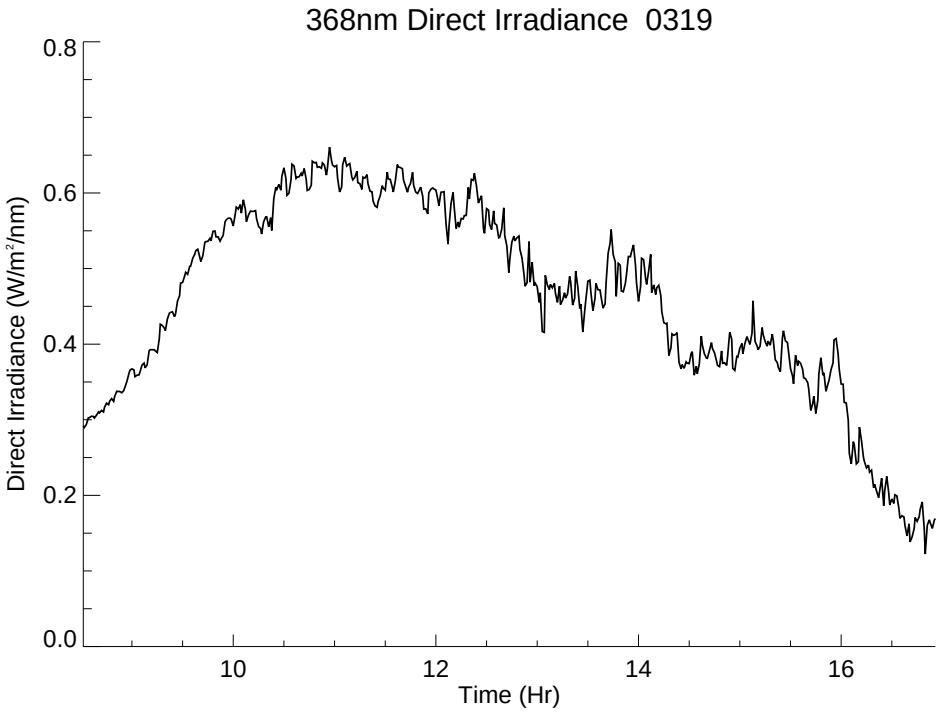

Figure 4.16 The 368nm direct irradiance profile for March 19th during MILAGRO.

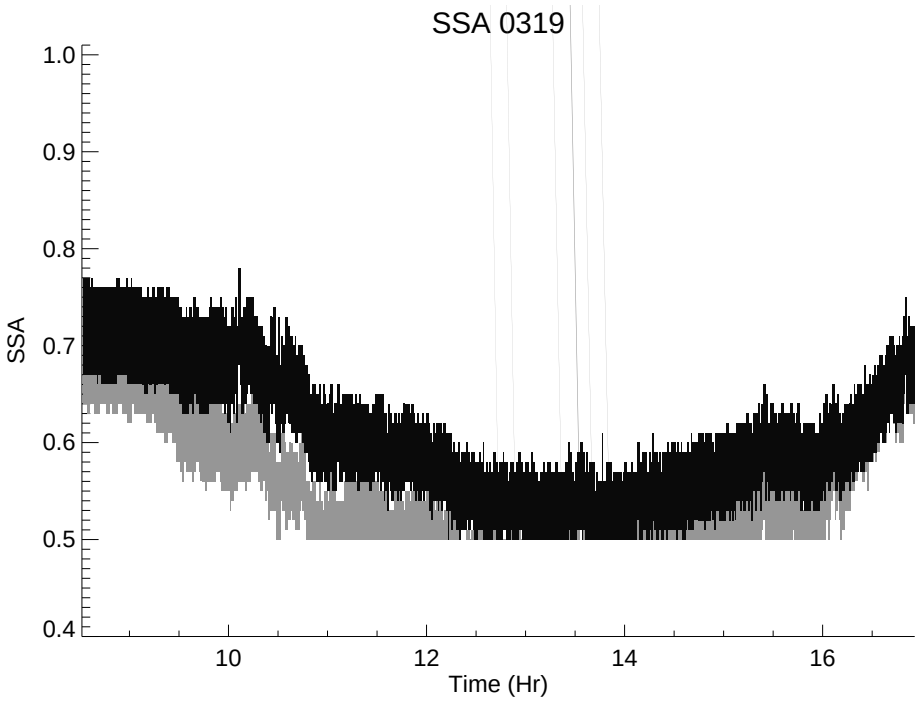

Figure 4.17 Ranges of SSA_{368} (black) and SSA_{332} (gray) for March 19th during MILAGRO.

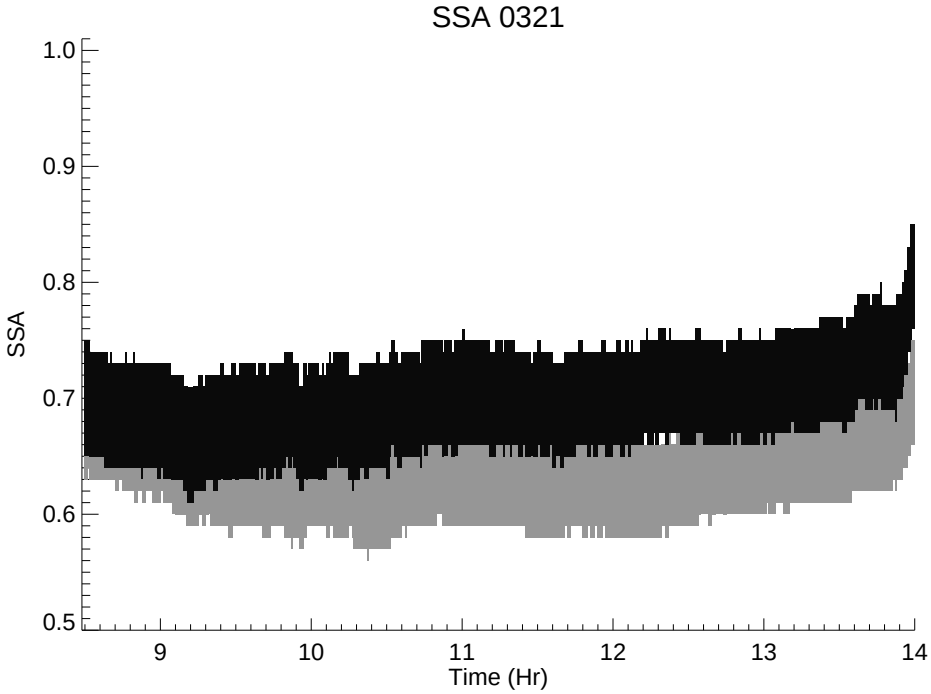

Figure 4.18 Ranges of SSA_{368} (black) and SSA_{332} (gray) for March 21st during MILAGRO.

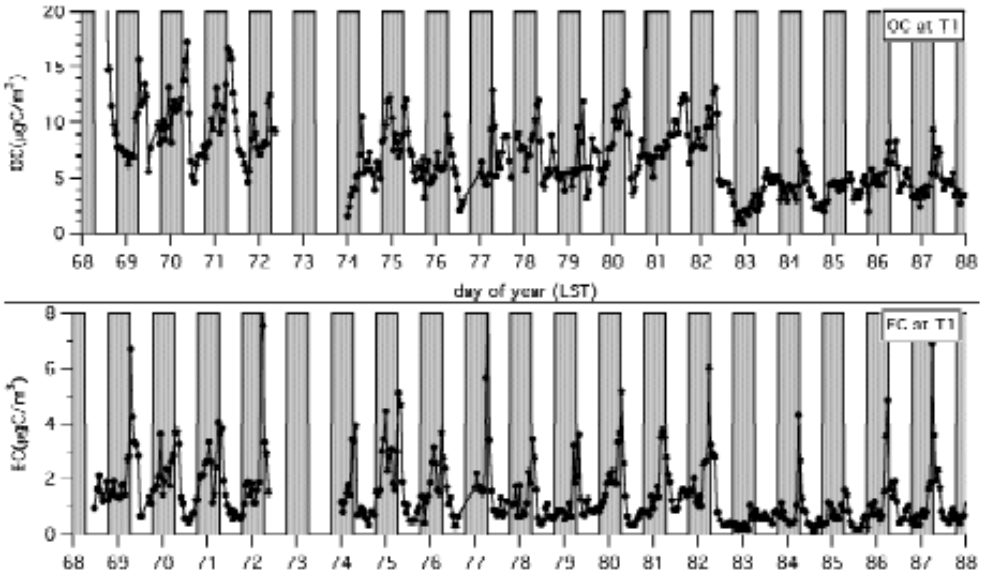

Figure 4.19 Organic carbon (top) and elemental carbon (bottom) measured at the T1 measurement site during MILAGRO from Doran et al [2007] from March 9th (day of year 68) to March 29th (day of year 88).

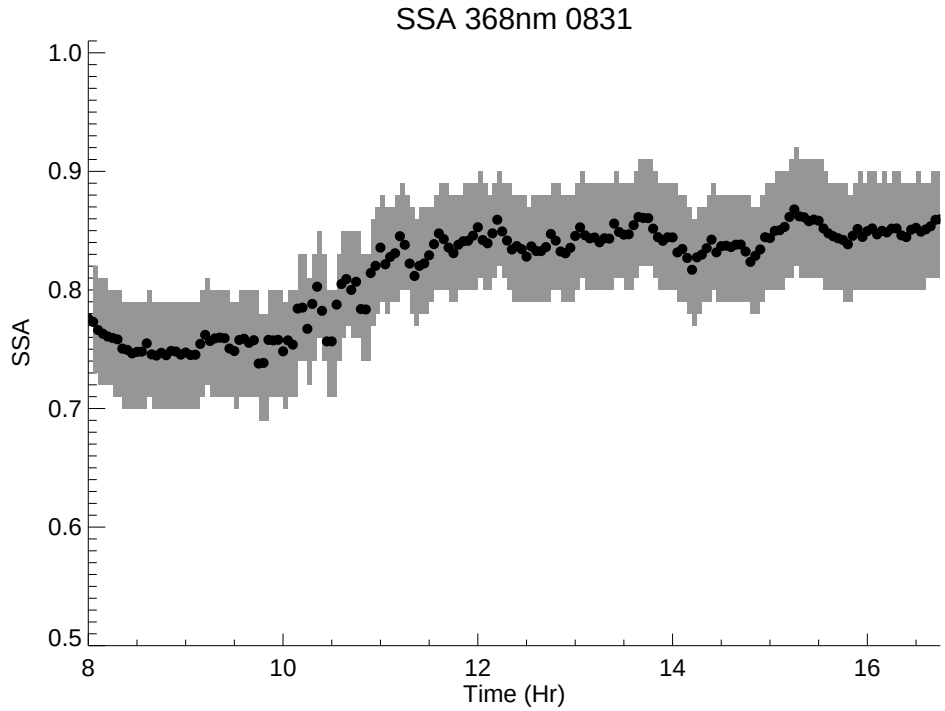

Figure 4.20 Ranges of SSA_{368} (gray area) and average SSA_{368} (points) values for August 31st during TexAQS II/GoMACCS.

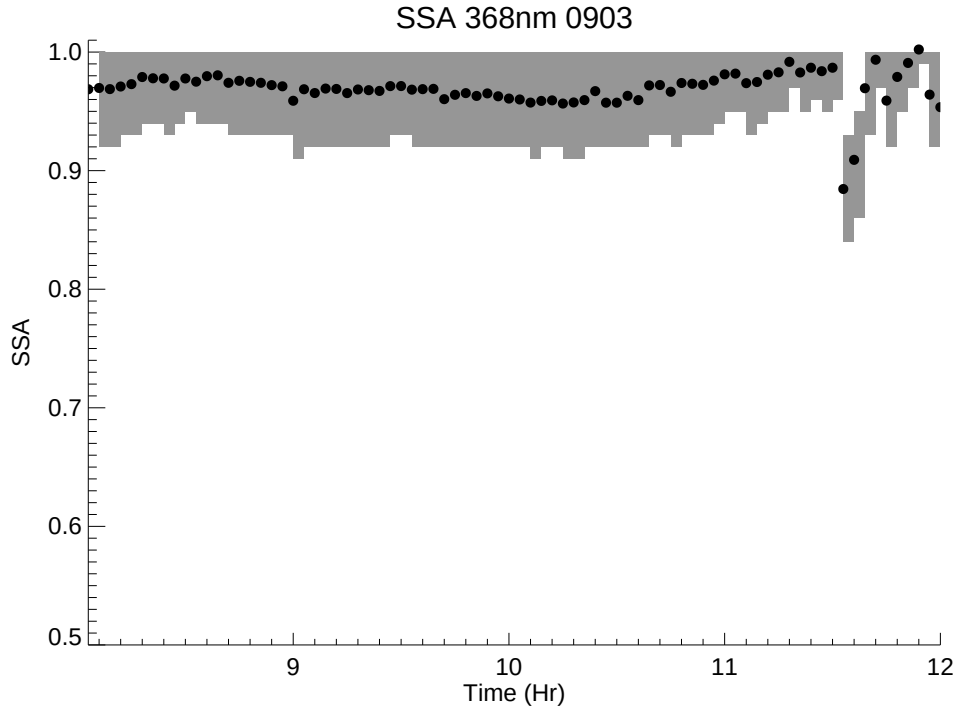

Figure 4.21 Ranges of SSA_{368} (gray area) and average SSA_{368} (points) values for September 3rd during TexAQS II/GoMACCS.

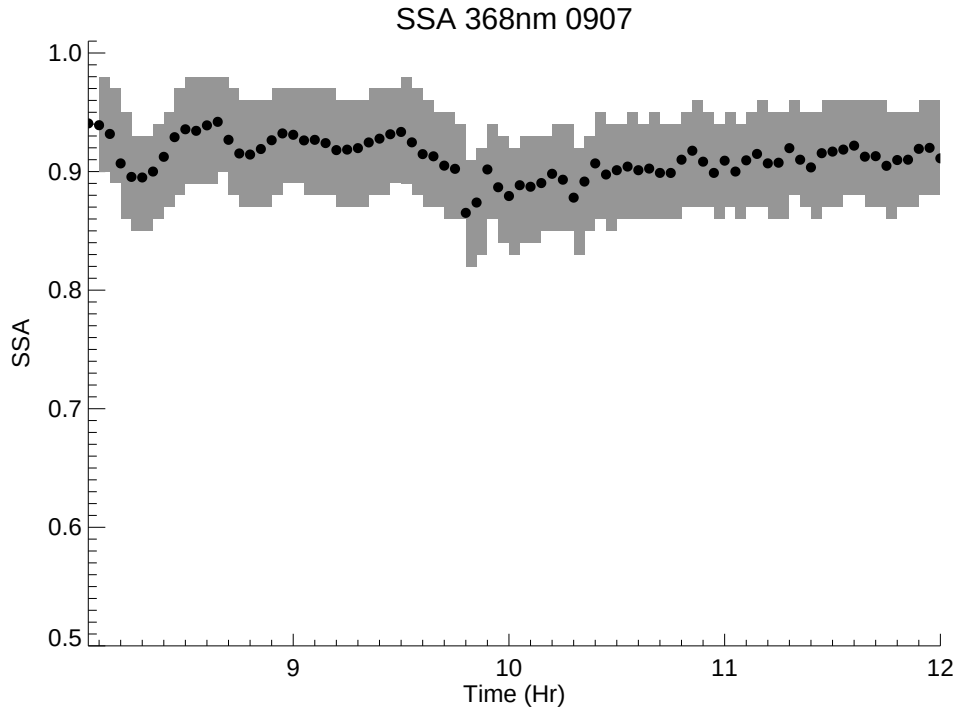

Figure 4.22 Ranges of SSA_{368} (gray area) and average SSA_{368} (points) values for September 7th during TexAQS II/GoMACCS.

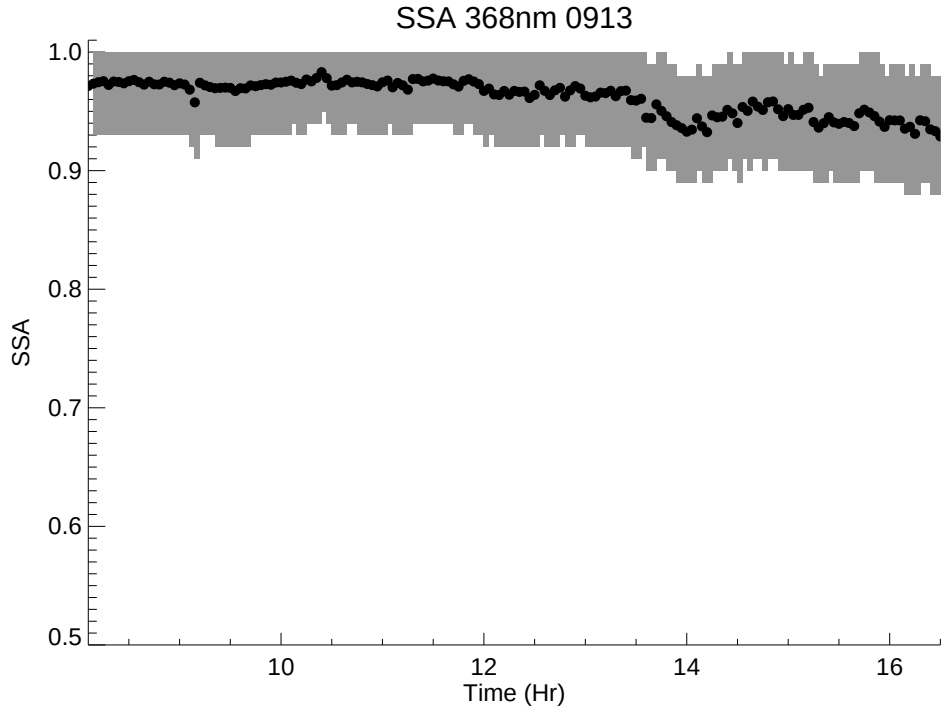

Figure 4.23 Ranges of SSA_{368} (gray area) and average SSA_{368} (points) values for September 13th during TexAQS II/GoMACCS.

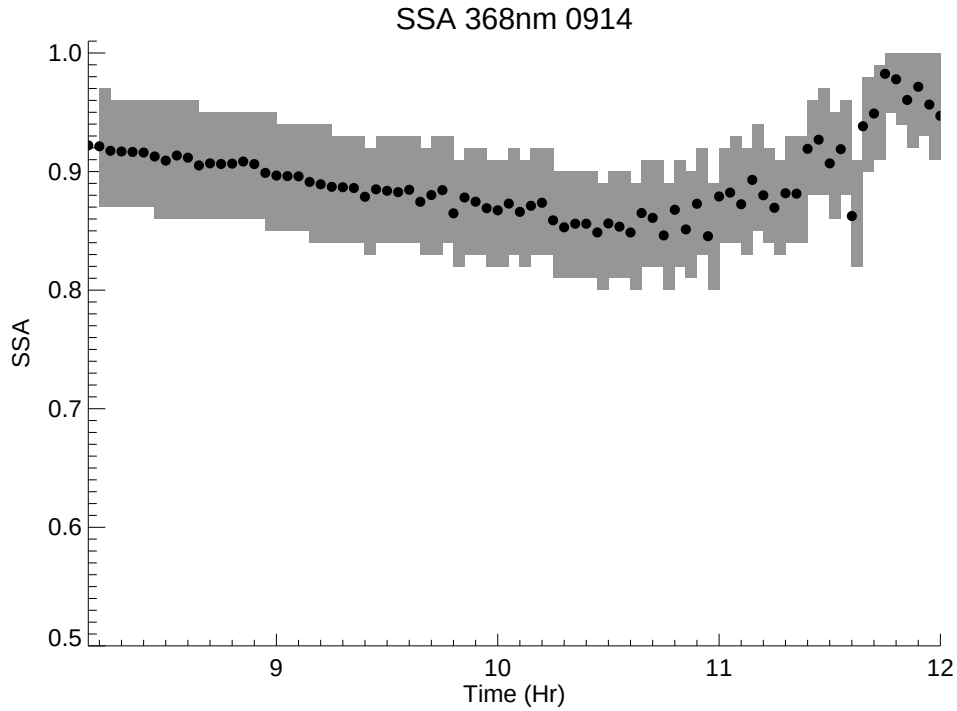

Figure 4.24 Ranges of SSA_{368} (gray area) and average SSA_{368} (points) values for September 14th during TexAQS II/GoMACCS.

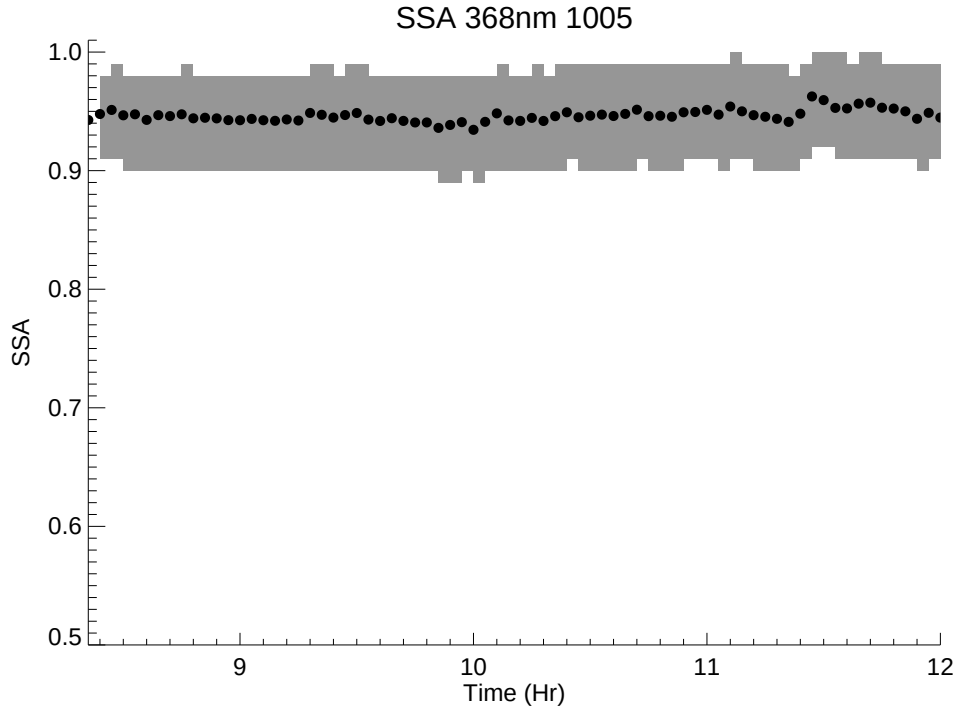

Figure 4.25 Ranges of SSA_{368} (gray area) and average SSA_{368} (points) values for October 5th during TexAQS II/GoMACCS.

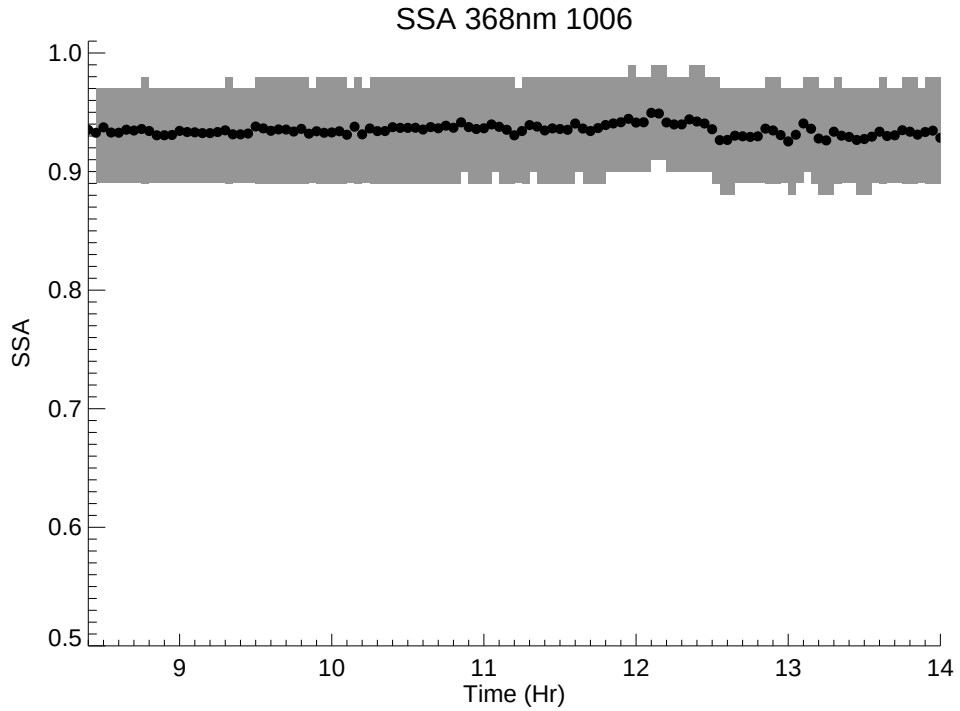

Figure 4.26 Ranges of SSA_{368} (gray area) and average SSA_{368} (points) values for October 6th during TexAQS II/GoMACCS.

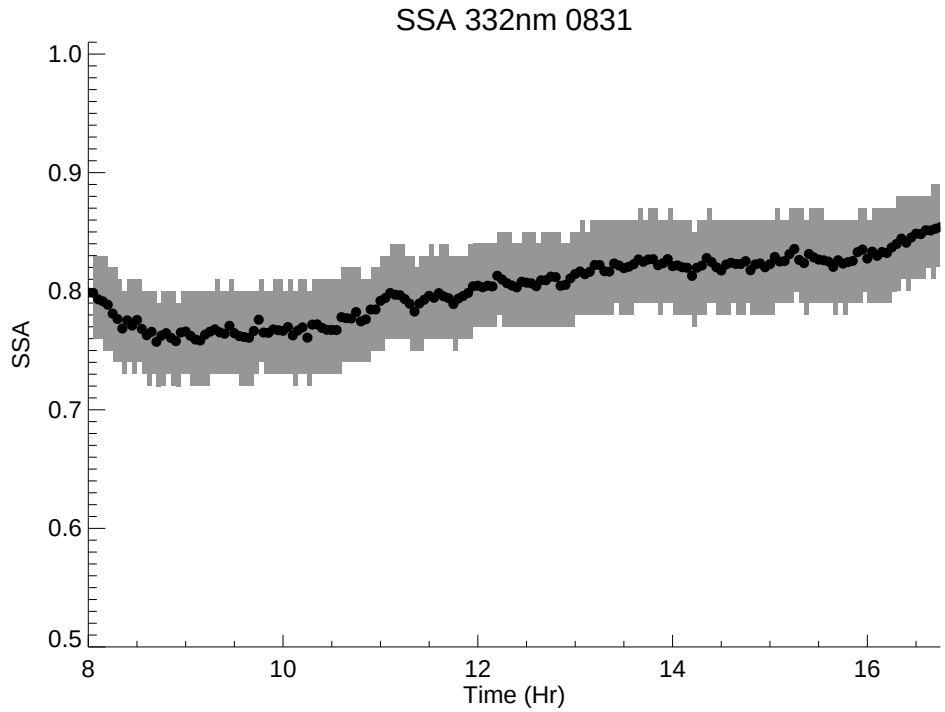

Figure 4.27 Ranges of SSA_{332} (gray area) and average SSA_{332} (points) values for August 31st during TexAQS II/GoMACCS.

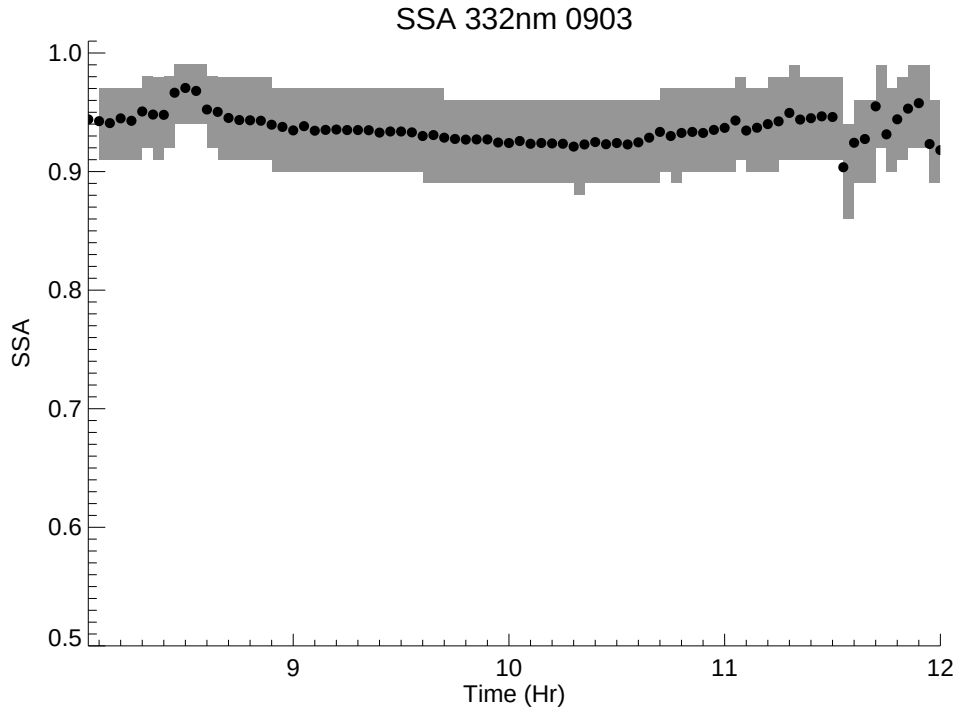

Figure 4.28 Ranges of SSA_{332} (gray area) and average SSA_{332} (points) values for September 3rd during TexAQS II/GoMACCS.

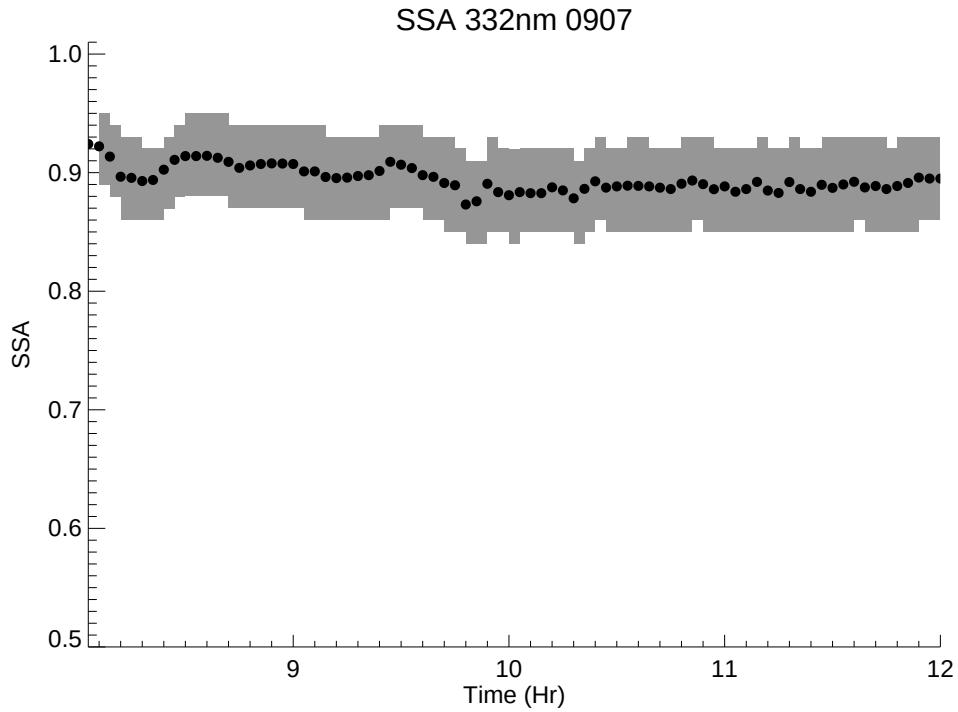

Figure 4.29 Ranges of SSA_{332} (gray area) and average SSA_{332} (points) values for September 7th during TexAQS II/GoMACCS.

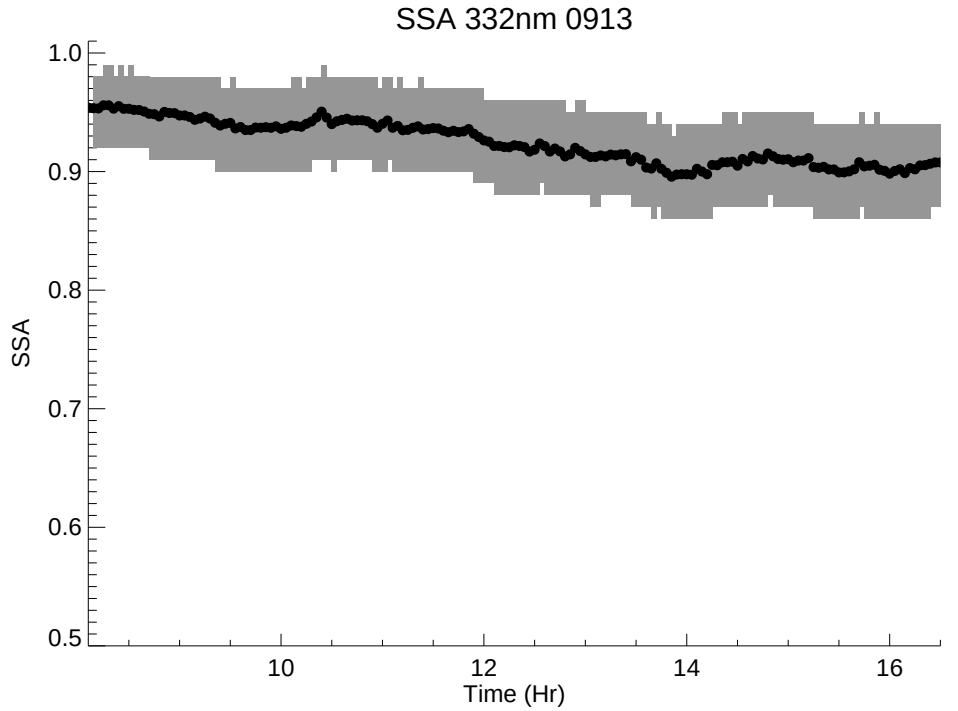

Figure 4.30 Ranges of SSA_{332} (gray area) and average SSA_{332} (points) values for September 13th during TexAQS II/GoMACCS.

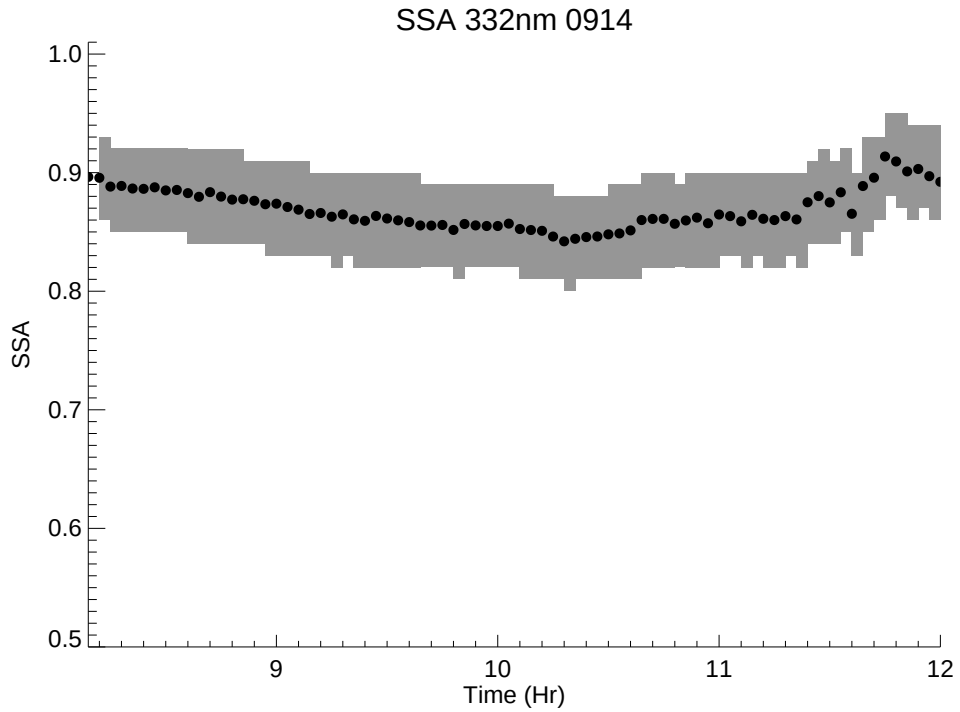

Figure 4.31 Ranges of SSA_{332} (gray area) and average SSA_{332} (points) values for September 14th during TexAQS II/GoMACCS.

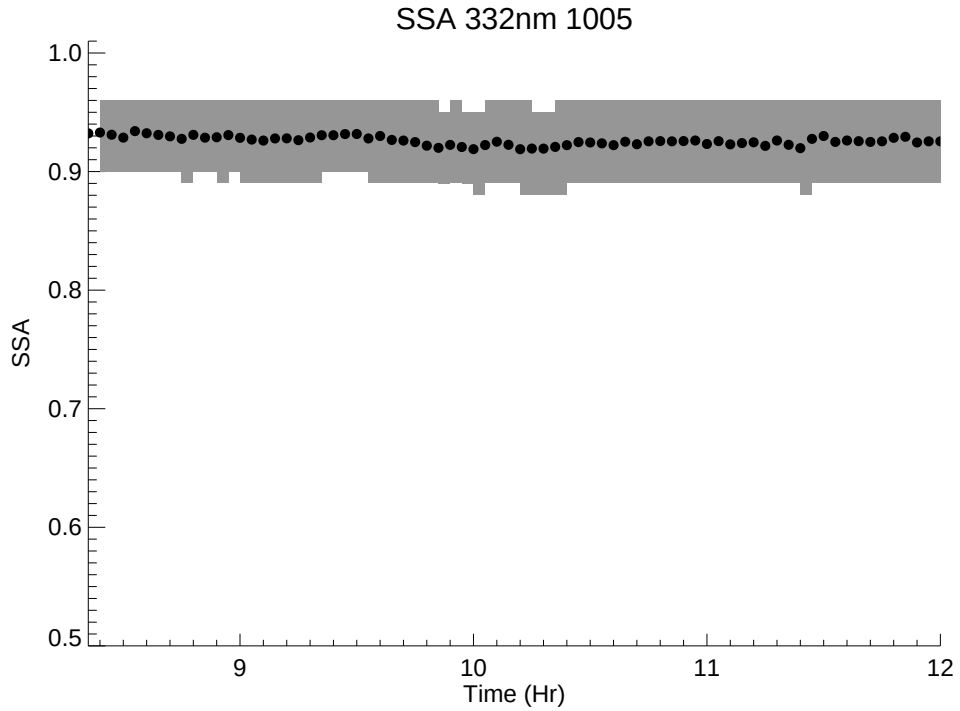

Figure 4.32 Ranges of SSA_{332} (gray area) and average SSA_{332} (points) values for October 5th during TexAQS II/GoMACCS.

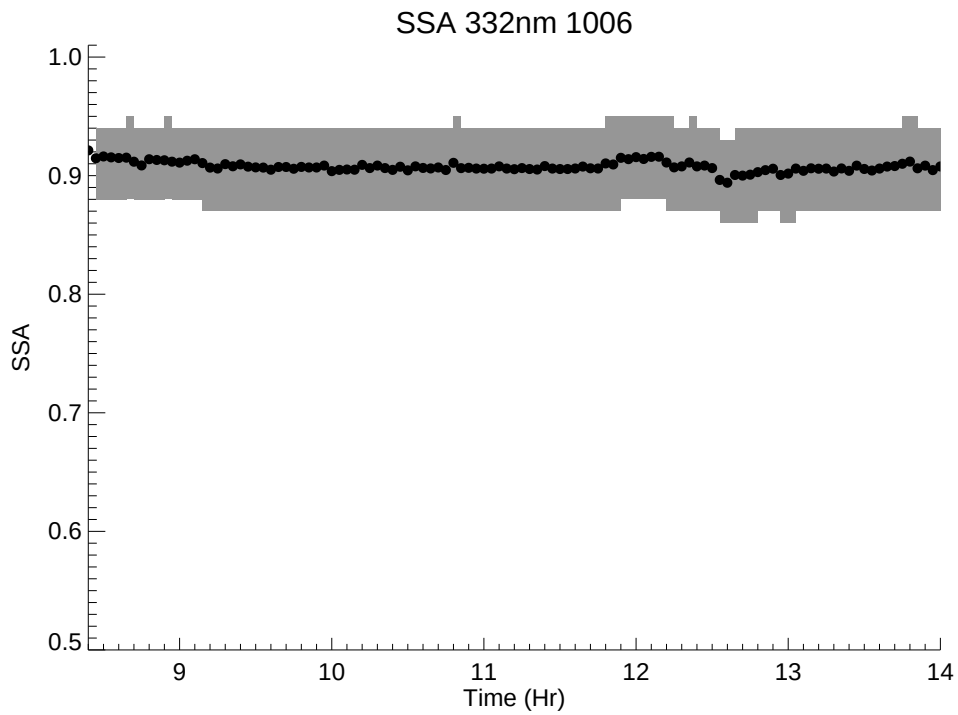

Figure 4.33 Ranges of SSA_{332} (gray area) and average SSA_{332} (points) values for October 6th during TexAQS II/GoMACCS.

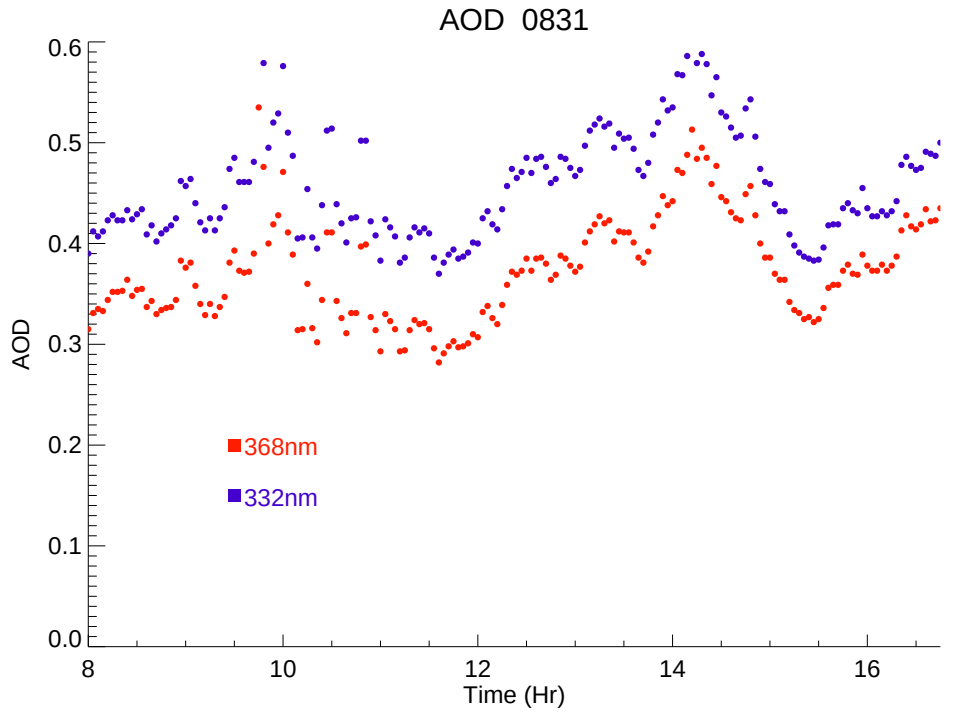

Figure 4.34UVMRP AOD_{368} (red) and AOD_{332} (blue) for August 31st during TexAQS II/GoMACCS.

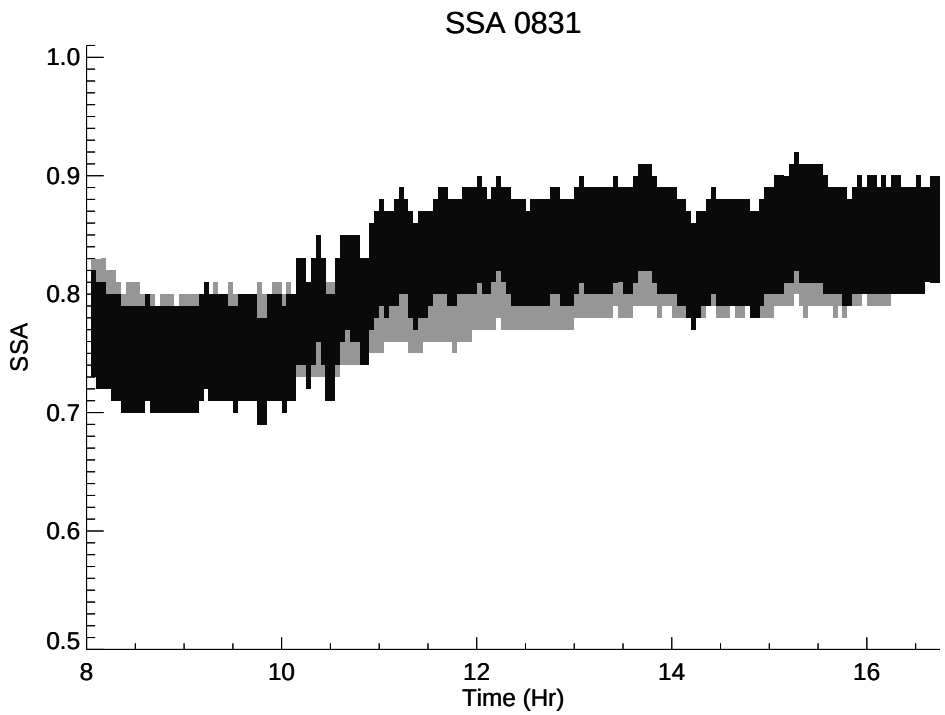

Figure 4.35 Ranges of SSA_{368} (black) and SSA_{332} (gray) for August 31st during TexAQS II/GoMACCS.

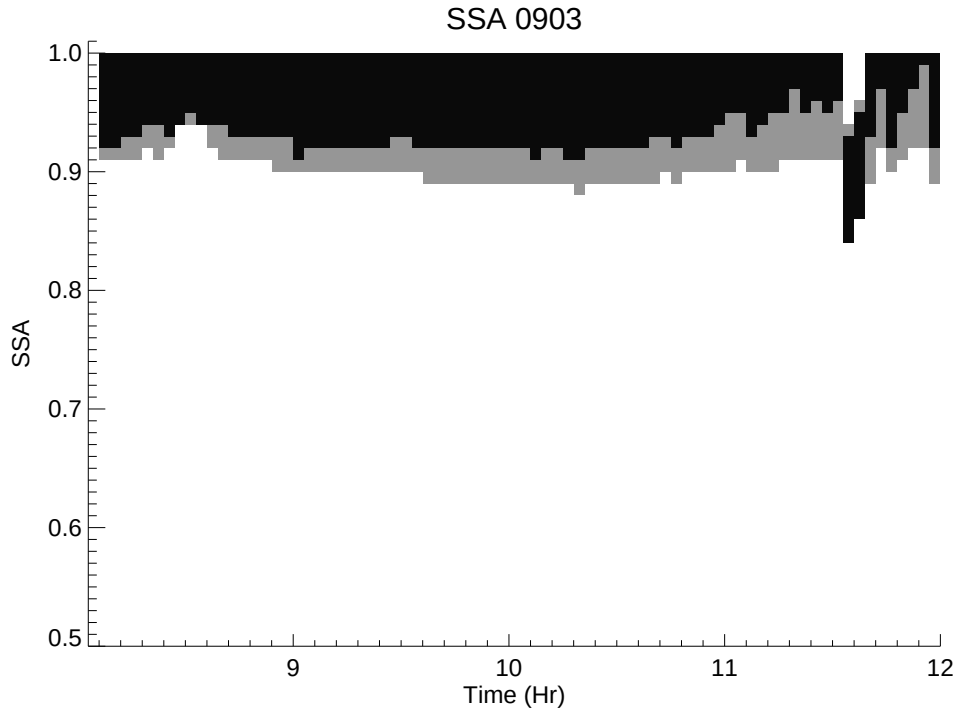

Figure 4.36 Ranges of SSA_{368} (black) and SSA_{332} (gray) for September 3rd during TexAQS II/GoMACCS.

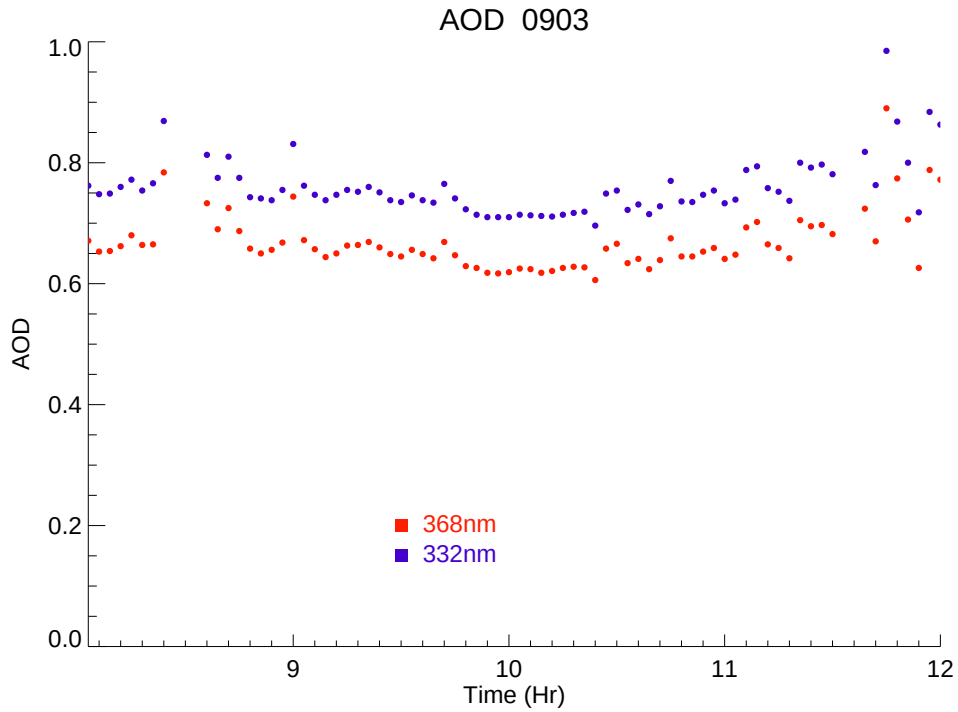

Figure 4.37 UVMRP AOD_{368} (red) and AOD_{332} (blue) for September 3rd during TexAQS II/GoMACCS.

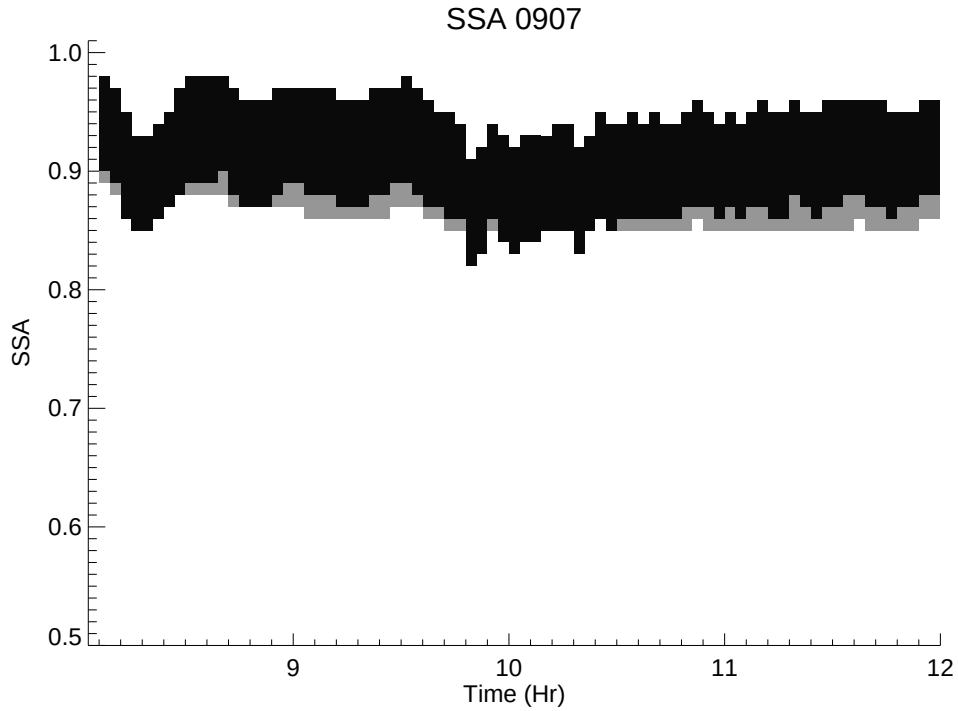

Figure 4.38 Ranges of SSA_{368} (black) and SSA_{332} (gray) for September 7th during TexAQS II/GoMACCS.

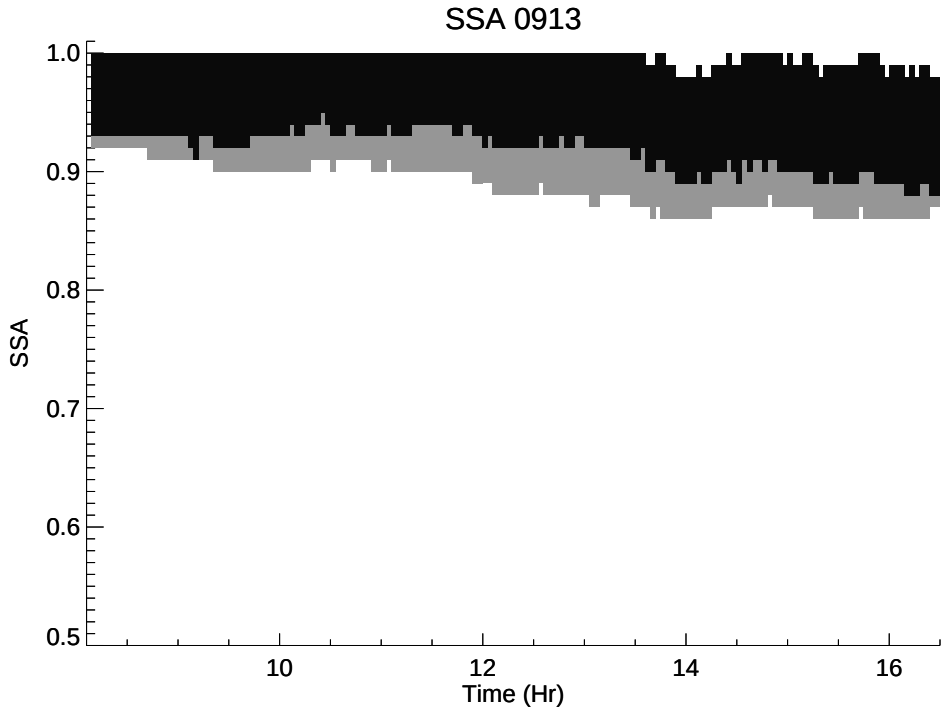

Figure 4.39 Ranges of SSA_{368} (black) and SSA_{332} (gray) for September 14th during TexAQS II/GoMACCS.

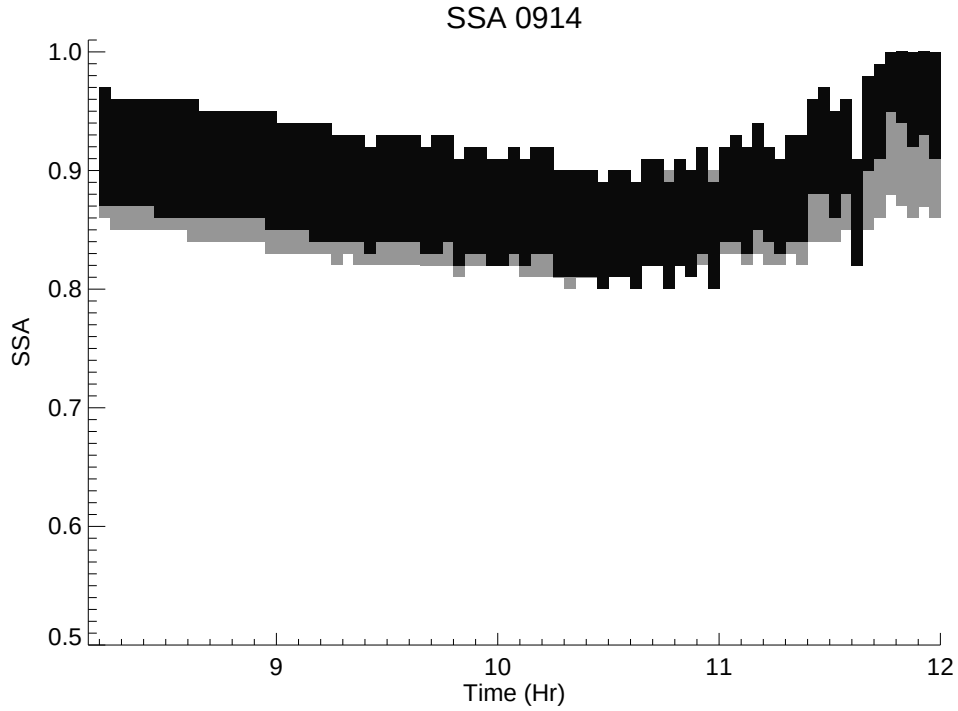

Figure 4.40 Ranges of SSA_{368} (black) and SSA_{332} (gray) for September 14th during TexAQS II/GoMACCS.

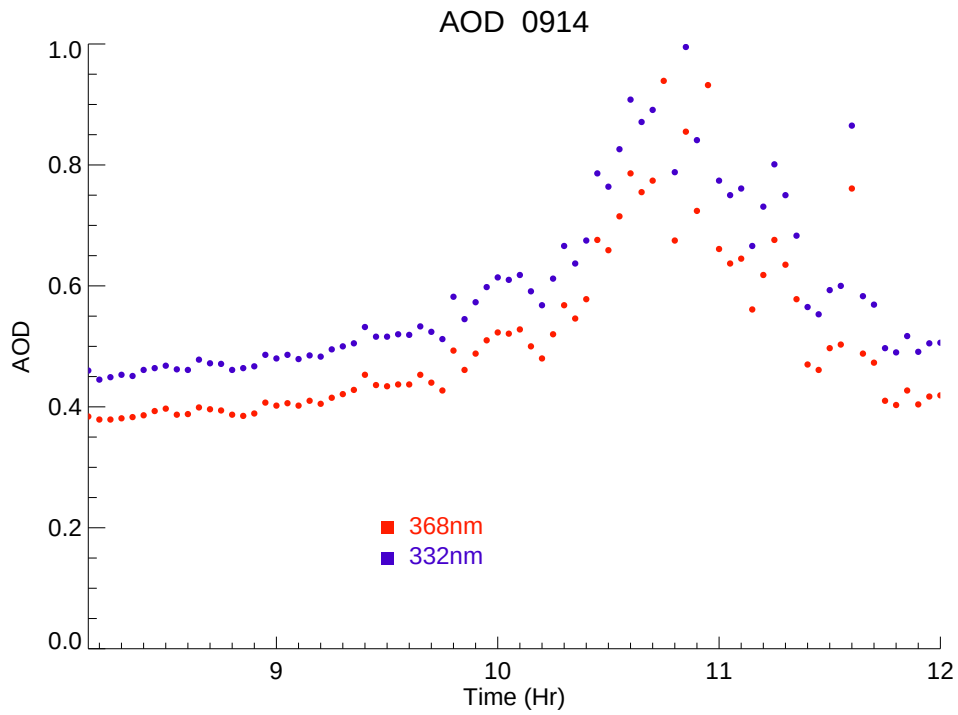

Figure 4.41UVMRP AOD_{368} (red) and AOD_{332} (blue) for September 14th during TexAQS II/GoMACCS.

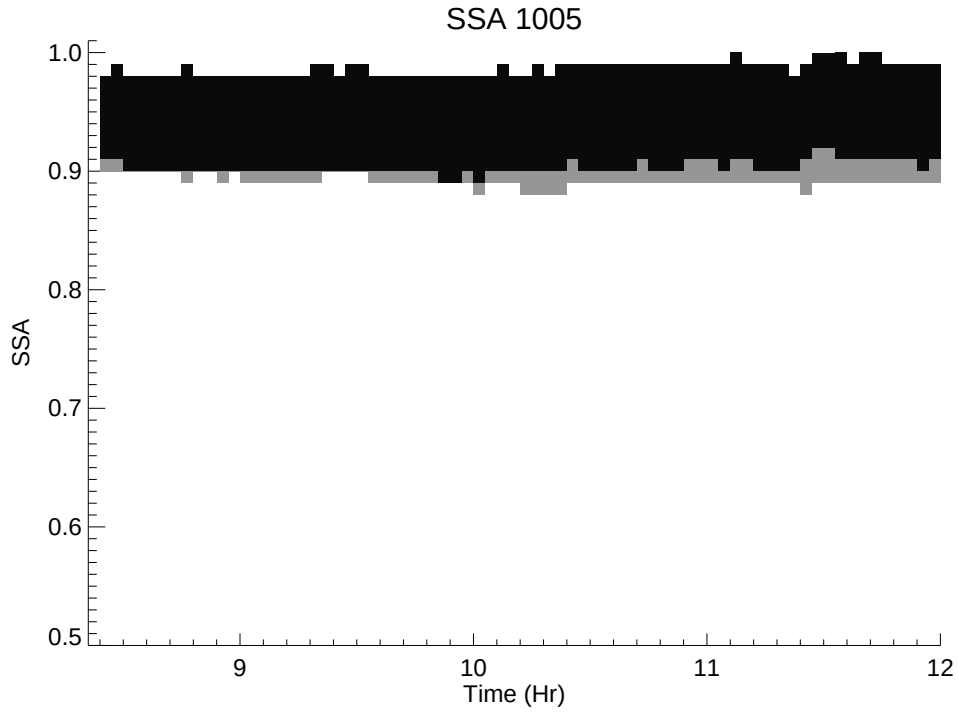

Figure 4.42 Ranges of SSA_{368} (black) and SSA_{332} (gray) for October 5th during TexAQS II/GoMACCS.

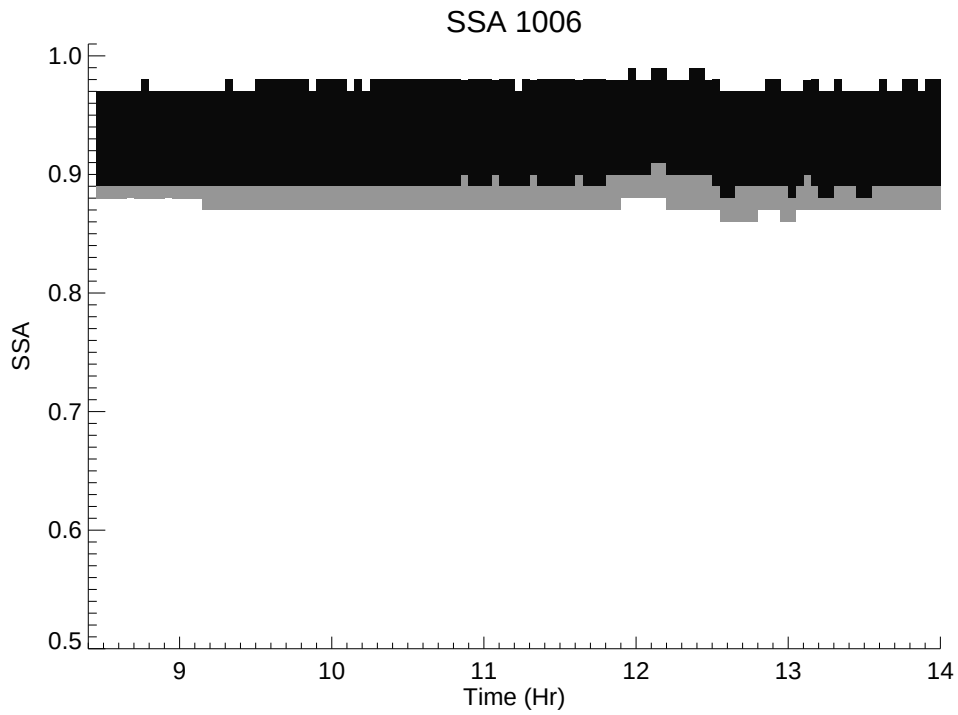

Figure 4.43 Ranges of SSA_{368} (black) and SSA_{332} (gray) for October 6th during TexAQS II/GoMACCS.

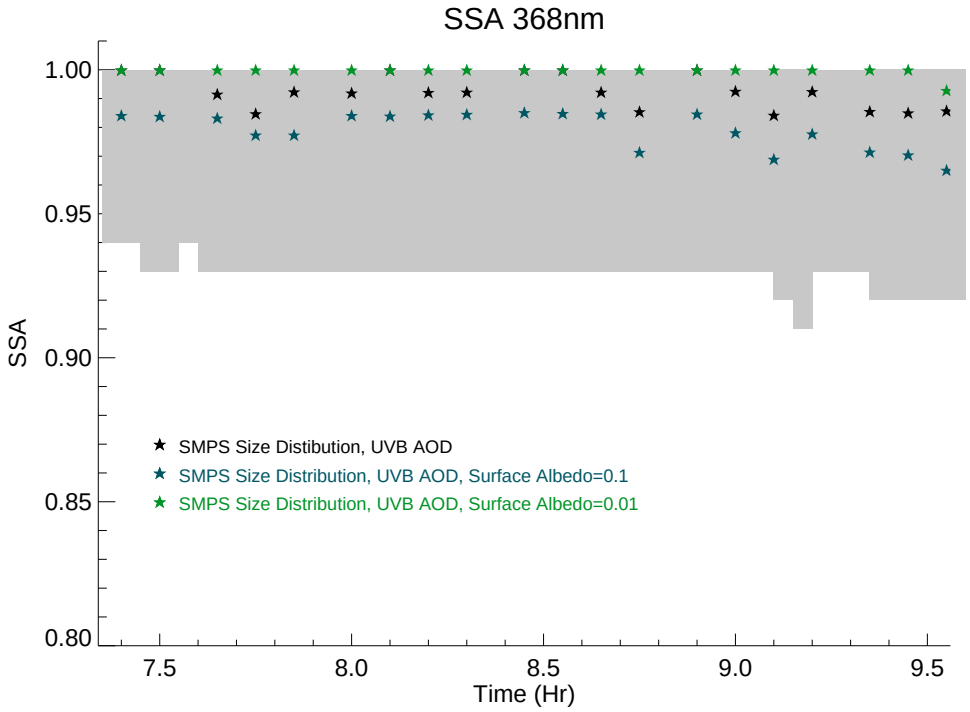

Figure 4.44 Best-fit (points) and ranges of SSA_{368} (gray shaded area). Best-fit SSA_{368} values were calculated using surface albedos of 0.01 (green), 0.05 (black), and 0.1 (blue).

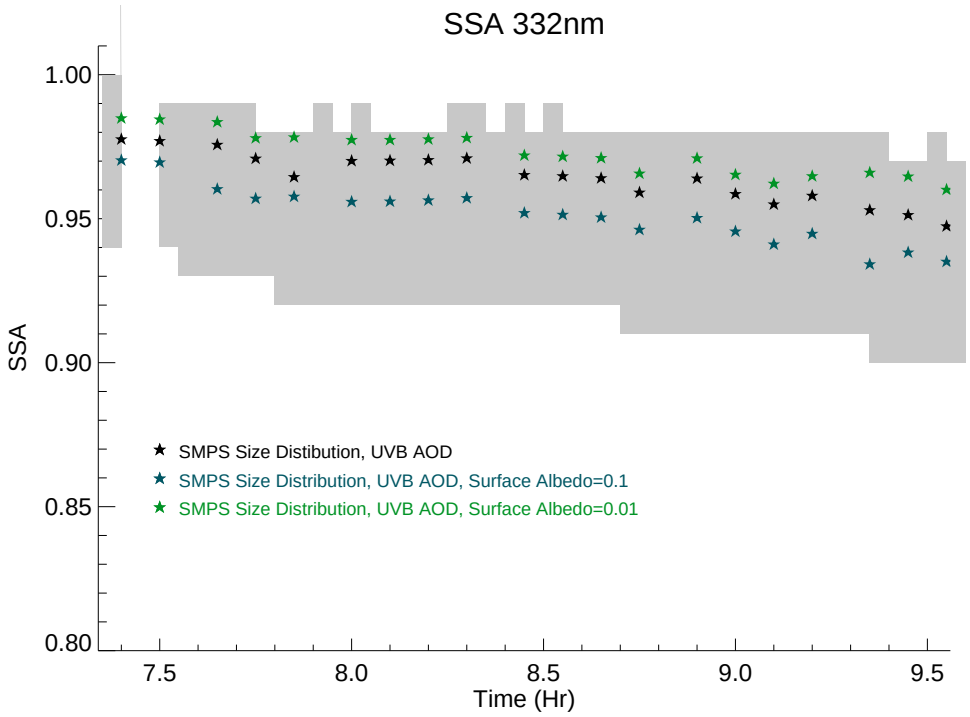

Figure 4.45 Best-fit (points) and ranges of SSA_{332} (gray shaded area). Best-fit SSA_{332} values were calculated using surface albedos of 0.01 (green), 0.05 (black), and 0.1 (blue).

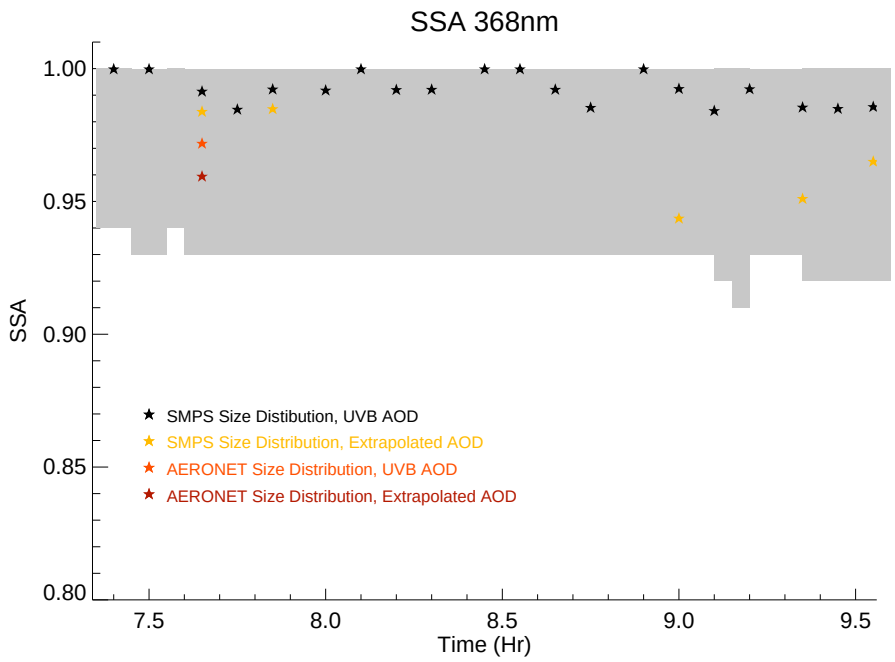

Figure 4.46 Best-fit (points) and ranges of SSA_{332} (gray shaded area). Best-fit SSA_{368} values were calculated using SMPS size distributions and UVMRP AOD_{368} (black), SMPS size distributions and extrapolated AOD_{368} (gold), AERONET size distributions and UVMRP AOD_{368} (orange) and AERONET size distributions and extrapolated AOD_{368} (red).

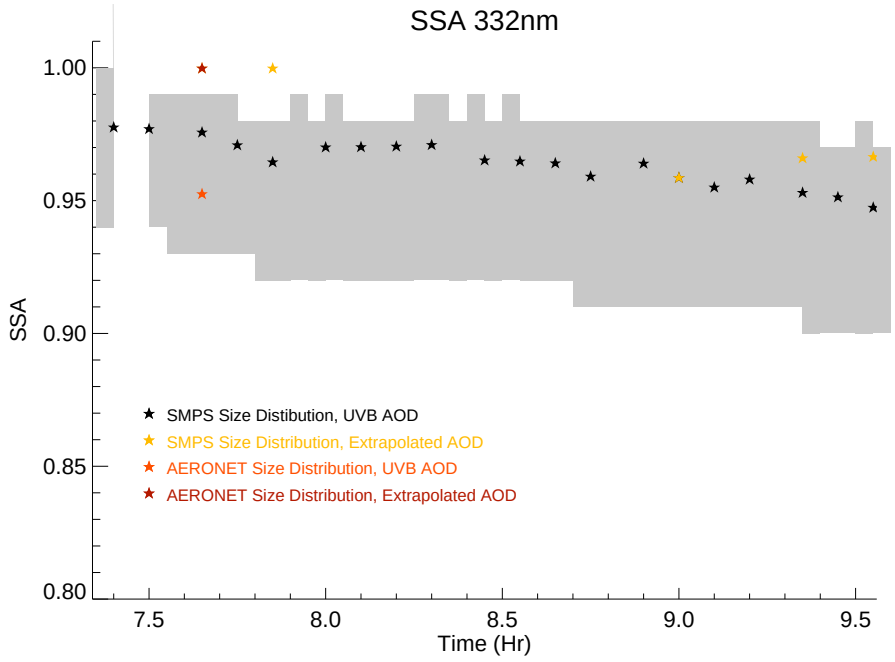

Figure 4.47 Best-fit (points) and ranges of SSA_{332} (gray shaded area). Best-fit SSA_{368} values were calculated using SMPS size distributions and UVMRP AOD_{368} (black), SMPS size distributions and extrapolated AOD_{368} (gold), AERONET size distributions and UVMRP AOD_{368} (orange) and AERONET size distributions and extrapolated AOD_{368} (red).

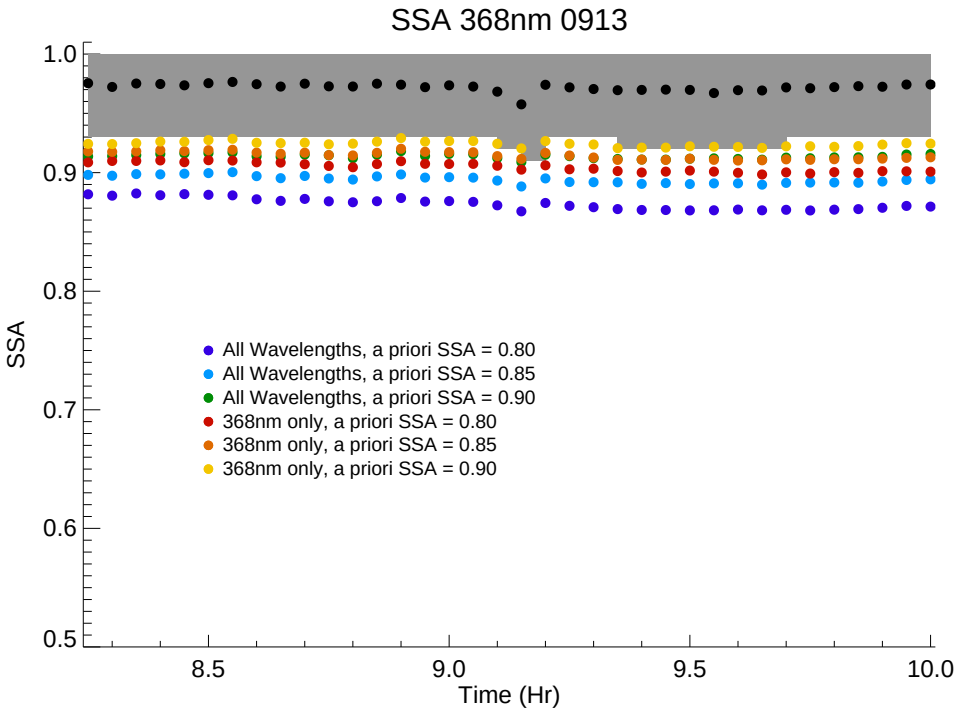

Figure 4.48 OE and partial single-wavelength SSA_{368} results. Black points represent average SSA_{368} and colored points represent OE algorithm results under several *a priori* SSA and wavelength scenarios.

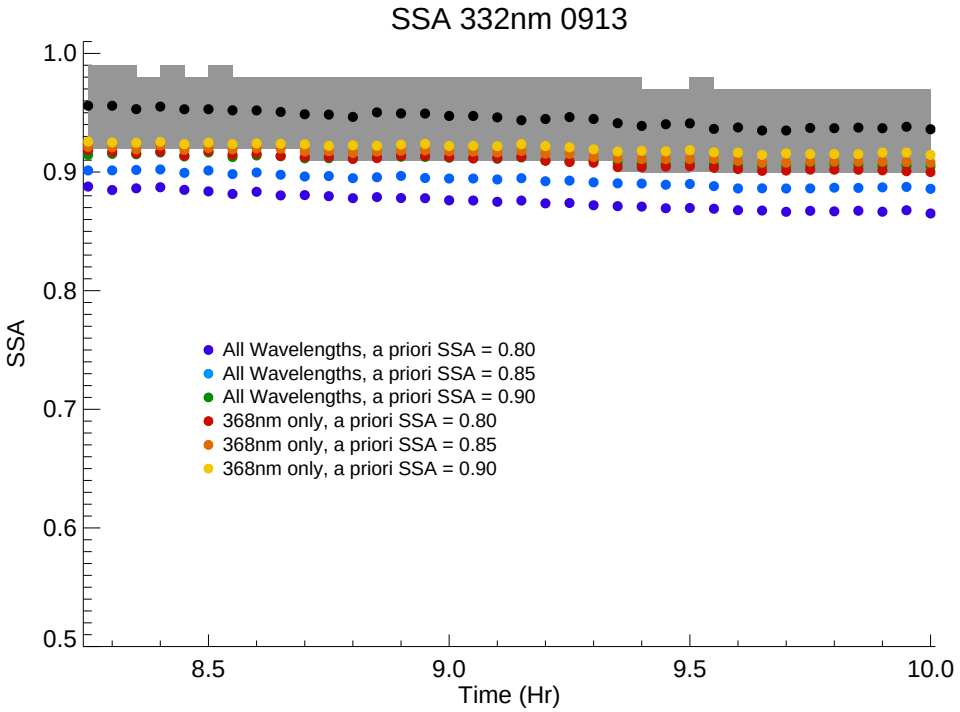

Figure 4.49 OE and partial single-wavelength SSA_{368} results. Black points represent average SSA_{368} and colored points represent OE algorithm results under several *a priori* SSA and wavelength scenarios.

5 Summary and Future Work

5.1 Summary of Retrieval Results

SSA time series were determined for two UV wavelengths using UV-MFRSR irradiance data obtained during the TexAQS II/GoMACCS and MILAGRO campaigns. Ranges of SSA values were obtained using the partial single-wavelength method developed in this work to conform to the measured DDR as described by Equation 3.17. TUV was used to retrieve ranges of SSA values that correspond to the range of g (0.6-0.9) yielding DDR values within 1% of the DDR value calculated using the UV-MFRSR data.

Range-average SSA_{368} and SSA_{332} determined for all eleven retrieval days (four from MILAGRO and seven from TexAQS II/GoMACCS) ranged from approximately 0.60 to 1.00 for 10 out of the 11 days. On March 19th during the MILAGRO campaign, ranges of instantaneous SSA_{368} and SSA_{332} of 0.518-0.728 and 0.500-0.702, respectively were obtained for the afternoon observations. The low values of SSA were attributed to the resuspension of local dust due to moderately high surface wind speeds based on auxiliary data from the site. The retrieved ranges of SSA values were consistent with UV SSA values reported in other studies [*Petters et al.*, 2003; *Wenny et al.*, 1998; *Wetzel et al.*, 2003].

All data were cloudscreened before retrievals were conducted. Average SSA values were fairly stable for each of the seven TexAQS II/GoMACCS retrieval days,

with little to no scatter in SSA_{368} and SSA_{332}. Two of the four MILAGRO retrieval days (March 19th and March 21st) were also stable; however, some high frequency variability in SSA_{368} and SSA_{332} was seen in the late morning-early afternoon hours of the other two MILAGRO retrieval days (March 12th and 13th). While March 12th and 13th passed the cloudscreening criteria, there was some notable high frequency variability in the 368nm direct irradiance profile for both days, potentially indicating a broken or cirrus cloud field for both days. It was suggested that cirrus and or broken cumulus clouds were responsible for the variation in SSA_{368} and SSA_{332} for both days. This emphasizes the need for an accurate cloudscreening mechanism to ensure the accuracy of retrieval results.

Range-averaged SSA_{368} and range-averaged SSA_{332} were determined and compared at each time interval for all retrieval days for both field campaigns. The Student's t-test was performed at each time interval for each day to determine the significance of the differences between range-averaged SSA_{368} and range-averaged SSA_{332}. Range-averaged SSA_{368} were significantly different than range-averaged SSA_{332} 60.9% and 65.0% of the retrieval time interevals on March 12th and March 13th, respectively. On March 19th and 21st, range-averaged SSA_{368} was higher than range-averaged SSA_{332} for nearly the entire retrieval period (93.3% and 100%, respectively). Range-averaged SSA_{368} and range-averaged SSA_{332} were significantly different for a substantial percentage of all seven TexAQS II/GoMACCS retrieval days. Range-averaged SSA_{368} was significantly different than range-averaged SSA_{332} for all retrieval time intervals for three of the TexAQS II/GoMACCS days: September 13th, October 5th, and October 6th.

For all retrieval days of both field campaigns, the significant differences between range-averaged SSA_{368} and range-averaged SSA_{332} were found where range-averaged SSA_{368} was larger than range-averaged SSA_{332}. These trends are explainable through an understanding particle size and composition effects on the wavelength dependence of SSA. Certain organic aerosol species as well as mineral dust would yield such a trend in SSA values as such aerosol types preferentially absorb at shorter wavelengths [e.g., *Derimian et al.*, 2007; *Jacobson*, 1999] by resulting in a stronger wavelength dependence in absorption than is predicted by theory [*Bond*, 2001; *Kirchstetter et al.*, 2004]. Additionally, larger particles, such as seasalt would result in a decrease in SSA with an increase in wavelength as explained by the relationship between SSA, wavelength, and particle size outlined in Bergstrom et al [2002].

To test the sensitivity of the retrievals to assumed input parameters, the full retrieval was run for the morning hours of September 13th using two different size distributions (AERONET and the SMPS), two different values of AOD (extrapolated and UVMRP), and three different values of surface albedo. These parameters were of interest as they represented the largest sources of potential error in the assumptions of input values used to run the partial retrieval code. It was shown that all best-fit SSA_{368} and best-fit SSA_{332} values were sensitive to size distribution, AOD, and surface albedo. However, despite the variation in the magnitude of the best-fit SSA_{368} and best-fit SSA_{332}, best-fit SSA values for all of the assumptions generally fell within the retrieved ranges of SSA values, indicating the 1% relative error assumption, along with the specified range in g, was sufficient at capturing potential

error in input values. One value of best-fit SSA_{332} calculated using the AERONET size distribution and extrapolated AOD fell outside of the range of good SSA_{332} values suggesting some additional error in the 332nm irradiance data (e.g., inaccurate $V_{o,\lambda}$ value).

Partial single-wavelength retrieval results were also compared to SSA_{368} and SSA_{332} determined using the OE algorithm described in Taylor et al [2008]. The OE algorithm was run for the morning hours of September 13th using three different values for *a priori* SSA and two wavelength scenarios: one where all seven UV-MFRSR wavelengths were considered in the solution matrix and the other where all wavelengths except the wavelength of interest (either 368nm or 332nm) were effectively removed from the solution matrix. OE retrieved SSA values increased with increases in the *a priori* SSA values (~0.04 for both wavelengths) and when only one wavelength was considered in the solution matrix (~0.02 for both wavelengths). However, regardless of the *a priori* SSA value and the wavelength scenario, the OE algorithm SSA values were generally lower than the retrieved SSA ranges of the partial single-wavelength method. This was attributed to error associated with the shorter wavelength channels used in the minimization technique of the OE method as well as error associated with the $V_{o,\lambda}$ values considered by the OE algorithm through the use of direct and diffuse irradiance independently to determine aerosol UV optical properties.

5.2 Suggestions for Future Work

The findings presented in this work add to a growing database of aerosol UV optical properties. However, knowledge of aerosol-UV radiation interactions still remains fairly limited. As such, some suggestions for future work include:

- **Compare retrieved SSA with aerosol chemistry and back trajectory data sets.**

In this work, some preliminary comparisons between reported aerosol chemistry data were done for the MILAGRO retrieval days. However, comparisons were qualitative and only involved the visual comparison of OC and EC trends with trends in instantaneous SSA values. To better understand the potential relationships between aerosol composition and UV SSA, statistical analysis should be used to examine correlations between trends in high resolution aerosol chemical data and retrieved SSA values. Quantitative analysis of the relationship between aerosol composition and UV SSA should be performed for both field campaigns as chemical data are made available.

Several studies have examined the relationship between air mass type and retrieved UV SSA [*Petters et al.*, 2003; *Wenny et al.*, 1998; *Wetzel et al.*, 2003]. A similar analysis should also be performed for the retrieval days of the MILAGRO and TexAQS II/GoMACCS campaigns. Using back trajectory software, such as NOAA's HYSPLIT model, would provide additional information regarding the sources of air mass to the measurement sites. Such information would be a useful addition to surface chemical data as free-tropospheric aerosol, such as dust, may not be

measurable at the surface but would still significantly affect the surface radiation field.

- **Compare measured photolysis rates to those modeled using retrieved SSA values as input.**

As previously discussed, aerosol interactions with UV radiation can have profound effects on the surface UV radiation field. These effects have been shown to both enhance and suppress tropospheric photochemistry, thus affecting the formation of ground-level O_3 [*Dickerson et al.*, 1997; *Liao et al.*, 1999]. Therefore, in order to properly forecast ground-level O_3 episodes, accurate values of aerosol UV optical properties are needed.

In addition to irradiance, the TUV model used in this work may be used to calculate actinic flux and photolysis rate coefficients using the same set of user defined inputs. Using the range-averaged SSA_{368} and SSA_{332} values for the SSA inputs, photolysis rate coefficients can be calculated and compared to measured photolysis rate coefficients taken during both the MILAGRO and TexAQS II/GoMACCS field campaigns. This comparison would either verify or disprove that aerosols do in fact affect photolysis rates. Similarly, photolysis rate coefficients calculated using retrieved range-averaged SSA_{368} and SSA_{332} values may be compared to photolysis rate coefficients calculated under aerosol-free conditions. Because retrieved SSA values are determined from irradiance data, they represent UV SSA values of real, atmospheric aerosol. Studies that have previously examined effects of aerosols on photolysis have largely examined how pure aerosol types (e.g., sulfate, black carbon) affect photolysis rates, situations that may not be entirely

atmospherically relevant. Comparison between photolysis rates determined using retrieved instantaneous SSA values and photolysis rates determined under aerosol-free conditions may therefore provide a more realistic picture of how the presence of urban aerosol may affect photolysis rates and thus ground-level O_3 formation.

- **Compare retrieved UV SSA values with visible SSA values.**

Several claims for a spectral dependence of SSA were made based on statistical analysis in this work. However, due to data availability constraints, these SSA values were not compared to SSA values calculated or measured in the visible range during the two field campaigns, thus it cannot be concluded that the observed spectral dependencies extend beyond the near-UV range. Examining trends in SSA values from the UV into the visible range would provide further support for or against the spectral dependence of SSA.

- **Continued comparison of aerosol UV optical properties retrieval methods.**

As indicated by this work's results, there are some discrepancies between SSA values retrieved using different retrieval methods. The partial single-wavelength method developed here was compared to a full single-wavelength method similar in design to that used in Krotkov et al [2005b] and an optimal estimation method [*Taylor et al.*, 2008]. Both methods, along with other methods similar to the partial single-wavelength method designed here [*Petters et al.*, 2003], have been used to retrieve aerosol UV optical properties and thus it is important to examine the reasons for potential differences in retrieval results. While some of these reasons were mentioned in this work, potential differences should be quantified and improvement to the retrieval methods made to ensure accurate retrieval of UV optical properties.

REFERENCES

Acosta, L. R., and W. F. J. Evans (2000), Design of the Mexico City UV monitoring network: UV-B measurements at ground level in the urban environment, *Journal of Geophysical Research-Atmospheres*, *105*(D4), 5017-5026.

Adam, M. E., and S. M. El Shazly (2007), Attenuation of UV-B radiation in the atmosphere: Clouds effect, at Qena (Egypt), *Atmospheric Environment*, *41*, 4856-4864.

Bergstrom, R. W., P. B. Russell, and P. Hignett (2002), Wavelength dependence of the absorption of black carbon particles: Predictions and results from the TARFOX experiment and implications for the aerosol single scattering albedo, *Journal of the Atmospheric Sciences*, *59*(3), 567-577.

Bergstrom, R. W., P. Pilewskie, B. Schmid, and P. B. Russell (2003), Estimates of the spectral aerosol single scattering albedo and aerosol radiative effects during SAFARI 2000, *Journal of Geophysical Research-Atmospheres*, *108*(D13), doi:10.1029/2002JD002435.

Bergstrom, R. W., P. Pilewskie, J. Pommier, M. Rabbette, P. B. Russell, B. Schmid, J. Redemann, A. Higurashi, T. Nakajima, and P. K. Quinn (2004), Spectral absorption of solar radiation by aerosols during ACE-Asia, *Journal of Geophysical Research-Atmospheres*, *109*(D19), doi:10.1029/2003JD004467.

Bergstrom, R. W., P. Pilewskie, P. B. Russell, J. Redemann, T. C. Bond, P. K. Quinn, and B. Sierau (2007), Spectral absorption properties of atmospheric aerosols, *Atmospheric Chemistry and Physics*, *7*, 5937-5943.

Bigelow, D. S., J. R. Slusser, A. F. Beaubien, and J. H. Gibson (1998), The USDA ultraviolet radiation monitoring program, *Bulletin of the American Meteorological Society*, *79*(4), 601-615.

Blumthaler, M., and W. Ambach (1990), Indication of increasing solar ultraviolet-B radiation flux in alpine regions, *Science*, *248*(4952), 206-208.

Bond, T. C. (2001), Spectral dependence of visible light absorption by carbonaceous particles emitted from coal combustion, *Geophysical Research Letters*, *28*(21), 4075-4078.

Bornman, J. F., and A. H. Teramura (1993), *Environmental UV Photobiology*, Plenum Press, New York, New York.

Castro, T., B. Mar, R. Longoria, L. G. Ruiz-Suarez, and L. Morales (2001), Surface albedo measurements in Mexico City metropolitan area, *Atmosfera*, *14*(2), 69-74.

Derimian, Y., Y. J. K. A. Karnieli, M. O. Andreae, T. W. Andreae, O. Dubovik, W. Maenhaut, and I. Koren (2007), The role of iron and black carbon in aerosol light absorption, *Atmospheric Chemistry and Physics Discussions*, *7*, 8159-8192.

Diaz, J. P., F. J. Exposito, C. J. Torres, V. Carreno, and A. Redondas (2000), Simulation of mineral dust effects on UV radiation levels, *Journal of Geophysical Research-Atmospheres*, *105*(D4), 4979-4991.

Dickerson, R. R., S. Kondragunta, G. Stenchikov, K. L. Civerolo, B. G. Doddridge, and B. N. Holben (1997), The impact of aerosols on solar ultraviolet radiation and photochemical smog, *Science*, *278*(5339), 827-830.

Diffey, B. L. (1991), Solar ultraviolet-radiation effects on biological-systems, *Physics in Medicine and Biology*, *36*(3), 299-328.

Doran, J. C., J. C. Barnard, W. P. Arnott, R. Cary, R. Coulter, J. D. Fast, E. I. Kassianov, L. Kleinman, N. S. Laulainen, T. Martin, G. Paredes-Miranda, M. S. Pekour, W. J. Shaw, D. F. Smith, S. R. Springston, and X. Y. Yu (2007), The T1-T2 study: evolution of aerosol properties downwind of Mexico City, *Atmospheric Chemistry and Physics*, *7*(6), 1585-1598.

Dubovik, O., and M. D. King (2000), A flexible inversion algorithm for retrieval of aerosol optical properties from Sun and sky radiance measurements, *Journal of Geophysical Research-Atmospheres*, *105*(D16), 20673-20696.

Dubovik, O., A. Smirnov, B. N. Holben, M. D. King, Y. J. Kaufman, T. F. Eck, and I. Slutsker (2000), Accuracy assessments of aerosol optical properties retrieved from Aerosol Robotic Network (AERONET) Sun and sky radiance measurements, *Journal of Geophysical Research-Atmospheres*, *105*(D8), 9791-9806.

Dubovik, O., A. Sinyuk, T. Lapyonok, B. N. Holben, M. Mishchenko, P. Yang, T. F. Eck, H. Volten, O. Munoz, B. Veihelmann, W. J. van der Zande, J. F. Leon, M. Sorokin, and I. Slutsker (2006), Application of spheroid models to account for aerosol particle nonsphericity in remote sensing of desert dust, *Journal of Geophysical Research-Atmospheres*, *111*(D11), doi:10.1029/2005JD006619.

Eck, T. F., B. N. Holben, I. Slutsker, and A. Setzer (1998), Measurements of irradiance attenuation and estimation of aerosol single scattering albedo for

biomass burning aerosols in Amazonia, *Journal of Geophysical Research-Atmospheres*, *103*(D24), 31865-31878.

Elminir, H. K. (2007), Sensitivity of ultraviolet solar radiation to anthropogenic air pollutants and weather conditions, *Atmospheric Research*, *84*(3), 250-264.

Elterman.L, R. Wexler, and D. T. Chang (1969), Features of tropospheric and stratospheric dust, *Applied Optics*, *8*(5), 893-&.

Fast, J. D., B. de Foy, F. A. Rosas, E. Caetano, G. Carmichael, L. Emmons, D. McKenna, M. Mena, W. Skamarock, X. Tie, R. L. Coulter, J. C. Barnard, C. Wiedinmyer, and S. Madronich (2007), A meteorological overview of the MILAGRO field campaigns, *Atmospheric Chemistry and Physics*, *7*(9), 2233-2257.

Finlayson-Pitts, B. J., and J. N. Pitts (2000), *Chemistry of the Upper and Lower Atmosphere*, Academic Press, San Deigo, California.

Forster, P., V. Ramaswamy, P. Artaxo, T. Bernsten, R. Betts, D. W. Fahey, J. Haywood, J. Lean, D. C. Lowe, G. Myhre, J. Nganga, R. Prinn, G. Raga, M. Schulz, and R. Van Dorland (2007), Changes in Atmospheric Constituents and in Radiative Forcing, Cambridge, UK.

Gao, W., J. Slusser, J. Gibson, G. Scott, D. Bigelow, J. Kerr, and B. McArthur (2001), Direct-Sun column ozone retrieval by the ultraviolet multifilter rotating shadow-band radiometer and comparison with those from Brewer and Dobson spectrophotometers, *Applied Optics*, *40*(19), 3149-3155.

Ghan, S. J., R. C. Easter, E. G. Chapman, H. Abdul-Razzak, Y. Zhang, L. R. Leung, N. S. Laulainen, R. D. Saylor, and R. A. Zaveri (2001), A physically based estimate of radiative forcing by anthropogenic sulfate aerosol, *Journal of Geophysical Research-Atmospheres*, *106*(D6), 5279-5293.

Goering, C. D., T. S. L'Ecuyer, G. L. Stephens, J. R. Slusser, G. Scott, J. Davis, J. C. Barnard, and S. Madronich (2005), Simultaneous retrievals of column ozone and aerosol optical properties from direct and diffuse solar irradiance measurements, *Journal of Geophysical Research-Atmospheres*, *110*(D5), doi:10.1029/2004JD005330.

Harrison, L., J. Michalsky, and J. Berndt (1994), Automated multifilter rotating shadow-band radiometer - an instrument for optical depth and radiation measurements, *Applied Optics*, *33*(22), 5118-5125.

Haywood, J. M., S. R. Osborne, P. N. Francis, A. Keil, P. Formenti, M. O. Andreae, and P. H. Kaye (2003), The mean physical and optical properties of regional haze dominated by biomass burning aerosol measured from the C-130 aircraft

during SAFARI 2000, *Journal of Geophysical Research-Atmospheres*, *108*(D13), doi:10.1029/2002JD002226.

He, S., and G. R. Carmichael (1999), Sensitivity of photolysis rates and ozone production in the troposphere to aerosol properties, *Journal of Geophysical Research-Atmospheres*, *104*(D21), 26307-26324.

Herman, J. R., N. Krotkov, E. Celarier, D. Larko, and G. Labow (1999), Distribution of UV radiation at the Earth's surface from TOMS-measured UV-backscattered radiances, *Journal of Geophysical Research-Atmospheres*, *104*(D10), 12059-12076.

Holben, B. N., T. F. Eck, I. Slutsker, D. Tanre, J. P. Buis, A. Setzer, E. Vermote, J. A. Reagan, Y. J. Kaufman, T. Nakajima, F. Lavenu, I. Jankowiak, and A. Smirnov (1998), AERONET - A federated instrument network and data archive for aerosol characterization, *Remote Sensing of Environment*, *66*(1), 1-16.

Holben, B. N., D. Tanre, A. Smirnov, T. F. Eck, I. Slutsker, N. Abuhassan, W. W. Newcomb, J. S. Schafer, B. Chatenet, F. Lavenu, Y. J. Kaufman, J. V. Castle, A. Setzer, B. Markham, D. Clark, R. Frouin, R. Halthore, A. Karneli, N. T. O'Neill, C. Pietras, R. T. Pinker, K. Voss, and G. Zibordi (2001), An emerging ground-based aerosol climatology: Aerosol optical depth from AERONET, *Journal of Geophysical Research-Atmospheres*, *106*(D11), 12067-12097.

Jacobson, M. Z. (1999), Isolating nitrated and aromatic aerosols and nitrated aromatic gases as sources of ultraviolet light absorption, *Journal of Geophysical Research-Atmospheres*, *104*(D3), 3527-3542.

Jacovides, C. P., N. A. Kaltsounides, D. N. Asimakopoulos, and D. G. Kaskaoutis (2005), Spectral aerosol optical depth and Angstrom parameters in the polluted Athens atmosphere, *Theoretical and Applied Climatology*, *81*(3-4), 161-167.

Junkermann, W., C. Bruhl, D. Perner, E. Eckstein, T. Trautmann, B. Fruh, R. Dlugi, T. Gori, A. Ruggaber, J. Reuder, M. Zelger, A. Hofzumahaus, A. Kraus, F. Rohrer, D. Bruning, G. Moortgat, A. Horowitz, and J. Tadic (2002), Actinic radiation and photolysis processes in the lower troposphere: Effect of clouds and aerosols, *Journal of Atmospheric Chemistry*, *42*(1), 413-441.

Junkermann, W. (2005), The actinic UV-radiation budget during the ESCOMPTE campaign 2001: results of airborne measurements with the microlight research aircraft D-MIFU, *Atmospheric Research*, *74*(1-4), 461-475.

Kaufman, Y. J. (1993), Aerosol optical-thickness and atmospheric path radiance, *Journal of Geophysical Research-Atmospheres*, *98*(D2), 2677-2692.

Kerr, S. C., J. J. Schauer, and B. Rodger (2004), Regional haze in Wisconsin: sources and the spatial distribution, *Journal of Environmental Engineering and Science*, *3*(3), 213-222.

King, M. D., and D. M. Byrne (1976), Method for inferring total ozone content from spectral variation of total optical depth obtained with a solar radiometer, *Journal of the Atmospheric Sciences*, *33*(11), 2242-2251.

Kirchstetter, T. W., T. Novakov, and P. V. Hobbs (2004), Evidence that the spectral dependence of light absorption by aerosols is affected by organic carbon, *Journal of Geophysical Research-Atmospheres*, *109*(D21), doi:10.1029/2004JD004999.

Krotkov, N., P. K. Bhartia, J. Herman, J. Slusser, G. Labow, G. Scott, G. Janson, T. F. Eck, and B. Holben (2005a), Aerosol ultraviolet absorption experiment (2002 to 2004), part 1: ultraviolet multifilter rotating shadowband radiometer calibration and intercomparison with CIMEL sunphotometers, *Optical Engineering*, *44*(4), doi:10.1117/1.1886818.

Krotkov, N., P. K. Bhartia, J. Herman, J. Slusser, G. Scott, G. Labow, A. P. Vasilkov, T. F. Eck, O. Dubovik, and B. N. Holben (2005b), Aerosol ultraviolet absorption experiment (2002 to 2004), part 2: absorption optical thickness, refractive index, and single scattering albedo, *Optical Engineering*, *44*(4), doi:10.1117/1.1886819.

L'Ecuyer, T. S., and G. L. Stephens (2002), An estimation-based precipitation retrieval algorithm for attenuating radars, *Journal of Applied Meteorology*, *41*(3), 272-285.

Lefer, B. L., R. E. Shetter, S. R. Hall, J. H. Crawford, and J. R. Olson (2003), Impact of clouds and aerosols on photolysis frequencies and photochemistry during TRACE-P: 1. Analysis using radiative transfer and photochemical box models, *Journal of Geophysical Research-Atmospheres*, *108*(D21), doi:10.1029/2002JD003171.

Liao, H., Y. L. Yung, and J. H. Seinfeld (1999), Effects of aerosols on tropospheric photolysis rates in clear and cloudy atmospheres, *Journal of Geophysical Research-Atmospheres*, *104*(D19), 23697-23707.

Longstreth, J., F. R. de Gruijl, M. L. Kripke, S. Abseck, F. Arnold, H. I. Slaper, G. Velders, Y. Takizawa, and J. C. van der Leun (1998), Health risks, *Journal of Photochemistry and Photobiology B-Biology*, *46*(1-3), 20-39.

Madronich, S. (1993), *Environmental UV Photobiology*, Plenum Press, New York, New York.

McKenzie, R., B. Conner, and G. Bodeker (1999), Increased summertime UV radiation in New Zealand in response to ozone loss, *Science*, *285*(5434), 1709-1711.

McKenzie, R. L., M. Kotkamp, and W. Ireland (1996), Upwelling UV spectral irradiances and surface albedo measurements at Lauder, New Zealand, *Geophysical Research Letters*, *23*(14), 1757-1760.

McMeeking, G. R., S. M. Kreidenweis, M. Lunden, J. Carrillo, C. M. Carrico, T. Lee, P. Herckes, G. Engling, D. E. Day, J. Hand, N. Brown, W. C. Malm, and J. L. Collett (2006), Smoke-impacted regional haze in California during the summer of 2002, *Agricultural and Forest Meteorology*, *137*(1-2), 25-42, doi:10.1016/j.agrformet.2006.01.011.

Papayannis, A., D. Balis, A. Bais, H. Van Der Bergh, B. Calpini, E. Durieux, L. Fiorani, L. Jaquet, I. Ziomas, and C. S. Zerefos (1998), Role of urban and suburban aerosols on solar UV radiation over Athens, Greece, *Atmospheric Environment*, *32*(12), 2193-2201.

Petters, J. L., V. K. Saxena, J. R. Slusser, B. N. Wenny, and S. Madronich (2003), Aerosol single scattering albedo retrieved from measurements of surface UV irradiance and a radiative transfer model, *Journal of Geophysical Research-Atmospheres*, *108*(D9), doi:10.1029/2002JD002360.

Querol, X., J. Pey, M. C. Minguillon, N. Perez, A. Alastuey, M. Viana, T. Moreno, R. M. Bernabe, S. Blanco, B. Cardenas, E. Vega, G. Sosa, S. Escalona, H. Ruiz, and B. Artinano (2008), PM speciation and sources in Mexico during the MILAGRO-2006 Campaign, *Atmospheric Chemistry and Physics*, *8*(1), 111-128.

Reid, J. S., T. F. Eck, S. A. Christopher, P. V. Hobbs, and B. Holben (1999), Use of the Angstrom exponent to estimate the variability of optical and physical properties of aging smoke particles in Brazil, *Journal of Geophysical Research-Atmospheres*, *104*(D22), 27473-27489.

Reuder, J., and H. Schwander (1999), Aerosol effects on UV radiation in nonurban regions, *Journal of Geophysical Research-Atmospheres*, *104*(D4), 4065-4077.

Rodgers, C. D. (2000), *Inverse Methods For Atmospheric Sounding: Theory and Practice*, World Scientific Publishing Company Pte. Ltd.

Rosenfeld, D. (2000), Suppression of rain and snow by urban and industrial air pollution, *Science*, *287*(5459), 1793-1796.

Schmid, B., J. Michalsky, R. Halthore, M. Beauharnois, L. Harrison, J. Livingston, P. Russell, B. Holben, T. Eck, and A. Smirnov (1999), Comparison of aerosol

optical depth from four solar radiometers during the Fall 1997 ARM Intensive Observation Period, *Geophysical Research Letters*, *26*(17), 2725-2728.

Schuster, G. L., O. Dubovik, and B. N. Holben (2006), Angstrom exponent and bimodal aerosol size distributions, *Journal of Geophysical Research-Atmospheres*, *111*(D7), doi:10.1029/2005JD006328.

Scourfield, M. W. J., and G. E. Bodeker (2000), The influence of cloud and surface albedo on surface UV erythemal irradiance, *Physics and Chemistry of the Earth Part B-Hydrology Oceans and Atmosphere*, *25*(5-6), 521-523.

Seinfeld, J. H., and S. N. Pandis (2006), *Atmospheric Chemistry and Physics*, John Wiley & Sons, Inc., Hoboken, New Jersey.

Sinyuk, A., O. Dubovik, B. Holben, T. F. Eck, F. M. Breon, J. Martonchik, R. Kahn, D. J. Diner, E. F. Vermote, J. C. Roger, T. Lapyonok, and I. Slutsker (2007), Simultaneous retrieval of aerosol and surface properties from a combination of AERONET and satellite data, *Remote Sensing of Environment*, *107*(1-2), 90-108.

Slusser, J., J. Gibson, D. Bigelow, D. Kolinski, W. Mou, G. Koenig, and A. Beaubien (1999), Comparison of column ozone retrievals by use of an UV multifilter rotating shadow-band radiometer with those from Brewer and Dobson spectrophotometers, *Applied Optics*, *38*(9), 1543-1551.

Slusser, J., J. Gibson, D. Bigelow, D. Kolinski, P. Disterhoft, K. Lantz, and A. Beaubien (2000), Langley method of calibrating UV filter radiometers, *Journal of Geophysical Research-Atmospheres*, *105*(D4), 4841-4849.

Smirnov, A., B. N. Holben, T. F. Eck, O. Dubovik, and I. Slutsker (2000), Cloud-screening and quality control algorithms for the AERONET database, *Remote Sensing of Environment*, *73*(3), 337-349.

Sokolik, I. N., and O. B. Toon (1999), Incorporation of mineralogical composition into models of the radiative properties of mineral aerosol from UV to IR wavelengths, *Journal of Geophysical Research-Atmospheres*, *104*(D8), 9423-9444.

Taylor, T. E. (2006), Ozone and Aerosol Optical Properties from Ground Based Ultra-violet Irradiance Measurements, Colorado State University, Fort Collins, Colorado.

Taylor, T. E., T. S. L'Ecuyer, J. R. Slusser, G. L. Stephens, and C. D. Goering (2008), An operational retrieval algorithm for determining aerosol optical properties in the ultraviolet, *Journal of Geophysical Research-Atmospheres*, *113*, doi:10.1029/2007JD008661.

Toon, O. B., C. P. McKay, T. P. Ackerman, and K. Santhanam (1989), Rapid calculation of radiative heating rates and photodissociation rates in inhomogeneous multiple-scattering atmospheres, *Journal of Geophysical Research-Atmospheres*, *94*(D13), 16287-16301.

Twomey, S. (1977), Influence of pollution on shortwave albedo of clouds, *Journal of the Atmospheric Sciences*, *34*(7), 1149-1152.

Weaver, C. J., P. Ginoux, N. C. Hsu, M. D. Chou, and J. Joiner (2002), Radiative forcing of Saharan dust: GOCART model simulations compared with ERBE data, *Journal of the Atmospheric Sciences*, *59*(3), 736-747.

Webb, A. R., I. M. Stromberg, H. Li, and L. M. Bartlett (2000), Airborne spectral measurements of surface reflectivity at ultraviolet and visible wavelengths, *Journal of Geophysical Research-Atmospheres*, *105*(D4), 4945-4948.

Wendisch, M., P. Pilewskie, J. Pommier, S. Howard, P. Yang, A. J. Heymsfield, C. G. Schmitt, D. Baumgardner, and B. Mayer (2005), Impact of cirrus crystal shape on solar spectral irradiance: A case study for subtropical cirrus, *Journal of Geophysical Research-Atmospheres*, *110*(D3), doi:10.1029/2004JD005294.

Wenny, B. N., J. S. Schafer, J. J. DeLuisi, V. K. Saxena, W. F. Barnard, I. V. Petropavlovskikh, and A. J. Vergamini (1998), A study of regional aerosol radiative properties and effects on ultraviolet-B radiation, *Journal of Geophysical Research-Atmospheres*, *103*(D14), 17083-17097.

Wetzel, M. A., G. E. Shaw, J. R. Slusser, R. D. Borys, and C. F. Cahill (2003), Physical, chemical, and ultraviolet radiative characteristics of aerosol in central Alaska, *Journal of Geophysical Research-Atmospheres*, *108*(D14), doi:10.1029/2002JD003208.

Zwick, H., W. Popp, C. Wagner, K. Reiser, J. Schmoger, A. Bock, K. Herkner, and K. Radunsky (1991), Effects of ozone on the respiratory health, allergic sensitization, and cellular immune-system in children, *American Review of Respiratory Disease*, *144*(5), 1075-1079.